Temperature and pressure induced changes in the local atomic and electronic structure of complex materials

Dissertation

zur Erlangung des Doktorgrades der Naturwissenschaften

der Fakultät Physik der Technischen Universität Dortmund

vorgelegt von

Christoph J. Sahle

November 2011

Contents

List of Figures

List of Acronyms

a-GeO	Amorphous germanium monoxide
APS	Advanced Photon Source
DAC	Diamond anvil cell
DDSCS	Double differential scattering cross-section
DELTA	Dortmunder Elektronen Speicherring Anlage
DFT	Density functional theory
DOS	Density of states
EDX	Energy dispersive x-ray spectroscopy
ESRF	European Synchrotron Radiation Facility
EXAFS	Extended x-ray absorption fine structure
FDM	Finite difference method
FMS	Full multiple scattering
FWHM	Full width at half maximum
GGA	Generalized gradient approximation
GR	Giant resonance
HDAC	Hydrothermal diamond anvil cell
H-bond	Hydrogen-bond
ICM	Interface clusters mixture (model)
IXS	Inelastic x-ray scattering
LDA	Local density approximation
LERIX	Lower energy resolution inelastic x-ray scattering spectrometer
MEM	Maximum Entropy Method
ML	Multilayer
NC	Nanocrystal
NRIXS	Non-resonant inelastic x-ray scattering
PFY	Partial fluorescence yield
PIPS	Passivated Implanted Planar Silicon
RBS	Rutherford backscattering
RDF	Radial distribution function
RIXS	Resonant inelastic x-ray scattering
RMC	Reverse Monte Carlo (method)
ROI	Region of interest
RSMS	Real space multiple scattering
SDD	Silicon drift detector
SL	Singlelayer
TDLDA	Time dependent local density approximation
TEM	Transmission electron microscopy
TFY	Total fluorescence yield
TPA	Transition potential approximation
XANES	X-ray absorption near edge structure
XAS	X-ray absorption spectroscopy
XRD	X-ray Diffraction
XRR	X-ray reflectivity
XRS	X-ray Raman scattering

1 Introduction

Most macroscopic properties of material originate in its local atomic and electronic structure. It is the understanding of these structures on the microscopic length scale and the interactions involved that drive condensed matter physicists. Manipulation of the local atomic and electronic structure may help develop new materials or modify properties of existing materials for dedicated demands. High temperature and pressure can induce changes in the local atomic and electronic structure; studies on these changes in complex materials are presented in this thesis. Questions raised from diverse fields such as materials science and design, fundamental solid state physics, and the geosciences will be addressed.

Structural investigations on the atomic length scale are routinely performed for systems that exhibit long range order, e.g. using elastic x-ray or neutron scattering.[1] In the case of disordered systems, however, this task turns out to be much more challenging and the measured quantities oftentimes only represent averages of the local structure over space and time. Here, the study of absorption edges was proven tremendously important to examine the local electronic and atomic structure even in disordered systems.[2] In an x-ray absorption spectroscopy (XAS) experiment, the unoccupied density of electronic states is probed via the generation of a photoelectron from an inner core shell. This makes XAS an element selective probe since the electronic binding characteristics vary across the periodic table of elements. Measuring the unoccupied density of states provides details of the electronic structure of the investigated material and is sensitive especially to e.g. bond formation and changes in bonding.[3] This also implies the indirectness of XAS as there is no direct correlation between spectral features and the atomic structure. Usually structural information is extracted by comparison of spectral features to spectra of known materials or to simulated spectra of atomic models. However, even when the local structure cannot be revealed directly, XAS is very sensitive to structural changes.

For elements with electron binding energies in the hard x-ray regime, absorption edges can be measured bulk sensitively using XAS in fluorescence or transmission mode. When interested in bulk properties of light elements, especially when studied under extreme conditions, however, XAS fails as probe due to the limited penetration depth of soft x-rays in matter. Here, x-ray Raman scattering (XRS)[4], an energy loss spectroscopy which provides similar information as XAS, with primary x-ray energies in the hard x-ray regime

---

1 Als-Nielsen, J. and McMorrow, D. (2011). *Elements of modern X-ray physics.* Wiley; Hurd, A.J. and Sinha, S. (2010). *Neutrons & nanoscience (Neutron scattering applications & techniques).* Springer.

2 Koningsberger, D.C. and Prins, R. (1987). *X-ray absorption: principles, applications, techniques of EXAFS, SEXAFS and XANES.* John Wiley and Sons Inc., New York, NY; Rehr, J.J. and Albers, R.C. (2000). *Rev. Mod. Phys.* **72**, 621–654.

3 Pylkkänen, T. (2011). "Disordered matter studied by x-ray Raman scattering." PhD thesis. University of Helsinki.

4 Schülke, W. (2007). *Electron dynamics by inelastic X-ray scattering.* Vol. 7. Oxford University Press, USA.

can be used.

This thesis summarizes studies where x-ray spectroscopy is utilized to study the local structure as well as structural changes induced by elevated temperatures and/or pressure in different complex materials such as amorphous germanium and germanium-silicon oxides, barium clathrates, silicate glasses and melts, and supercritical water.

The thesis is organized as follows. **Chapter 2** summarizes important relations from the theoretical framework of the techniques used. A short description of the program packages used to model absorption edges from first principles is also given.

In **chapter 3** a descriptive overview of the experimental endstations used is provided and the experimental details of the presented studies are summarized shortly.

A series of three studies of the phase separation and germanium nanocrystal formation in oxide matrices is reported in **chapter 4**. The discovery of light emission from nanostructured silicon[5] in the early 1990s attracted vast attention and gave rise to numerous studies of the properties of nanostructured semiconductors aiming at novel diverse and attractive applications such as new photoluminescent devices[6], fast and small non-volatile flash memory[7], and highly efficient photo-voltaic cells[8]. In this respect materials of nanocrystalline semiconductors especially silicon and germanium nanocrystals embedded in oxide matrices proved promising over e.g. porous silicon because of the high stability and durability of oxide matrix embedded nanocrystals. One of the production pathways for these oxide matrix embedded nanocrystals is the temperature induced phase separation of germanium monoxide which ultimately leads to the formation of nanocrystals. This temperature induced local atomic reordering was studied using XAS and x-ray diffraction (XRD). Special attention is payed to the formation of size controlled nanocrystals in oxide matrices.

Chapter 5 summarizes the results of two studies aimed at the understanding of the pressure induced phase transitions in barium intercalated silicon clathrates. These complex cage-like structures exhibit numerous interesting physical properties like superconductivity and thermoelectric behavior.[9] The structural details and interactions between the intercalated guest atoms and the Si host network are of tremendous importance for the understanding of the mechanisms leading to the observed properties. In a first investigation the influence of the local atomic environment of the Ba atoms on the Ba giant resonance[10] is investigated using XRS and calculations employing a real space multiple scattering formalism. For the barium intercalated silicon clathrates Ba_8Si_{46} and $Ba_{24}Si_{100}$, several phase transitions without change in spacial symmetry were observed when high pressure is applied.[11] This peculiar behavior still defies a unified explanation and a second study aimed at an understanding of the underlying mechanisms is also presented in this chapter.

---

5 Iyer, S.S. and Xie, Y.H. (1993). *Science* **260**, 40.

6 Hirschman, K.D. et al. (1996). *Nature* **384**, 338–341; Godefroo, S. et al. (2008). *Nature Nanotech.* **3**, 174–178; Pavesi, L. et al. (2000). *Nature* **408**, 440–444.

7 Tiwari, S. et al. (1996). *Appl. Phys. Lett.* **68**, 1377.

8 Conibeer, G. (2007). *Mater. Today* **10**, 42–50.

9 San-Miguel, A. and Toulemonde, P. (2005). *High Pressure Res.* **25**, 159–185.

10 Connerade, J.P. et al. (1987). "Giant resonances in atoms, molecules, and solids."*NATO ASIB Proc. 151: Giant Resonances in Atoms, Molecules, and Solids.* Vol. 1.

11 San-Miguel, A. et al. (2002). *Phys. Rev. B* **65**, 054109; Toulemonde, P. et al. (2011). *Phys. Rev. B* **83**, 134110.

The influence of high pressure and high temperature conditions on the local atomic environment of water and silicate melts was investigated using XRS and the results are summarized in **chapter 6**. High temperature and high pressure conditions give rise to structural reordering processes in the earth's interior. Numerous pressure induced phase transitions, such as the discontinuities found in the earth's mantle, are known to occur.[12] Contrary to our intuitive perception, the earth needs to be viewed as a vibrant and dynamic system, most obviously witnessed through volcanism and earth quakes. For the geological processes in the earth's crust, water plays a key role. In subduction zones substantial amounts of water are dragged into the crust and upper mantle. High pressure and temperature conditions also lead to a considerable take up of water by silicate melts, a major constituent of the earth in these depths. The intake of water was shown to influence physical and transport properties of these melts.[13] First measurements aiming at the understanding of structural changes in silicate melts upon intake of water are also presented in this chapter.

The thesis concludes with a summary and outlook which is given in **chapter 7**.

[12] Marshak, S. (2004). *Essentials of geology*. WW Norton.

[13] Mysen, B.O. and Richet, P. (2005). *Silicate glasses and melts: Properties and structure*. Vol. 10.

2 Theory of inelastic x-ray scattering

In this chapter, an overview of the theoretical background of inelastic x-ray scattering (IXS) will be given. The physical quantity which is accessible in an IXS experiment, namely the double differential scattering cross-section (DDSCS), will be derived from basic principles of the interaction of x-rays with matter. Special attention will be payed to the aspects important for the experimental methods used in this thesis. In particular, non-resonant inelastic x-ray scattering (NRIXS) of core electrons, often referred to as non-resonant x-ray Raman scattering (XRS), and the resonant inelastic x-ray scattering (RIXS) process that enables one to measure an x-ray absorption edge using the fluorescence yield technique will be discussed in detail. In the remainder of this chapter, different approaches to calculate *ab initio* the cross-sections of the respective techniques will be presented shortly.

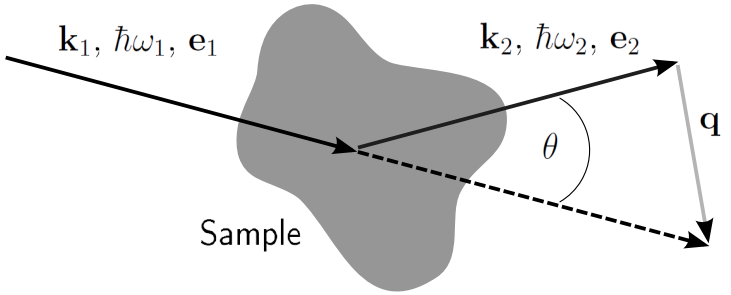

Figure 2.1: Schematic drawing of a typical inelastic scattering experiment. X-rays with wave vector $\mathbf{k}_1$, energy $\hbar\omega_1$ and polarization $\mathbf{e}_1$ are scattered by the sample into wave vector $\mathbf{k}_2$, energy $\hbar\omega_2$ and polarization $\mathbf{e}_2$ such that the energy $\hbar\omega = \hbar\omega_1 - \hbar\omega_2$ and the momentum $\hbar\mathbf{q} = \hbar\mathbf{k}_1 - \hbar\mathbf{k}_2$ are transferred to the scattering system.

2.1 The double differential scattering cross-section

The outline of a typical inelastic scattering experiment is given in Fig. 2.1. A monochromatic x-ray beam of wave vector $\mathbf{k}_1$, energy $\hbar\omega_1$, and polarization $\mathbf{e}_1$ hits the sample, interacts with it and is scattered. During the interaction the system, characterized by its eigenstate $|\mathrm{i}\rangle$ and eigenvalue E_i, can be excited into another state. The scattered radiation with wave vector $\mathbf{k}_2$, energy $\hbar\omega_2$, and polarization $\mathbf{e}_2$ is detected such that a scattering vector $\mathbf{q}$ is defined by the solid angle element of the detector Ω_2 and the energy $\hbar\omega_2$ of the scattered radiation is analyzed. Since the transferred energy $\hbar\omega = \hbar\omega_1 - \hbar\omega_2$ is usually small compared to the incident energy, the modulus of the transferred momentum is well approximated by

$$\mathrm{q} = 2\mathrm{k}_1 \sin(\theta/2). \tag{2.1}$$

In most inelastic scattering experiments, as is the case for the experiments carried out in the scope of this work, the polarization $\mathbf{e}_2$ of the scattered radiation is not analyzed. In brief, the measured quantity of an IXS experiment is the double differential scattering cross-section which can be described as[1]

$$\frac{\mathrm{d}^2\sigma}{\mathrm{d}\Omega_2 \mathrm{d}\hbar\omega_2} = \frac{\begin{array}{c}\text{current of photons scattered into solid angle element } [\Omega_2, \Omega_2 + \mathrm{d}\Omega_2] \\ \text{and into the range of energies } [\hbar\omega_2, \hbar\omega_2 + \mathrm{d}\hbar\omega_2]\end{array}}{\text{current density of the incident photons} \times \mathrm{d}\Omega_2 \times \mathrm{d}\hbar\omega_2}. \tag{2.2}$$

In what follows, the DDSCS shall be derived from basic principles of the interaction of x-rays with matter. Following Blume[2] and thus Schülke[3], the derivation of the DDSCS starts with writing down the non-relativistic (to the order of $(v/c)^2$) Hamiltonian for a number of j electrons in a quantized electromagnetic field:

$$\begin{aligned}\mathbf{H} = & \frac{1}{2m}\sum_j \left(\mathbf{p}_j - \frac{e}{c}\mathbf{A}(\mathbf{r}_j)\right)^2 + \sum_{jj'} \mathbf{V}(\mathbf{r}_{jj'}) \\ & - \frac{e\hbar}{2mc}\sum_j \sigma_j \cdot \nabla \times \mathbf{A}(\mathbf{r}_j) - \frac{e\hbar}{4m^2c^2}\sum_j \sigma_j \cdot \mathbf{E}(\mathbf{r}_j) \times \left[\mathbf{p}_j - \frac{e}{c}\mathbf{A}(\mathbf{r}_j)\right] \\ & + \sum_{\mathbf{k}\lambda} \hbar\omega_{\mathbf{k}} \left[c^+(\mathbf{k}\lambda)c(\mathbf{k}\lambda) + \frac{1}{2}\right].\end{aligned} \tag{2.3}$$

Here, m is the electron mass, e the elementary electric charge, and c is the speed of light. $c^+(\mathbf{k}\lambda)$ and $c(\mathbf{k}\lambda)$ are the creation and annihilation operators and σ are the Pauli spin matrices. The first term in (2.3) represents the kinetic energy of the electrons in the presence of the photon field. Here, $\mathbf{p}_j$ is the jth electron's momentum operator, $\mathbf{A}(\mathbf{r}_j)$ the operator of the vector potential of the electromagnetic field at the position $\mathbf{r}_j$ of the jth electron. The second term corresponds to the potential energy of the interacting electron system. The third and fourth term are the potential energy of the magnetic moment which is connected with the electrons' spin in the magnetic field of the radiation ($\nabla \times \mathbf{A}$) and with $(1/c)(\mathbf{v} \times \mathbf{E})$, respectively. $\mathbf{v}$ is the electron's velocity which is to be understood in terms of its canonical momentum $\mathbf{p}$. Since the magnetic structure of matter is not subject of interest in any of the experiments carried out in the scope of this thesis, spin dependent terms, i.e. those containing explicitly the vector potential $\mathbf{A}$ together with the Pauli spin matrices σ, will be omitted in what follows. However, the presence of these terms reveals the accessibility of magnetic properties by IXS. The last term of (2.3) is the energy of the photon field. The summation over $\mathbf{k}\lambda$ is to be understood over all modes of the photon field, where $\mathbf{k}$ is the wave vector and λ is counting the polarization directions.

---

1 Schülke, W. (2007). *Electron dynamics by inelastic X-ray scattering*. Vol. 7. Oxford University Press, USA.

2 Blume, M. (1985). *J. Appl. Phys.* **57**, 3615–3618.

3 Schülke, W. (1991). *Handbook on Synchrotron Radiation*. Ed. by Brown, G. and Moncton, D.E. Elsevier Science Publishers; Schülke, W. (2007). *Electron dynamics by inelastic X-ray scattering*. Vol. 7. Oxford University Press, USA.

Following Schülke[4], the vector potential $\mathbf{A}(\mathbf{r})$ is expressed in terms of the photon creation and annihilation operators $c^+(\mathbf{k}\lambda)$ and $c(\mathbf{k}\lambda)$

$$\begin{aligned}\mathbf{A}(\mathbf{r}) = \sqrt{\frac{2\pi\hbar c^2}{V\omega_{\mathbf{k}}}}\sum_{\mathbf{k}\lambda}[&\mathbf{e}(\mathbf{k}\lambda)c(\mathbf{k}\lambda)\exp\left(i\mathbf{k}\cdot\mathbf{r} - i\omega_{\mathbf{k}}t\right)\\ &+ \mathbf{e}^*(\mathbf{k}\lambda)c^+(\mathbf{k}\lambda)\exp(-i\mathbf{k}\cdot\mathbf{r} + i\omega_{\mathbf{k}}t)\big]\,,\end{aligned} \tag{2.4}$$

using Coulomb gauge, introducing the scalar potential ϕ as in

$$\mathbf{E} = -\nabla\phi - \frac{1}{c}\dot{\mathbf{A}}\,, \tag{2.5}$$

and evaluating the square in the first term of (2.3), one can isolate terms which represent the interaction between the photon field and the electrons. These interaction terms will then be treated as a small perturbation within perturbation theory. The terms describing the interaction contain explicitly the vector potential $\mathbf{A}$

$$H_{i1} = \frac{e^2}{2mc^2}\sum_j \mathbf{A}^2(\mathbf{r}_j) \tag{2.6}$$

and

$$H_{i2} = -\frac{e}{mc}\sum_j \mathbf{A}(\mathbf{r}_j)\cdot\mathbf{p}_j. \tag{2.7}$$

The remaining parts of the Hamiltonian that do not contain $\mathbf{A}$ are the Hamiltonian describing the interacting unperturbed electron system

$$H_0 = \frac{1}{2m}\sum_j \mathbf{p}_j^2 + \sum_{jj'}\mathbf{V}(\mathbf{r}_{jj'}) + \frac{e\hbar}{4m^2c^2}\sum_j \sigma_j\cdot\left(\nabla\phi\times\mathbf{p}_j\right), \tag{2.8}$$

where the σ containing part is the spin-orbit coupling, and the Hamiltonian describing the radiation field

$$H_{\mathrm{R}} = \sum_{\mathbf{k}}\hbar\omega_{\mathbf{k}}\left(c^+(\mathbf{k}\lambda)c(\mathbf{k}\lambda) + \frac{1}{2}\right). \tag{2.9}$$

The scattering processes described here are one and two photon processes and since the vector potential $\mathbf{A}$ (2.4) is linear in the creation and annihilation operators H_{i1} contributes to the inelastic scattering cross-section in first order perturbation theory while H_{i2} will only contribute in second order perturbation theory. Using Fermi's golden rule, the DDSCS up to second order is given by

[4] Schülke, W. (2007). *Electron dynamics by inelastic X-ray scattering*. Vol. 7. Oxford University Press, USA.

$$\frac{\mathrm{d}^2\sigma}{\mathrm{d}\Omega_2 \mathrm{d}\hbar\omega_2} \propto \frac{2\pi}{\hbar} \left| \langle \mathrm{f}|H_{i1}|\mathrm{i}\rangle + \sum_n \frac{\langle \mathrm{f}|H_{i2}|\mathrm{n}\rangle \langle \mathrm{n}|H_{i2}|\mathrm{i}\rangle}{(E_\mathrm{i} - E_\mathrm{n})} \right|^2 \delta(E_\mathrm{i} - E_\mathrm{f}). \tag{2.10}$$

The initial state $|\mathrm{i}\rangle$ can be excited directly into the final state $|\mathrm{f}\rangle$ (first term in (2.10)) or via an intermediate state $|\mathrm{n}\rangle$. This intermediate state $|\mathrm{n}\rangle$ can be represented by either of the two Feynman diagrams depicted in Fig. 2.2. Thus, it may consist of a state where the incident photon has been annihilated first (Fig. 2.2 a) $|\mathrm{n}\rangle = |\mathrm{n}, 0\rangle$ or a state where the final photon has been created first $|\mathrm{n}, \mathbf{k}_1\lambda_1, \mathbf{k}_2\lambda_2\rangle$ (Fig. 2.2 b)).

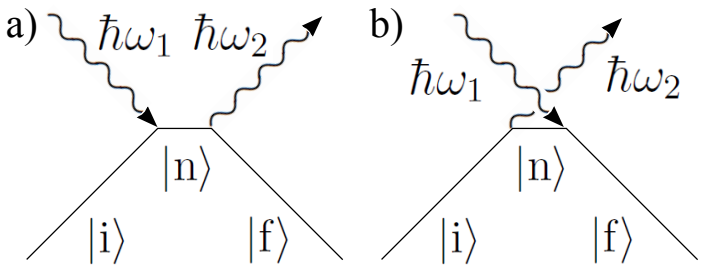

Figure 2.2: Feynman diagrams of the possible two-photon processes which result from second order perturbation treatment of H_{i2}: a) intermediate state where the incident photon has been annihilated first and b) state where the final photon has been created first.

Evaluation of (2.10) yields for the DDSCS

$$\begin{aligned}\frac{\mathrm{d}^2\sigma}{\mathrm{d}\Omega_2 \mathrm{d}\hbar\omega_2} = & \left(\frac{e^2}{mc^2}\right)^2 \left(\frac{\omega_2}{\omega_1}\right) \Bigg| (\mathbf{e_1}\cdot\mathbf{e}_2^*) \langle \mathrm{f}| \sum_j \exp(i\mathbf{q}\cdot\mathbf{r}_j)|\mathrm{i}\rangle \\ & + \frac{\hbar^2}{m} \sum_n \sum_{jj'} \Bigg(\frac{\langle \mathrm{f}|\mathbf{e}_2^*\cdot\mathbf{p}_j/\hbar \exp(-i\mathbf{k}_2\cdot\mathbf{r}_j)|\mathrm{n}\rangle \langle \mathrm{n}|\mathbf{e}_1\cdot\mathbf{p}_{j'}/\hbar \exp(i\mathbf{k}_1\cdot\mathbf{r}_{j'})|\mathrm{i}\rangle}{E_\mathrm{i} - E_\mathrm{n} + \hbar\omega_1 - i\Gamma_\mathrm{n}/2} \\ & + \frac{\langle \mathrm{f}|\mathbf{e}_1\cdot\mathbf{p}_j/\hbar \exp(i\mathbf{k}_1\cdot\mathbf{r}_j)|\mathrm{n}\rangle \langle \mathrm{n}|\mathbf{e}_2^*\cdot\mathbf{p}_{j'}/\hbar \exp(-i\mathbf{k}_2\cdot\mathbf{r}_{j'})|\mathrm{i}\rangle}{E_\mathrm{i} - E_\mathrm{n} - \hbar\omega_2} \Bigg) \Bigg|^2 \\ & \times \delta(E_\mathrm{i} - E_\mathrm{f} + \hbar\omega). \end{aligned} \tag{2.11}$$

This is the well known Kramers-Heisenberg formula[5] for the double differential scattering cross-section. It contains, assuming relativistic effects are negligible up to the order of $(v/c)^2$, all information about the interaction of x-rays with matter. Here, Γ_n is the energy broadening due to a finite core-hole lifetime ($\hbar/\Gamma_\mathrm{n}$) of the intermediate state $|n\rangle$. Resonant and non-resonant inelastic scattering are described if $|i\rangle \neq |f\rangle$, for $|i\rangle \equiv |f\rangle$ the Kramers-Heisenberg formula describes elastic scattering. The case for resonant and non-resonant x-ray scattering will be discussed in the next two sections.

[5] Kramers, H.A. and Heisenberg, W. (1925). *Z. Phys. A: Hadrons Nucl.* **31**, 681–708.

2.1.1 X-ray absorption and the resonant term

When $\hbar\omega_1 \approx E_\mathrm{n} - E_\mathrm{i}$ holds for the incident photon energy, the second term in (2.11) becomes the dominant contribution to the DDSCS. This is referred to as the resonant case and the cross section reduces to

$$\frac{\mathrm{d}^2\sigma}{\mathrm{d}\Omega_2 \mathrm{d}\hbar\omega_2} = \left(\frac{r_0}{m}\right)^2 \left(\frac{\omega_2}{\omega_1}\right) \sum_\mathrm{f} \sum_{jj'} \sum_\mathrm{n} \left| \frac{\langle \mathrm{f}|\mathbf{e}_2^* \cdot \mathbf{p}_j \exp(-i\mathbf{k}_2 \cdot \mathbf{r}_j)|\mathrm{n}\rangle \langle \mathrm{n}|\mathbf{e}_1 \cdot \mathbf{p}_{j'} \exp(i\mathbf{k}_1 \cdot \mathbf{r}_{j'})|\mathrm{i}\rangle}{E_\mathrm{i} - E_\mathrm{n} + \hbar\omega_1 - i\Gamma_\mathrm{n}/2} \right|^2 \delta(E_\mathrm{i} - E_\mathrm{f} + \hbar\omega). \tag{2.12}$$

Here, $r_0 = \frac{e^2}{mc^2}$ denotes the classical electron radius. Equation (2.12) describes the coherent excitation of a tightly bound core electron from an initial state $|\mathrm{i}\rangle$ into a short lived intermediate state $|\mathrm{n}\rangle$ and de-excitation of this intermediate state into a final state $|\mathrm{f}\rangle$. The adequate handling of the resonant denominator is taken care of by introducing the energy broadening of the resonance Γ_n which is, via the Heisenberg uncertainty principle, a consequence of the finite core-hole lifetime of the intermediate state.

Neglecting the coherence of excitation and de-excitation, this process may be sketched in a simplified single-particle picture as in Fig. 2.3 a). Part b) of the same figure illustrates the energy diagram for such a process.

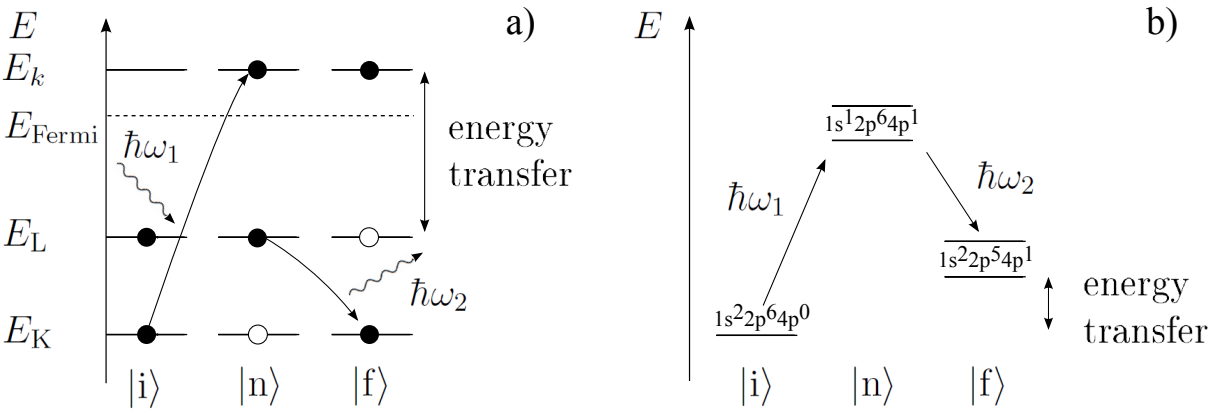

Figure 2.3: a) Sketch of a RIXS process in the single particle picture. $|\mathrm{i}\rangle$ is the initial, $|\mathrm{n}\rangle$, and $|\mathrm{f}\rangle$ are the intermediate and final state, respectively. See text for details. b) Exemplary energy diagram for an excitation and de-excitation process as depicted in a).

The initial state consists of an incident photon $(\mathbf{k}_1, \hbar\omega_1, \mathbf{e}_1)$ and an electron in a bound core state ($|\mathrm{i}\rangle$). Depending on the energy of the incident photon and the symmetry of the initial state, the core electron is excited into either an unoccupied bound state or a free photo-electron state. This stresses how the unoccupied electronic states of the according symmetry are probed by the core-electron excitation. The intermediate state consists of a hole in a deep core state and an electron in a formerly unoccupied level. In the de-excitation process, the intermediate state decays into the final state by filling

the core hole with an electron from a bound state. Excitation and de-excitation have to obey the selection rules due to the conservation of angular momentum. In the hard x-ray regime this decay is mostly radiative and a photon with wave vector $\mathbf{k}_2$, energy $\hbar\omega_2$, and polarization $\mathbf{e}_2$ is emitted. It is worth mentioning that, although the entire resonant scattering process has to satisfy energy conservation, the excitation process from the initial into the intermediate state is, due to the short lifetime ($\hbar/\Gamma_n$) of the intermediate state, not strictly limited by energy conservation[6].

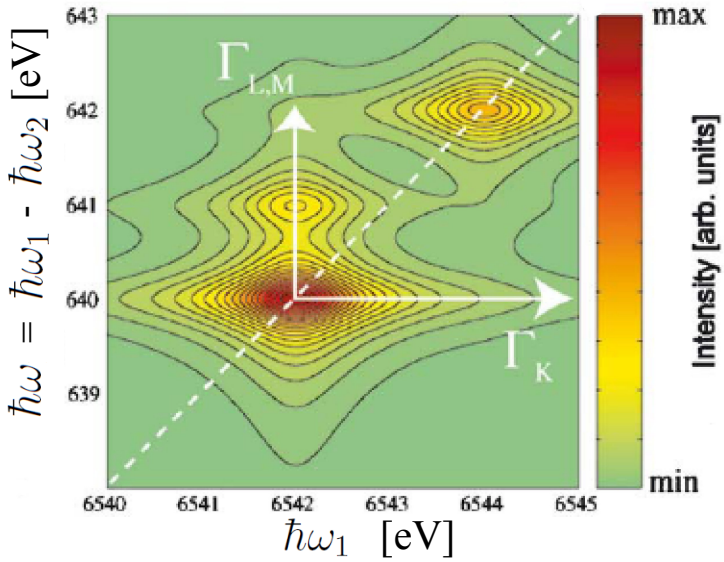

Figure 2.4: Calculated RIXS plane for a process as sketched in Fig. 2.3. Γ_K and $\Gamma_{L,M}$ are the lifetime broadening of the K shell core hole and the final state (hole in the L or M shell), respectively. Image taken from Glatzel, P. and Bergmann, U. (2005). *Coord. Chem. Rev.* **249**, 65–95.

In a RIXS experiment, the energy transfer $\hbar\omega = \hbar\omega_1 - \hbar\omega_2$ is measured for a variety of incident energies by an energy analysis of the emitted radiation. The information can be displayed in the so called RIXS plane, a two dimensional contour plot where the recorded intensity is plotted versus the energy transfer in one direction and the incident energy in the other. Such a theoretical RIXS plane taken from Glatzel *et al.*[7] for a process as depicted in Fig. 2.3 is shown in Fig. 2.4, exemplarily. The energy broadening due to the finite K shell intermediate state (core hole) lifetime Γ_K and the finite lifetime of the final state, $\Gamma_{L,M}$, are shown as arrows in the horizontal (incident energy) and vertical (energy transfer) directions, respectively.

In many cases, recording the entire RIXS plane is tedious and/or even unnecessary. As in this work, it is oftentimes sufficient to monitor the intensity of an emission line while scanning the incident energy across the absorption edge. This is often referred to as partial fluorescence yield (PFY) detection and, since the total intensity of an emission line is proportional to the absorption probability of x-rays, this is also referred to as x-ray absorption spectroscopy (XAS). Thus, in terms of inelastic x-ray scattering, a PFY-XAS

[6] Schülke, W. (2007). *Electron dynamics by inelastic X-ray scattering.* Vol. 7. Oxford University Press, USA.

[7] Glatzel, P. and Bergmann, U. (2005). *Coord. Chem. Rev.* **249**, 65–95.

scan is equivalent to a diagonal cut through the RIXS plane as $\hbar\omega_2$ is fixed. In PFY, the RIXS cross section reduces to a function of the incident energy $\hbar\omega_1$ at a fixed value of $\hbar\omega_2$. Setting $E_\mathrm{f} + \hbar\omega_2 = E_\mathrm{n}$, and thus fixing $\hbar\omega_2$ to the maximum of the fluorescence line, the cross section can be written as[8]

$$\begin{aligned}\sigma_\mathrm{PFY}(\omega_1) \propto & \sum_\mathrm{n} |\langle \mathrm{n}|T|\mathrm{i}\rangle|^2 \\ & \times \left(\frac{1}{(E_\mathrm{i} - E_\mathrm{n} + \hbar\omega_1)^2 + \Gamma_\mathrm{n}^2/4}\right)\left(\frac{\Gamma_\mathrm{f}/\pi}{(E_\mathrm{n} - E_\mathrm{i} - \hbar\omega_1)^2 + \Gamma_\mathrm{f}^2/4}\right).\end{aligned} \tag{2.13}$$

The transition operator of the excitation process in (2.12) has been replaced by T for simplicity. In the dipole limit T reduces to $(\mathbf{e}_1 \cdot \mathbf{r})$. Compared to the full RIXS equation (2.12) the transition matrix element $\langle f|T^+|n\rangle$ is independent of the incident photon energy and since only one final state has to be considered (fixed $\hbar\omega_2$), the summation over f can be omitted. The energy conserving δ-function was represented by a Lorentzian with full width at half maximum Γ_f. This accounts for the finite lifetime of the final state. Equation (2.13) again stresses the sensibility of XAS to the unoccupied density of states (uDOS) since absorption is only possible for suitable unoccupied states $|\mathrm{n}\rangle$.

In an even more rigorous approach, the total fluorescence yield (TFY) which corresponds to an energy integration over $\hbar\omega_2$ is monitored e.g. by a simple pin diode detector which simplifies the experimental setup substantially. In case of TFY, the probability that an electron is excited from an initial into an intermediate state is given by

$$\sigma_\mathrm{TFY}(\omega_1) \propto \sum_\mathrm{n} |\langle \mathrm{n}|\mathbf{e}_1 \cdot \mathbf{r}|\mathrm{i}\rangle|^2 \, \delta(E_\mathrm{n} - E_\mathrm{i} - \hbar\omega_1). \tag{2.14}$$

To bring (2.14) into the form of (2.13) the δ-function can also be broadened into a Lorentzian

$$\sigma_\mathrm{TFY}(\omega_1) \propto \sum_\mathrm{n} |\langle \mathrm{n}|T|\mathrm{i}\rangle|^2 \, \frac{(\Gamma_\mathrm{n}/2\pi)}{(E_\mathrm{n} - E_\mathrm{i} - \hbar\omega_1)^2 + \Gamma_\mathrm{n}^2/4}. \tag{2.15}$$

Comparing (2.13) with (2.15), the PFY spectrum appears similar to the TFY, but with a spectral broadening that stems from the lifetime of the intermediate state as compared to the final state. Since the lifetime of the intermediate state $\hbar/\Gamma_\mathrm{n}$ is usually smaller than that of the final state $\hbar/\Gamma_\mathrm{f}$, RIXS allows one to investigate absorption edges with a resolution higher than in fluorescence or transmission XAS. In the example of Fig. 2.4 the energy broadening due to the lifetime of the 1s core-hole is responsible for the maximum energy resolution in TFY. In PFY, however, the energy broadening due to the lifetime of the hole in the 2p state will limit the maximum energy resolution. The 2p state is more weakly bound than the 1s state and the lifetime of a hole in a 2p state is usually longer than for a 1s core-hole. Since the lifetime is, via Heisenberg's uncertainty principle, inverse proportional to the energy broadening, PFY yields a higher resolution than TFY.

[8] Schülke, W. (2007). *Electron dynamics by inelastic X-ray scattering*. Vol. 7. Oxford University Press, USA.

This was first shown by Hämäläinen *et al.*[9] for the case of the Dysprosium L_3-edge.

Besides this electronic picture of XAS, it is oftentimes instructive to view the explicit form of an absorption edge as a result of a multiple scattering event of the photo-electron wave at the atoms surrounding the absorbing atom. The shape of the absorption edge is then modulated by the interference of the outgoing and backscattered photo-electron wave.[10] This multiple scattering event is depicted in Fig. 2.5 and demonstrates the sensitivity of absorption spectroscopy to the immediate surrounding of the absorber. In the direct vicinity of an absorption edge, the photo-electron has little kinetic energy and multiple scattering is strong. This region extends to a few 10 eV above an absorption edge and is often referred to as x-ray absorption near edge structure (XANES). XANES spectroscopy is thus sensitive to the exact shape of the scattering potentials, i.e. coordination chemistry, bond length and bond angles. Far above an absorption edge single scattering dominates as the photo-electron has higher kinetic energy. The region beyond the XANES region is called extended x-ray absorption fine structure (EXAFS). EXAFS spectroscopy yields information like next neighbor distances, angles, and coordination numbers.[11]

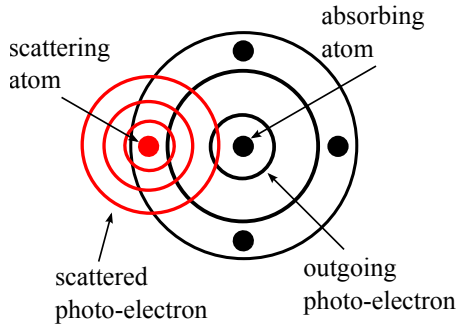

Figure 2.5: Cartoon of an emerging photo electron wave that scatters off of neighboring atoms. Interference of the emerging and backscattered photo electron wave modulate the absorption probability.

2.1.2 The dynamic structure factor $S(\mathbf{q}, \omega)$

The first term in (2.11) describes non-resonant (inelastic) scattering. When the incident energy $\hbar\omega_1$ is far away from the binding energy of an inner shell electron, the terms including an intermediate state $|\mathrm{n}\rangle$ in (2.10) are certainly small and can be neglected. In this case, only the term in the interaction Hamiltonian that is quadratic in the vector potential $\mathbf{A}$ contributes to the DDSCS and (2.10) can be simplified and rewritten as

$$\frac{\mathrm{d}^2\sigma}{\mathrm{d}\Omega_2 \mathrm{d}\hbar\omega_2} = r_0^2 \left(\frac{\omega_2}{\omega_1}\right) |\mathbf{e_1} \cdot \mathbf{e}_2^*|^2 \left| \langle \mathrm{f}| \sum_j e^{i\mathbf{q}\cdot\mathbf{r}_j} |\mathrm{i}\rangle \right|^2 \delta(E_\mathrm{i} - E_\mathrm{f} - \hbar\omega). \tag{2.16}$$

[9] Hämäläinen, K. et al. (1991). *Phys. Rev. Lett.* **67**, 2850–2853.

[10] Rehr, J.J. and Albers, R.C. (2000). *Rev. Mod. Phys.* **72**, 621–654.

[11] For more information about x-ray absorption spectroscopy (XAS) the reader is referred to Koningsberger *et al.* (Koningsberger, D.C. and Prins, R. [1987]. *X-ray absorption: principles, applications, techniques of EXAFS, SEXAFS and XANES*. John Wiley and Sons Inc., New York, NY) and Rehr *et al.* (Rehr, J.J. and Albers, R.C. [2000]. *Rev. Mod. Phys.* **72**, 621–654).

Usually (2.16) is written as

$$\frac{\mathrm{d}^2\sigma}{\mathrm{d}\Omega_2 \mathrm{d}\hbar\omega_2} = \left(\frac{d\sigma}{d\Omega_2}\right)_{\mathrm{Th}} S(\mathbf{q},\omega), \tag{2.17}$$

with the Thomson scattering cross-section which describes the photon-electron coupling

$$\left(\frac{\mathrm{d}\sigma}{\mathrm{d}\Omega_2}\right)_{\mathrm{Th}} = r_0^2 \left(\frac{\omega_2}{\omega_1}\right) |\mathbf{e_1}\cdot\mathbf{e}_2^*|^2, \tag{2.18}$$

and the dynamic structure factor

$$S(\mathbf{q},\omega) = \left|\langle \mathrm{f}| \sum_j e^{i\mathbf{q}\cdot\mathbf{r}_j} |\mathrm{i}\rangle\right|^2 \delta(E_\mathrm{i} - E_\mathrm{f} + \hbar\omega). \tag{2.19}$$

The delta-function ensures energy conservation.

In principle, $S(\mathbf{q},\omega)$ contains all information about the sample as an interacting many electron system by non-resonant scattering. Equation (2.19) stresses the inelastic scattering process as an electronic excitation from a ground state $|\mathrm{i}\rangle$ to an excited state $|\mathrm{f}\rangle$. Likewise, $S(\mathbf{q},\omega)$ can be expressed as a time dependent electron density fluctuation in the ground state

$$S(\mathbf{q},\omega) = \frac{1}{2\pi\hbar}\int_{-\infty}^{\infty} dt e^{-i\omega t} \langle \mathrm{i}| \sum_{jj'} e^{-i\mathbf{q}\cdot\mathbf{r}_{j'}(t)} e^{i\mathbf{q}\cdot\mathbf{r}_j(0)} |\mathrm{i}\rangle\,. \tag{2.20}$$

This formulation was first derived by van Hove[12] and q^{-1} and ω^{-1} determine the length and time scales probed. In yet another formulation, $S(\mathbf{q},\omega)$ can be related to the inverse of the dielectric function $\epsilon(\mathbf{q},\omega)$

$$S(\mathbf{q},\omega) = (1+\eta_\mathrm{B})\frac{q^2\hbar}{4\pi e^2}\mathrm{Im}\left[\frac{-1}{\epsilon(\mathbf{q},\omega)}\right], \tag{2.21}$$

where η_B is the Bose factor. Depending on the amount of energy and/or momentum transfered to the electron system, certain representations may be more intuitive than others. Thus, according to Schülke (2007), the different NRIXS experiments can be classified with respect to the information drawn from the experiment:

1. Valence electron excitations with $qr_c \approx 1$ and $\omega \approx \omega_p$ where the characteristic length r_c is the inter-particle distance and ω_p the plasmon frequency.
2. Scattering by inner-shell excitations or XRS with $\hbar\omega \approx E_\mathrm{B}$ and $qa \leq 1$ where E_B is the binding energy of an inner shell electron and a its orbital radius.
3. Phonon excitations with $qd \approx 1$ and $\omega \approx \omega_\mathrm{ph}$ where d is the inter-ionic distance and ω_ph is the phonon frequency.

[12] Hove, L. Van (1954). *Phys. Rev.* **95**,1, 249–262.

4. Compton scattering with $qr_c \gg 1$ and $\hbar\omega \gg E_0$, where E_0 is a characteristic energy of the system.

Only XRS was used in this work and thus formulation (2.19) is the most convenient representation for $S(\mathbf{q},\omega)$, for details of all other techniques the reader will be referred to the according literature (see Schülke[13] and references therein for a comprehensive overview).

Since in XRS the momentum transfer $\mathbf{q}$ is small, the transition operator in (2.19) can be expanded in a Taylor series

$$\langle \mathrm{f}|e^{i\mathbf{q}\cdot\mathbf{r}}|\mathrm{i}\rangle = i\,\langle \mathrm{f}|\mathbf{q}\cdot\mathbf{r}|\mathrm{i}\rangle - \frac{1}{2}\,\langle \mathrm{f}|(\mathbf{q}\cdot\mathbf{r})^2|\mathrm{i}\rangle + \mathcal{O}((\mathbf{q}\cdot\mathbf{r})^3). \tag{2.22}$$

The zeroth order term vanishes due to the orthogonality of initial and final state. The first term in the Taylor series describes dipole transitions and dominates for small $\mathbf{q}$. Here, the analogy of XRS and XAS, where only dipole transitions are allowed, becomes obvious.[14] In the single particle approximation the momentum transfer $\mathbf{q}$ in XRS takes over the role of the polarization $\mathbf{e}_1$ of the incident x-ray beam in XAS

$$\sigma_{\mathrm{XAS}}(\omega_1) \propto |\,\langle \mathrm{f}|\mathbf{e}_1\cdot\mathbf{r}|\mathrm{i}\rangle\,|^2\delta(E_\mathrm{i} - E_\mathrm{f} + \hbar\omega_1), \tag{2.23}$$

$$S(\mathbf{q},\omega) = |\,\langle \mathrm{f}|\mathbf{q}\cdot\mathbf{r}|\mathrm{i}\rangle\,|^2\delta(E_\mathrm{i} - E_\mathrm{f} + \hbar\omega). \tag{2.24}$$

Thus, the information content of $S(\mathbf{q},\omega)$ in the dipole limit and when $\hbar\omega \approx E_\mathrm{B}$ is formally the same as in XAS where $\hbar\omega_1 \approx E_\mathrm{B}$. However, since the energy loss ω does not depend on the incident energy, the incident energy can be chosen freely. Mostly, $\hbar\omega_1$ in an XRS experiment is of the order of 10 keV whereas the energy transfer is of the order of typical binding energies of low Z elements. This is a tremendous advantage of XRS when studying low Z absorption edges bulk sensitively and/or under extreme conditions and complicated sample environments that do not allow soft x-rays or electrons as probe. The drawback, however, is the small cross section of XRS compared to XAS such that XRS experiments are feasible only at dedicated experimental end-stations at $3rd$ generation synchrotron radiation sources.[15]

For higher momentum transfers, higher order terms in the Taylor series (2.22) contribute more significantly to $S(\mathbf{q},\omega)$ and thus, the study of multipole-transitions becomes feasible. The fact that also dipole forbidden transitions are accessible with XRS makes it sensible to the entire uDOS.[16]

---

13 Schülke, W. (2007). *Electron dynamics by inelastic X-ray scattering.* Vol. 7. Oxford University Press, USA.

14 Mizuno, Y. and Ohmura, Y. (1967). *J. Phys. Soc. Jpn.* **22**,2, 445–449.

15 An overview of the different experimental requirements needed and experimental setups used is given in chapter 3.

16 Soininen, J.A. et al. (2005). *Phys. Rev. B* **72**, 045136.

2.2 Simulating XAS and XRS spectra from first principles

The direct interpretation of XAS and XRS spectra is not straightforward and the analysis is either qualitative using the evolution of spectra with the variation of an experimental parameter or quantitative by comparison to reference spectra, if these are available. A different approach is to model the electronic structure of an atomic configuration and calculate from this the XAS or XRS spectra from first principles. Assuming the computational method gives accurate results, this provides a direct access to a structural model by comparison of the calculated and experimental spectra. In what follows, the three computational approaches used in the scope of this work shall be introduced and described shortly from an experimentalist's point of view. In particular, the program package FEFF, which allows the calculation of both XAS and XRS spectra, is described in section 2.2.1. The program package FDMNES, which can be used to calculate XAS spectra, is presented in section 2.2.2, and a short introduction to density functional theory, which is used by the StoBe-deMon program package, is given in section 2.2.3.

2.2.1 The real space multiple scattering formalism

The perception of the fine structure in XAS as a result of multiple scattering of the emerging photo-electron wave provides a convenient basis for the *ab initio* calculation of XAS and XRS spectra. This approach is called real-space multiple-scattering (RSMS) formalism and is implemented in the FEFF[17] program package[18]. The calculations are based on the fact that Fermi's golden rule (equations (2.15) and (2.19)) can be reformulated using a single-particle Green's function G as in

$$-(1/\pi)\,\mathrm{Im}\,G = \sum_{\mathrm{f}} |f\rangle\,\langle f|\,\delta(E - E_{\mathrm{f}}). \tag{2.25}$$

For the case of XAS and XRS, the golden rule then becomes[19]

$$\sigma(E) \propto -\frac{2}{\pi}\,\mathrm{Im}\,\langle i|\mathbf{e}\cdot\mathbf{r}'G(\mathbf{r}',\mathbf{r},E)\mathbf{e}\cdot\mathbf{r}|i\rangle \tag{2.26}$$

and

$$S(\mathbf{q},\omega) \propto -\frac{2}{\pi}\,\mathrm{Im}\,\langle i|e^{-i\mathbf{q}\cdot\mathbf{r}'}G(\mathbf{r}',\mathbf{r},E)e^{i\mathbf{q}\cdot\mathbf{r}}|i\rangle\,. \tag{2.27}$$

Since the computation of the final state wave function $|\mathrm{f}\rangle$ is usually challenging because it needs to be calculated in the presence of a (possibly) screened core hole, one apparent advantage of this formulation is that $|\mathrm{f}\rangle$ does not appear explicitly in equation (2.26). In-

[17] The name FEFF stems from the effective scattering amplitude f_{eff} introduced by Rehr *et al.* (Rehr, J.J. and Albers, R.C. (1990). *Phys. Rev. B* **41**, 8139). Within this thesis the program package FEFF9 was used to calculate absorption edges, the program package FEFFq was utilized for all q dependent XRS calculations.

[18] Rehr, J.J. et al. (2010). *Phys. Chem. Chem. Phys.* **12**, 5503–5513.

[19] Ankudinov, A.L. et al. (1998). *Phys. Rev. B* **58**, 7565; Soininen, J.A. et al. (2005). *Phys. Rev. B* **72**, 045136.

stead, the one-electron Green's function $G = (E - H + i\Gamma)^{-1}$ with the effective one-electron Hamiltonian $H = H_0 + \sum_n v_n$ and the photo-electron energy E needs to be calculated. This effective one-electron Hamiltonian H is given by the free electron Hamiltonian H_0 and the scattering potentials v_n at the according atomic site n within a finite cluster[20]. Within the program package FEFF, the atomic scattering potentials v_n are approximated by muffin tin potentials which are calculated self consistently (self consistent field (SCF) method) by iterating the total electron density, the potential, and the Fermi energy.[21] The Green's function $G_{L'R',LR}$, i.e. the amplitude for an electron to propagate from a state $|LR\rangle$ into state $|L'R'\rangle$, where R denotes the site and $L = (l, m)$ the angular momentum, can be calculated as

$$G = G^{\mathrm{c}} + G^{\mathrm{sc}}. \tag{2.28}$$

G^{c} represents the contribution from the central atom $(-1/\pi)\,\mathrm{Im}\,G^{\mathrm{c}} = \delta_{R,R'}\delta_{L,L'}$ and G^{sc} denotes the scattering from the surrounding atoms which, using the free propagator G^0, is given by the implicit functional Dyson equation

$$G^{\mathrm{sc}} = G^0 t G^0 + G^0 t G^0 t G^0 + \cdots . \tag{2.29}$$

Here, t is the scattering matrix and scattering from all single scattering paths ($G^0 t G^0$), double scattering paths ($G^0 t G^0 t G^0$), etc. are summed up. In many cases, this so called path expansion converges well, especially at high photo-electron energies[22], and (2.29) can be truncated after a finite number of paths. At low photo-electron energies[23], however, multiple scattering is strong and it may be necessary to include all scattering paths. This is accounted for by calculating the full multiple scattering (FMS) using

$$G^{\mathrm{sc}} = (1 - G^0 t)^{-1} G^0, \tag{2.30}$$

which involves a numerically challenging matrix inversion. However, since the mean free path of the photo-electron in the vicinity of an absorption edge, i.e. where the path expansion fails, is of the order of $1 - 5$ Å, only a relatively small cluster with the order of 10^2 atoms needs to be taken into account.

For the calculation of inelastic x-ray scattering cross sections, i.e. XRS spectra, the momentum transfer $\mathbf{q}$ has to be considered. In order to find the weights of the various excitation channels, the final state density matrix is represented in an angular momentum $(L = l, m)$ and site $\mathbf{R}$ basis $|L, \mathbf{R}\rangle$ and rewriting $S(\mathbf{q}, \omega)$ gives

$$S(\mathbf{q}, \omega) = \sum_{LL'} M_L(-\mathbf{q}, E)\rho_{LL'}(E)M_{L'}(\mathbf{q}, E). \tag{2.31}$$

Here, $M_L(\mathbf{q}, E) = \langle R_L(E)|e^{i\mathbf{q}\cdot\mathbf{r}}|i\rangle$ are the atomic transition matrix elements describing the transition from initial states $|\mathrm{i}\rangle$ into exited states with energy $E = E_{\mathrm{i}} + \hbar\omega$ and L-type angular momentum. The empty states are described by the matrix elements $\rho_{LL'}(E)$

[20] This bears the advantage of being able to account for periodic and aperiodic systems alike.
[21] Soininen, J.A. et al. (2005). *Phys. Rev. B* **72**, 045136.
[22] I.e. the EXAFS regime.
[23] I.e. the XANES region.

of the final states density matrix.[24] In polycrystalline materials or materials with cubic symmetry, equation (2.31) can be simplified to

$$S(\mathbf{q},\omega) = \sum_l (2l+1)\,|M_l(\mathbf{q},E)|^2\,\rho_l(E). \tag{2.32}$$

Since the matrix elements $M_l(q,E)$ are inherently atomic properties, they can be calculated reliably by the FEFF program package, and the lDOS is extractable directly by measuring $S(\mathbf{q},\omega)$ parametrically for several values of $\mathbf{q}$ and solving equation (2.32).[25]

2.2.2 The finite difference method to calculate $\sigma_{\mathrm{XAS}}(\omega_1)$

A drawback of the *ab initio* calculation scheme used by FEFF is the rather rudimentary approximation of the atomic scattering potentials by muffin-tin like potentials. As mentioned earlier in most cases the exact form and shape of the scattering potentials is not essential and remarkable agreement can be achieved between experiment and the Green's function approach described in section 2.2.1. This holds especially far above the absorption edge onset, i.e. in the EXAFS regime, where the interaction between the photo-electron and the scattering potentials is weak. In the direct vicinity of an absorption edge where the interaction of photo-electron and the scattering potentials is strong, however, the muffin-tin approximation may fail and the use of a more realistic scattering potential is inevitable.

The initial state is usually an atomic core orbital and can be calculated straightforwardly whereas the computation of the final state is quite demanding. Instead of using the Green's function formalism described in section 2.2.1 which uses the muffin tin approximation for the atomic scattering potentials, the program package FDMNES uses the finite difference method (FDM)[26] to solve the Schrödinger equation for the wave functions. This is performed on a discretized three dimensional grid in real space and the unknowns are the values of the wave function at each of the grid points in a spherical volume around an absorbing atom.[27] As potentials a superposition of atomic densities are used as a starting point for a self consistent field iteration similar to the case in the FEFF program package. The Coulomb potential is calculated from the densities via Poisson's equation and a Hedin-Lundqvist type exchange-correlation potential[28] is accounted for. If the core hole-photo-electron interaction is small, i.e. the core hole is screened well, electronic densities, as calculated from ground state band structure programs, can be used as input for FDMNES.

A considerable drawback of the FDM approach for calculating absorption edges is the numerically expensive calculation of the final states despite the discretization. This limits the applicability of this method to relatively small clusters and the near edge features. However, since the exact shape of the scattering potentials is less important far away from an absorption edge, calculations using the muffin tin approximation are well suited for this task. Up to date, a finite momentum transfer, as needed for the calculation of XRS

[24] Soininen, J.A. et al. (2005). *Phys. Rev. B* **72**, 045136.
[25] Soininen, J.A. et al. (2005). *Phys. Rev. B* **72**, 045136.
[26] Kimball, G.E. and Shortley, G.H. (1934). *Phys. Rev.* **45**, 815.
[27] Joly, Y. (2001). *Phys. Rev. B* **63**, 125120.
[28] Hedin, L. and Lundqvist, B.I. (1971). *J. Phys. C: Solid State Phys.* **4**, 2064.

spectra, cannot be accounted for within the FDMNES program package.

2.2.3 The Kohn-Sham Density Functional Theory approach to XAS and XRS

A very different approach than described in the last two sections is based on the famous density functional theory (DFT)[29]. It is based on the fact, that the energy of a many particle wave function $|\Psi\rangle$ can be calculated as

$$E\{|\Psi\rangle\} = \frac{\langle\Psi|H|\Psi\rangle}{\langle\Psi|\Psi\rangle}, \tag{2.33}$$

and each wave function is linked to a density

$$\rho(\mathbf{r}) = \langle\Psi|\sum_i \delta(\mathbf{r}-\mathbf{r}_i)|\Psi\rangle\,. \tag{2.34}$$

Hohenberg and Kohn showed[30] that there exists a ground state density $\rho_0(\mathbf{r})$ which uniquely minimizes this functional, i.e. the density $\rho_0(\mathbf{r})$, for which the functional

$$E\{\rho(\mathbf{r})\} = \langle\Psi|H|\Psi\rangle \tag{2.35}$$

is minimal, is the ground state density and the according value of the functional $E_0 = E\{\rho_0(\mathbf{r})\}$ is the ground state energy of the system. Thus, instead of trying to solve the Schrödinger equation for a system of N interacting particles, one has to find a density (in three spatial dimensions) which minimizes the functional (2.35). This leads to the variational problem

$$\delta E\{\rho(\mathbf{r})\} = 0, \tag{2.36}$$

for which Kohn and Sham have introduced a procedure that leads to the Kohn-Sham equations[31]

$$\left(-\frac{\hbar^2}{2m}\nabla + V_{\text{eff}}(\mathbf{r})\right)\psi_i(\mathbf{r}) = \epsilon_i\psi_i(\mathbf{r}), \tag{2.37}$$

with the Kohn-Sham orbitals $\psi_i(\mathbf{r})$, their eigenvalues ϵ_i, and the effective single-particle potential

$$V_{\text{eff}}(\mathbf{r}) = V(\mathbf{r}) + \int d\mathbf{r}'\frac{e^2}{|\mathbf{r}-\mathbf{r}'|}\rho(\mathbf{r}') + \frac{\delta E_{\text{xc}}\{\rho(\mathbf{r})\}}{\delta\rho(\mathbf{r})}. \tag{2.38}$$

Here, $V(\mathbf{r})$ is the external potential, e.g. of the nuclei, $\int d\mathbf{r}'\frac{e^2}{|\mathbf{r}-\mathbf{r}'|}\rho(\mathbf{r}')$ the classical electrostatic interaction between the electrons, and $V_{\text{xc}}(\mathbf{r}) = \delta E_{\text{xc}}\{\rho(\mathbf{r})\}/\delta\rho(\mathbf{r})$ the exchange-

[29] A detailed and comprehensive introduction to DFT is, e.g., given by Fiolhais, C. et al. (2003). *A primer in density functional theory.* Vol. 620. Springer Verlag.

[30] Hohenberg, P. and Kohn, W. (1964). *Phys. Rev.* **136**, B864.

[31] Kohn, W. and Sham, L.J. (1965). *Phys. Rev.* **140**, 1133–1138.

correlation potential which contains all many body quantum mechanical effects. Thus, the Kohn-Sham equations describe non-interacting electrons in an effective potential, where all many-body effects are accounted for by an effective potential $V_{\text{eff}}(\mathbf{r})$. Since the unknown density $\rho(\mathbf{r}) = \sum_i |\psi_i(\mathbf{r})|^2$ is itself a factor in the effective potential, (2.37) has to be solved self consistently. The exchange-correlation potential is also generally unknown and thus has to be approximated, however, a considerable number of approximations exist.[32]

Although the Kohn-Sham orbitals $\psi_i(\mathbf{r})$ are only used to construct the density $\rho(\mathbf{r})$ and thus have no direct physical meaning, they are often used as approximations to the actual single particle wave functions. Using the StoBe-deMon code[33] equations (2.37) can be solved self-consistently for a small cluster of atoms and the resulting Kohn-Sham orbitals and their energies can be used to calculate XAS and XRS spectra via equations (2.23) and (2.24), respectively. As pointed out in sections 2.2.1 and 2.2.2, the final state has to be calculated in the presence of a core hole. This is circumvented using the transition potential approximation (TPA)[34] to the transition state approach by Slater[35]. Within the TPA, the initial and final states are calculated at the same time with a half core hole in the initial state and a half core hole in the final state. As a starting point for the iterative calculation of the Kohn-Sham orbitals, the StoBe-deMon code uses a linear combination of Gaussian type orbitals to solve the Kohn-Sham equations. A number of approximations to the exchange-correlation interaction potential like the local density approximation (LDA) and several parametrizations of the generalized gradient approximation (GGA) are implemented. In case there are several equivalent absorbing atoms in the atomic cluster, model core potentials can be used for all non-excited atoms of the same kind to ensure the localization of the core hole. The calculation of x-ray absorption spectra is readily included in the StoBe-deMon program package. The computation of XRS spectra was recently described by Sakko *et al.*[36]. For all practical comparisons to experimental data, the calculated spectra have to be broadened to mimic experimental and lifetime broadening as well as the continuum part of the spectra. This is usually achieved by convolution of the calculated spectra with a Gaussian or Lorentzian with energy dependent full width at half maximum (FWHM).[37]

---

[32] Fiolhais, C. et al. (2003). *A primer in density functional theory.* Vol. 620. Springer Verlag.

[33] Hermann, K. et al. *http://w3.rz-berlin.mpg.de/hermann/StoBe/index.html.*

[34] Triguero, L. et al. (1998). *Phys. Rev. B* **58**, 8097.

[35] Slater, J.C. and Johnson, K.H. (1972). *Phys. Rev. B* **5**, 844.

[36] Sakko, A. et al. (2007). *Phys. Rev. B* **76**, 205115.

[37] Leetmaa, M. et al. (2010). *J. Electron. Spectrosc. Relat. Phenom.* **177**, 135–157; Hetenyi, B. et al. (2004). *J. Chem. Phys.* **2004**, 120.

3 Experimental Setups

The experiments presented in this thesis were all carried out using hard x-rays with photon energies of the order of 10 keV. Since an x-ray source which allows tuning the x-ray energy combined with a high photon flux is necessary for absorption spectroscopy and inelastic x-ray scattering experiments, all experiments were carried out at synchrotron radiation facilities. The experimental setups used will be described in this chapter. All x-ray absorption spectroscopy experiments were performed at the DELTA[1] beamline BL8. The setup of this beamline will be described first. Due to the small cross section for non-resonant inelastic x-ray scattering, all XRS experiments were carried out at the third generation synchrotron radiation facilities ESRF[2] and APS[3]. The unique setup of beamline ID16 (ESRF) for inelastic x-ray scattering allows experiments under extreme conditions like high temperatures and high pressures and will be described in section 3.2. In section 3.3 the IXS beamline 20-ID-B at the APS will be introduced. This beamline provides an exceptional setup to measure a large range of momentum transfers simultaneously. In the last section of this chapter, the XRD setup of the DELTA beamline BL9 is presented shortly.

3.1 DELTA beamline BL8

The general outline of the materials science beamline BL8[4] of the 1.5 GeV storage ring DELTA is depicted in a schematic drawing in Fig. 3.1 a). A photograph of the experimental end-station is provided in Fig. 3.1 b). Beamline BL8 is the first of three beamlines that are supplied with synchrotron radiation from a 5.3 T asymmetric wiggler. The radiation is monochromatized by a Si(111) double crystal monochromator and can be collimated using slits. Typically, spot sizes on the sample were chosen to be 1×3 mm^2 (V $\times$ H).

In order to measure the incident photon flux on the sample, the monochromatic x-ray beam passes through an argon filled ionization chamber and a photo-ion current proportional to the incident photon flux was used to normalize the data in all experiments. The absorption cross section is proportional to the fluorescence[5] intensity which was detected by three fluorescence detectors. Here, a Canberra Passivated Implanted Planar Silicon (PIPS) diode and two Amptek silicon drift diode (SDD) detectors were employed. The PIPS detector measures the total fluorescence yield, whereas the SDD detectors can measure energy dispersively such that the intensity of a single emission line[6] can

---

1 Dortmunder Elektronen Speicherring Anlage, Dortmund, Germany.

2 European Synchrotron Radiation Facility, Grenoble, France.

3 Advanced Photon Source at the Argonne National Laboratories, Argonne, USA.

4 Lützenkirchen-Hecht, D. et al. (2009). *J. Synchrotron Rad.* **16**, 264–272.

5 $\sigma(E) \propto I_f/I_0$, where I_0 is the incident and I_f the fluorescence intensity, respectively.

6 In all experiments, the Ge K_{α_1} was monitored; the energy resolution of the SDD detectors is of the order of 150 eV.

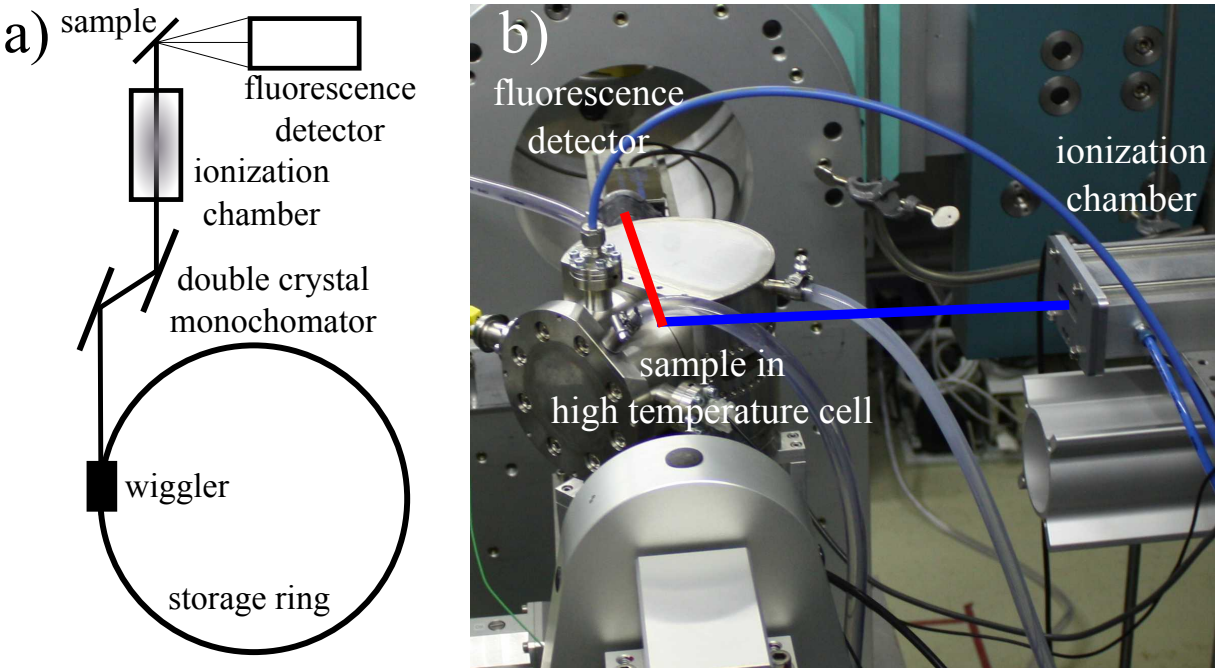

Figure 3.1: a) Schematic drawing of the DELTA beamline BL8 with the most important components and b) photograph of the experimental end-station with a high temperature *in situ* sample cell mounted on the sample stage. Incoming beam and the fluorescence radiation are indicated by a blue and red line, respectively.

be monitored. To suppress undesired elastic and Compton scattering, the fluorescence detectors are ideally placed at an angle of 90° to the incident beam in the horizontal plane.

In the experiments carried out at the DELTA beamline BL8, the Ge K-edge of bulk amorphous GeO, GeO/SiO_2 multilayers, and $GeSiO/SiO_2$ multilayers were measured by scanning the incident energy between 10.988 and 11.148 eV and detecting the fluorescence yield using both the energy dispersive SDD detectors and the PIPS detector. The SDD detectors were calibrated to measure the intensity of the Ge K_{α_1} fluorescence line. Experiments were carried out *in* and *ex situ*. The *in situ* experiments were conducted using a custom built high temperature sample cell[7] (see Fig. 3.1 b)). Prior to the experiments the sample cell was evacuated and flushed with inert gas at a steady flow rate during the *in situ* annealing processes. Samples annealed *ex situ* were measured in the same geometry using an appropriate sample holder. Several XANES scans of each sample at each temperature were measured, checked for consistency, and summed up. For comparison all resulting spectra were normalized to their integral intensity in the same energy range.

[7] The sample cell was designed and constructed by the author, details can be found in Sahle, Ch.J. (2008). "Disproportionierung und Kristallisation von massivem amorphen Germaniummonoxid." MA thesis. TU Dortmund, unpublished

3.2 ESRF beamline ID16

The ESRF beamline ID16 is a dedicated beamline for IXS experiments.[8] A schematic drawing of the general outline of the beamline as well as a photograph of the sample stage and analyzer chamber are depicted in Figs. 3.2 a) and b), respectively. The x-rays are generated by a row of three consecutive U35 undulators and are monochromatized by a Si(111) double crystal monochromator. To further decrease the bandwidth of the incoming x-ray beam a channel-cut monochromator (Si(220) or Si(440) reflection) can be used as a post-monochromator. Succeeding the monochromators a toroidal mirror can be introduced into the beam to focus the incoming x-rays to a spot size of 50×130 μm^2 (V $\times$ H) on the sample. This is convenient for inhomogeneous samples or very small sized samples, e.g. if contained within a diamond anvil cell (DAC).

Since there are no x-ray detectors with sufficiently high energy resolution in the energy regime where IXS experiments are usually conducted[9], the energy analysis is achieved using a crystal-analyzer spectrometer in a Rowland circle geometry[10] (compare Fig. 3.2 a)). In a Rowland circle spectrometer, the sample, analyzer, and detector are arranged on a common circle. At this beamline, the 1 m Rowland circle lies within the horizontal plane and the momentum transfer is determined by the angle between the incoming beam and the position of the analyzer on the circle. In all experiments carried out at ID16, nine spherically bent Si(660) crystals were used as analyzers. The arrangement of the nine analyzer crystals is shown schematically in Fig. 3.2 d). If the momentum transfer dependence of the scattering signal is weak, the signal from several analyzers can be summed up to increase the counting statistics. In case of a strong momentum transfer dependence, multiple momentum transfers can be recorded simultaneously. Depending on the choice of the optical components an overall energy resolution between approx. 0.5 eV and several eV can be achieved.

In order to detect the energy analyzed photons a two dimensional Maxipix detector is used. Several advantages over commonly used point detector setups are apparent. Firstly, the nine foci of the analyzers can be mapped to different areas on the detector allowing to process the signal from each analyzer separately. An image from the 256×256 pixel array is depicted in Fig. 3.3 a). It shows the difference between images taken above and below the Be K-edge of a Ba_8Si_{46} sample contained in a Be gasket within a DAC. This demonstrates the second benefit of an area detector: the capability of recording the imaging properties of the analyzers, i.e. different regions along the beam-path through the sample appear at different positions on the detector area. This is illustrated in Fig. 3.2 c). In the example of Fig. 3.3 a) regions of high Be concentration along the beam-path through the sample are visible as regions of high intensity on the area detector whereas regions of little or no Be along the beam-path correspond to regions of lesser intensity on the detector. Here, regions of high Be concentration correspond to the Be gasket used in a DAC whereas the lesser intense regions between the Be gasket correspond to the sample contained within the gasket. The region of pixels on the detector that solely record scattering from the sample is referred to as the region of interest (ROI). Thus, only

[8] Verbeni, R. et al. (2009). *J. Synchrotron Rad.* **16**, 469–476.

[9] Typically, primary x-ray energies lie between $6 - 15$ keV.

[10] For more information on the Rowland circle geometry the reader is referred to Johann, H.H. (1931). *Zeitschrift für Physik* **69**, 185 and citing articles.

taking into account pixels from a ROI, the signal from the sample can be conveniently discriminated against that from the sample's environment, i.e. DACs, glass capillaries, etc.

Moreover, tomographic image of the sample can be produced by scanning the sample position through the incoming x-ray beam and stacking or averaging the recorded two dimensional images along the corresponding direction. The contrast for these images can be selected by choosing the energy of the incoming beam and/or the energy loss, thus enabling a wide spectrum of electronic excitations like elastic scattering, core-electron excitations, or even plasmon- or phonon excitations as origin of contrast. Two examples for such tomographic images using elastic scattering are shown in Fig. 3.3 b) and c). This technique was used to align the samples during the high pressure experiments. More intriguing examples of how to utilize these imaging properties can be found in Huotari, S. et al. (2011). *Nat. Mater.* **10**, 489–493.

All experiments were carried out in the so called inverse geometry. In the inverse geometry the energy of the incident x-ray beam is scanned while the analyzer energy is kept fixed at the energy of the corresponding analyzer reflection. The measured energy loss thus corresponds to the difference between the incoming and analyzer energy.

In a first experiment, the multiplet features in the vicinity of the Ba $N_{4,5}$-edge of Ba_8Si_{46} were measured for pressures between 1.5 and 19.4 GPa. Using the Si(111) monochromator, the focusing mirror, and the (660) reflection of nine spherically bent Si(110) analyzers an energy resolution of 1.4 eV and an x-ray spot-size of 50×100 µm (V×H) was achieved. High pressure conditions were reached using a diamond anvil cell (DAC). The sample was placed inside a 100 µm hole in a circular Be gasket of 120 µm thickness. A small ruby chip was placed into the sample volume for pressure calibration.[11] Due to the small XRS cross section and the small sample size compared to the large parasitically scattering, sample containing Be gasket, counting times for a single XRS near edge spectrum amounted to approx. 8 h.

In a second experiment, the oxygen K-edge of water was investigated under high temperature and high pressure conditions. Using the Si(111) pre-monochromator and the Si(220) channel cut monochromator together with the focusing mirror and the (660) reflection of nine spherically bent Si(110) analyzers, an overall energy resolution of 0.8 eV could be achieved. Pressures up to 500 MPa and temperatures up to 600 °C were reached using a hydrothermal diamond anvil cell (HDAC). The HDAC was heated resistively and the purified water sample was placed into a ⌀ 0.5 mm recess hole in the culet of one diamond reducing the total path of the x-ray beam through the diamond. Temperatures were measured using a type K thermocouple, pressures were estimated from the sample volume, the homogenization temperature[12], and an equation of state after Wagner and Pruß[13].

In a third experiment, the Si $L_{2,3}$-edge of different Si containing minerals and glasses was measured *ex situ* and a hydrous NS3 melt was investigated *in situ* under high temperature and high pressure conditions by use of a HDAC. The *ex situ* samples were measured with an overall energy resolution of 2.0 eV using the Si(111) pre- and Si(220) channel cut monochromator and the (880) reflection of the nine spherically bent Si(110) analyzer

[11] Chervin, J.C. et al. (2001). *High Pressure Res.* **21**, 305–314.

[12] See supplementary information in section 7.

[13] Wagner, W. and Pruß, A. (1999). *J. Phys. Chem. Ref. Data* **31**, 387.

crystals. The *in situ* experiment was carried out with an energy resolution of 2.4 eV in the same setup but without the channel cut monochromator for reasons of an increased incident photon flux.

3.3 APS beamline 20-ID-B

The undulator beamline 20-ID-B of sector 20 of the APS has a dedicated end-station for inelastic x-ray scattering referred to as the LERIX[14] spectrometer.[15] The general outline of the beamline and a photograph of the LERIX spectrometer is shown in Fig. 3.4. X-rays from a 2.4 m undulator are monochromatized by a Si(111) double crystal monochromator. A toroidal mirror can focus the incoming beam to a spot size of 0.3×0.5 mm and the incident photon flux is measured by a He filled ionization chamber.

As is the case at beamline ID16 of the ESRF, the LERIX spectrometer is operated in inverse geometry and the energy analysis is accomplished using crystal analyzers on a 1 m Rowland circle. Here, 16 diced and 3 bent Si(111) analyzers are arranged in a semicircle each of which focuses the scattered radiation onto a sodium iodide (NaI) scintillation detector placed in a semicircle below the sample. The analyzers are mounted in angular steps of 9° such that scattering angles between $9 - 171°$ are covered. Since the Rowland circle lies in the vertical plane and thus perpendicular to the polarization direction of the incoming x-ray beam, also scattering angles close or equal to 90° can be realized. Thus, the LERIX setup allows measuring a large range of momentum transfers simultaneously. The overall energy resolution is 0.8 eV for the diced and 1.1 eV for the bent analyzers when using the Si(444) analyzer reflection. Powdered samples of Ba_8Si_{46} and $Ba_{24}Si_{100}$ were spread out on a sample holder which was tilted by 8° from the horizontal plane. Similar to the procedure described earlier, several near edge spectra were collected in the range between $80 - 250$ eV energy loss, checked for consistency and summed up.

3.4 DELTA beamline BL9

In and *ex situ* XRD experiments were carried out at the DELTA beamline BL9.[16] For the *in situ* XRD experiments, the same high temperature sample cell as mentioned in section 3.1 was used. In order to maximize the covered q range, an incident energy of 27 keV was used in all experiments. The incoming x-ray beam is monochromatized by a Si(311) double crystal monochromator and collimated to a spot size of 0.5×1 mm^2 (V $\times$ H) on the sample using a slit system. The samples were tilted by several degrees from the horizontal plane and the scattered radiation was detected by a MAR345 image plate detector covering a q-range of $q = 1.4$ - 3.7Å^{-1}.[17] Using the Fit2D program package, the two dimensional images were averaged azimuthally.[18]

[14] Lower energy resolution inelastic x-ray scattering
[15] Fister, T.T. et al. (2006). *Rev. Sci. Instrum.* **77**, 063901.
[16] Krywka, C. et al. (2005). *J. Synchrotron Rad.* **13**, 8–13.
[17] Krywka, C. et al. (2007). *J. Synchrotron Rad.* **14**, 244–251.
[18] Hammersley, A.P. et al. (1996). *High Pressure Res.* **14**, 235–248.

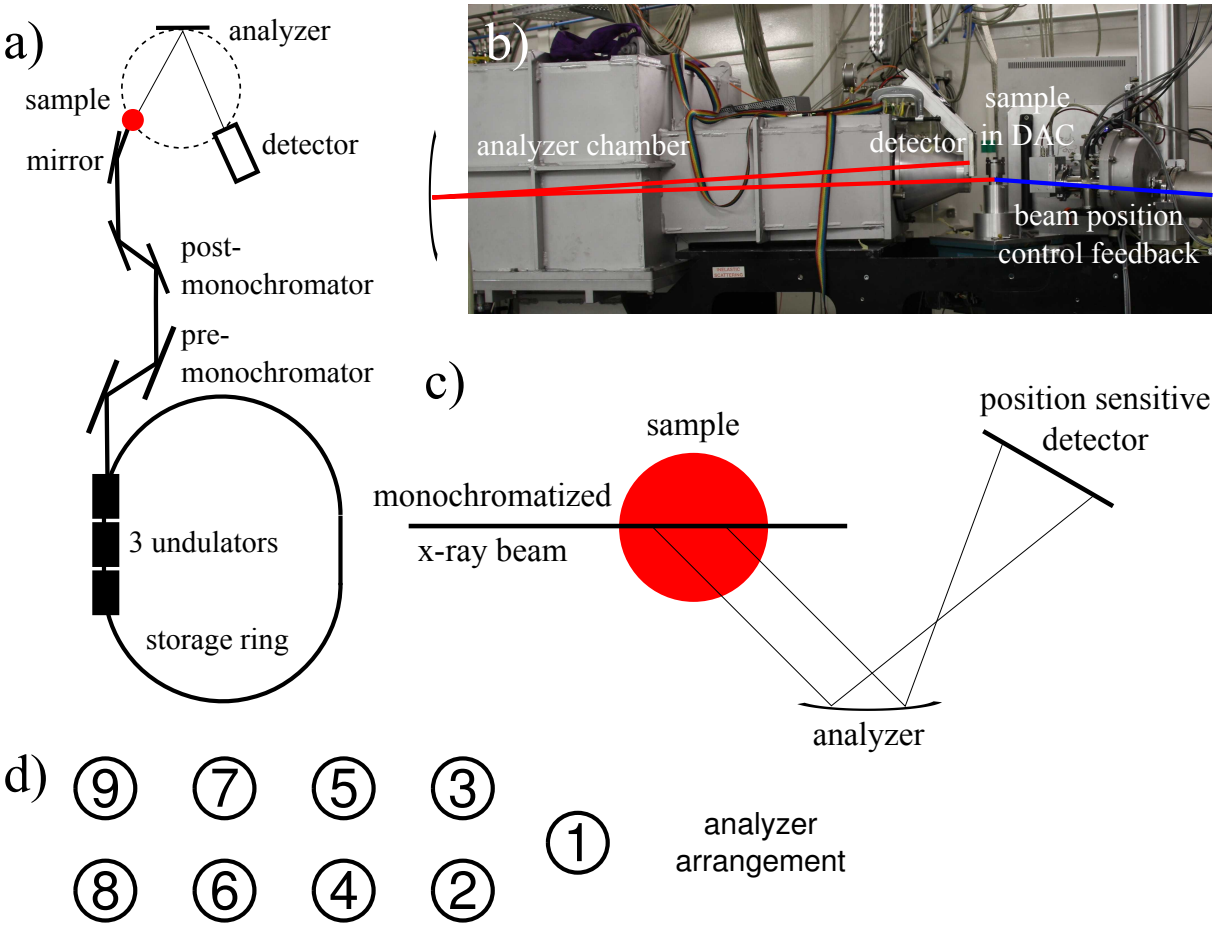

Figure 3.2: a) Schematic and oversimplified drawing of the inelastic scattering beamline ID16 of the ESRF. b) Photograph of the spectrometer in Rowland geometry including the beam position control feedback at the end of the flightpath, a DAC, and the analyzer chamber hosting 9 spherically bent analyzers and a position sensitive 2D detector. c) Scheme of the imaging properties of the Rowland spectrometer to suppress parasitic scattering from the surrounding of the sample. X-rays scattered at different positions along the penetrating path through the sample are detected at different positions on the 2D detector. d) Arrangement of the nine analyzer crystals.

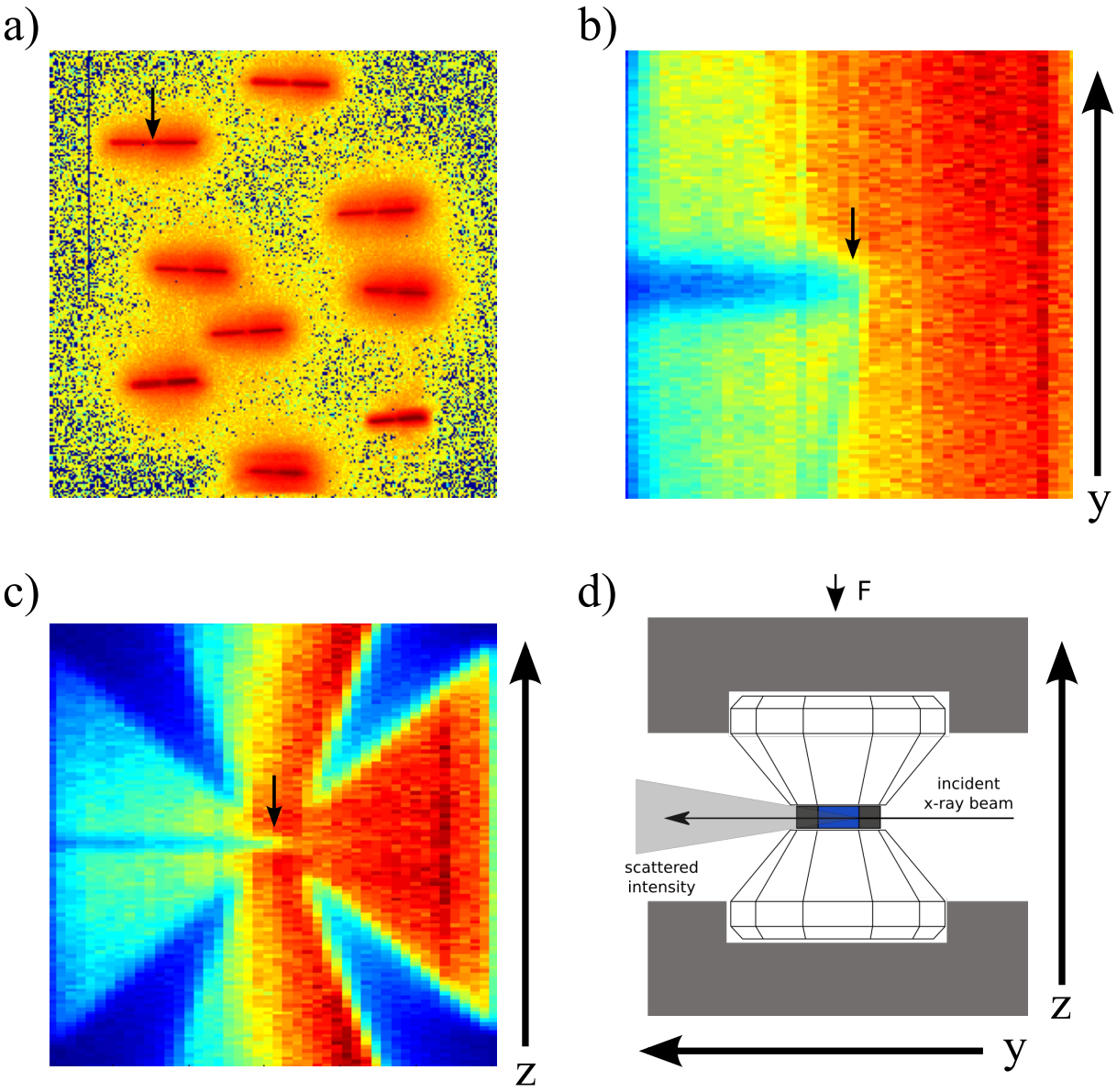

Figure 3.3: a) Difference between two 2D images taken above and below the Be K-edge of Ba_8Si_{46} within a Be gasket in a DAC. The sample position is indicated by an arrow for the first of the nine foci. As in the entire figure, red regions correspond to a high count rate, blue regions to low count rates. b) Tomographic image of a sample position scan along the y axis of the spectrometer. The sample is positioned in the middle of a circular Be gasket (small arrow in the image). The parts of the gasket shadowed by the sample (darker areas to the left and bottom) are visible. c) Tomographic image of a sample position scan along the z axis, the conically shaped diamond anvils (top and bottom) and the rotationally symmetric Be gasket (left and right) are clearly visible. The sample position is in the center of the image between the two diamond anvils (small arrow). d) Schematic drawing of a diamond anvil cell (DAC) for the geometries visible in b) and c). The scan directions are indicated by arrows.

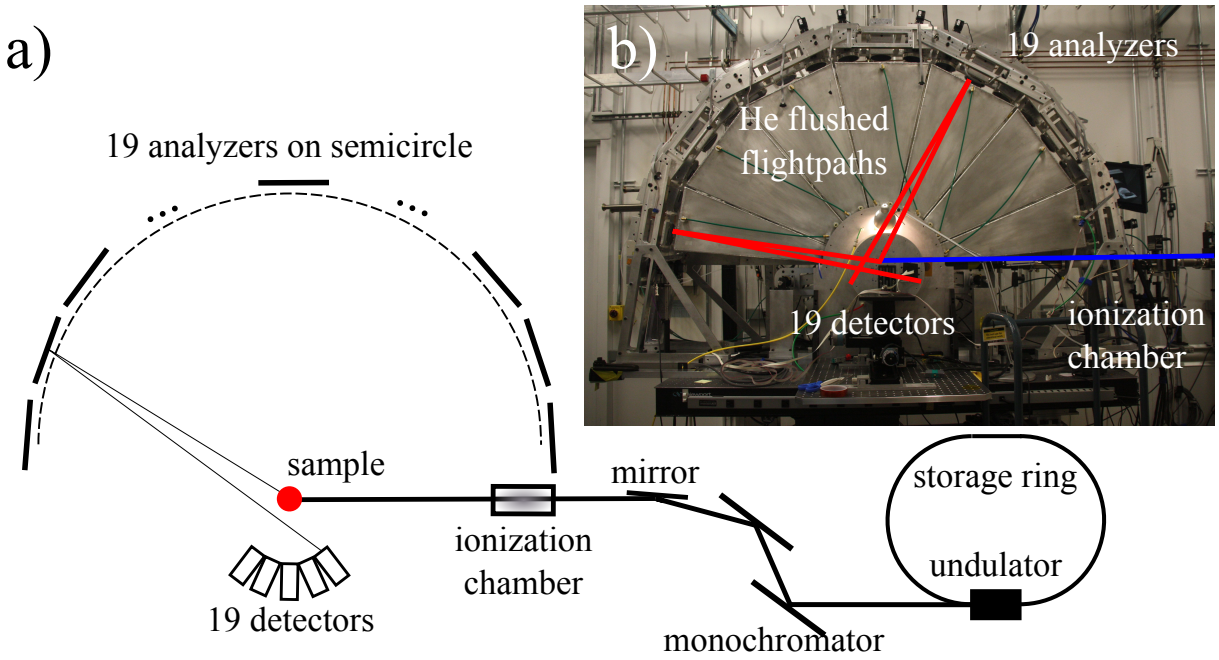

Figure 3.4: a) Schematic drawing of the outline of beamline 20-ID-B of Sector 20 of the APS. The arrangement of 19 analyzers in a semicircle allows for the detection of 19 different momentum transfers simultaneously. b) Photograph of the LERIX spectrometer showing the 19 analyzer array. Selected scattering paths are highlighted.

4 Ge nanocrystal formation in oxide matrices

The study of nanoscaled group IV semiconductor materials has attracted much attention in recent years[1]. The discovery of visible photoluminescence from nanostructured silicon in the early 1990s motivated the investigation of such systems regarding their nanotechnological applications.[2] Oxide matrix embedded Ge or Si nanocrystals (NCs) belong to this class of materials and represent promising candidates for the development of (opto-) electronic appliances.[3] In this respect, structures containing Si or Ge NCs exhibit photoluminescence in the visible and near infrared region of the electromagnetic spectrum and may thus represent alternatives to fragile porous silicon for the development of photoluminescent devices.[4] Small and fast non-volatile flash memories may be realized because of the excellent charge retention properties of oxide matrix embedded NCs.[5] Due to the possibility of band gap tuning by the control of the NCs' size, third generation photo voltaic cells, characterized by a quantum efficiency $> 30\%$, may be realizable.[6] Moreover, freestanding Ge and Si NCs have been proven as valuable non-toxic alternatives to the often used toxic direct band gap semi-conducting NCs as *in vivo* biological markers and diagnostic agents.[7] Mamiya *et al.*[8] and Kapaklis *et al.*[9] have introduced the phase separation of bulk amorphous SiO_x ($x \approx 1$) as a means to produce Si NCs in a Si-oxide matrix. The chemical similarity of Si and Ge suggests this is also possible for GeO_x ($x \approx 1$).

One pathway for the production of Ge or Si NCs embedded in an oxide matrix is the temperature induced phase separation of bulk Ge- or Si-rich oxides.[10] The disproportionation of the Ge- or Si rich oxides into domains of the pure element and pure oxide results in the formation of NCs if a sufficient domain size is reached. This method, though, usually yields nanocrystals with a broad size distribution. The results are described in detail in section 4.1 and have been published as: Ch.J. Sahle, C. Sternemann, H. Conrad, A. Herdt, O.M. Feroughi, M. Tolan, A. Hohl, R. Wagner, D. Lützenkirchen-Hecht, R. Frahm, A. Sakko, and Keijo Hämäläinen (2009). Phase separation and nanocrystal formation in

---

1 Iyer, S.S. and Xie, Y.H. (1993). *Science* **260**, 40; Lu, Z.H. et al. (1995). **378**, 258–260; Heitmann, J. et al. (2005). *Adv. Mater.* **17**, 795–803.

2 Pavesi, L. et al. (2000). *Nature* **408**, 440–444.

3 Hirschman, K.D. et al. (1996). *Nature* **384**, 338–341.

4 Maeda, Y. et al. (1991). *Appl. Phys. Lett.* **59**, 3168–3170; Kovalev, D. et al. (1999). *Phys. Status Solidi B* **215**, 871–932; Pavesi, L. et al. (2000). *Nature* **408**, 440–444.

5 Batra, Y. et al. (2007). *Solid State Commun.* **143**, 213–216.

6 Conibeer, G. (2007). *Mater. Today* **10**, 42–50; Röelver, R. et al. (2008). *Appl. Phys. Lett.* **92**, 212108.

7 Bruchez, M. et al. (1998). *Science* **281**, 2013; Lambert, T.N. et al. (2007). *Small* **3**, 691–699.

8 Mamiya, M. et al. (2001). *J. Cryst. Growth* **229**, 457–461; Mamiya, M. et al. (2002). *J. Cryst. Growth* **237**, 1909–1914.

9 Kapaklis, V. et al. (2005). *Appl. Phys. Lett.* **87**, 123114.

10 Sahle, Ch.J. et al. (2009). *Appl. Phys. Lett.* **95**, 021910–021910; Kapaklis, V. et al. (2005). *Appl. Phys. Lett.* **87**, 123114; Feroughi, O.M. et al. (2010). *Appl. Phys. Lett.* **96**, 081912.

GeO. *Appl. Phys. Lett.* **95**, 021910.

Oftentimes, as e.g. in the case of third generation photo voltaic cells, mono-dispersed NCs, or NCs with a defined size distribution and arrangement, i.e. density, are desirable. This size control would allow real band gap engineering.[11] Size controlled growth of Si NCs of high density in a silicon oxide matrix has been accomplished by thermal annealing of SiO/SiO_2 multilayers[12] and was realized for Ge NCs by annealing of GeO_x/SiO_2 multilayers with $0 < x < 2$[13]. This multilayer approach is also included in the scope of this work in order to achieve size controlled growth of Ge NCs in an oxide matrix.

Another important aspect on the way towards handy appliances is the reduction of production costs which are linked directly to the high heat load necessary for the formation of crystallites and the compatibility and cost of usable substrates.[14] Thus, efforts have been made to lower the crystallization temperature in order to reduce the heat load and make cheap quartz glass substrates feasible. Here, the use of a hydrogen containing annealing atmosphere holds promising. The results of the influence of hydrogen on the phase separation and size controlled NC formation are described in detail in section 4.2. This study was performed within a collaboration of the group of Prof. M. Tolan and the Helmholtz-Zentrum Dresden-Rossendorf. The results were published as: Ch.J. Sahle, M. Zschintzsch, C. Sternemann, J. von Borany, A. Mücklich, A. Nyrow, N.M. Jeutter, R. Wagner, R. Frahm, and M. Tolan (2011). Influence of hydrogen on thermally induced phase separation in GeO/SiO_2 multilayers. *Nanotechnology* **22**, 125709.

For efficient photo-voltaic cells and efficient light emittance from nanocrystalline photoluminescent devices, NC surface-matrix interface defect states are cumbersome. The interface between Ge and GeO_2 is known to exhibit an increased defect state density, especially when the matrix oxide is not stoichiometric ($x < 2$). To circumvent this difficulty, a new matrix material, namely SiO_2, is introduced as an alternative over a Ge-oxide matrix. The efforts to grow Ge-oxide free Ge NCs in a silica matrix is described in section 4.3. This study was performed within a collaboration of the group of Prof. M. Tolan and the Helmholtz-Zentrum Dresden-Rossendorf. The results were published as: M. Zschintzsch, Ch.J. Sahle, J. von Borany, C. Sternemann, A. Mücklich, A. Nyrow, A. Schwamberger, and M. Tolan (2011). Ge-Si-O phase separation and Ge nanocrystals growth in $Ge:SiO_x/SiO_2$ multilayers - A new dc magnetron approach. *Nanotechnology* **22**, 485303.

Since the phase separation manifests itself in structural changes in the local environment of the Ge atoms, a bulk sensitive method which probes element specifically the local structure is needed. As was pointed out in chapter 2 the study of absorption edges has proven a valuable tool in this respect. In case of absorption edges in the hard x-ray regime, x-ray absorption near edge structure (XANES) spectroscopy is the method of choice to attain the information sought. XANES measurements were employed to study the Ge K-edge in bulk native and annealed a-GeO_x ($x \approx 1$), GeO_x/SiO_2 multilayers, and $GeSiO_2/SiO_2$ multilayers.

This chapter concludes with a short summary and outlook.

---

11 Alivisatos, A.P. (1996). *J. Phys. Chem.* **100**, 13226–13239.
12 Zacharias, M. et al. (2002). *Appl. Phys. Lett.* **80**, 661.
13 Zschintzsch, M. et al. (2010). *J. Appl. Phys.* **107**, 034306.
14 Zhang, B. et al. (2010). *Appl. Phys. Lett.* **96**, 261901.

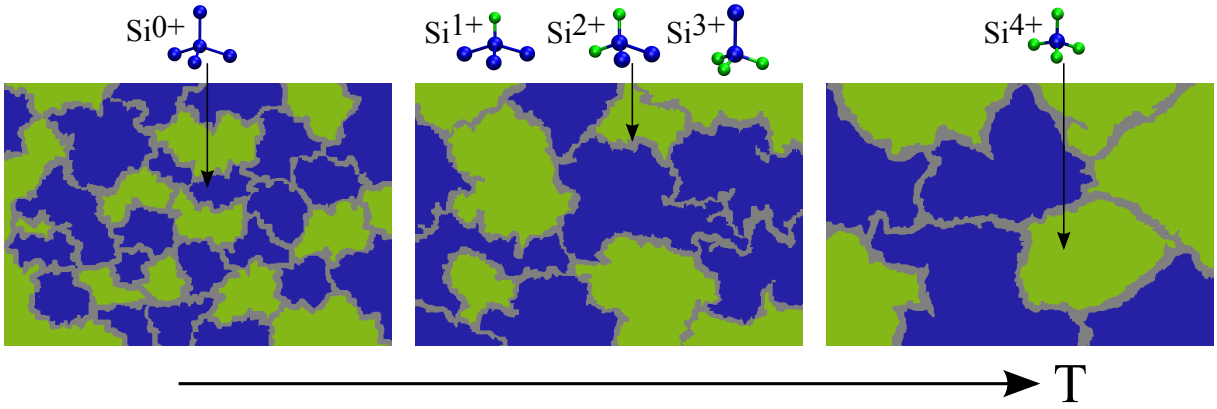

Figure 4.1: Schematic drawing of the ICM model for bulk a-SiO showing the Si and SiO_2 domains separated by Si sub-oxides ($Si(Si_{4-n}O_n)$ $(n = 1, 2, 3)$). With increasing annealing temperature, the sub-oxides disproportionate into pure Si and SiO_2 (left to right).

4.1 Phase separation and nanocrystal formation in bulk amorphous GeO_x

The phase separation process in bulk amorphous GeO (a-GeO) was investigated using XANES spectroscopy at the materials science beamline BL8[15] of DELTA, TU Dortmund (see chapter 3.1 for details). The NC formation was monitored by XRD at the multi-purpose beamline BL9[16] of DELTA.

Hohl *et al.*[17] have proposed a structural model, referred to by the authors as interface clusters mixture (ICM) model, for the native microscopic structure of bulk a-SiO. Within their model microscopic regions of elemental Si and SiO_2 are separated by sub-oxides[18] With increasing annealing temperature, these sub-oxide interfaces obliterate by a disproportionation reaction ($2SiO \rightarrow Si + SiO_2$) and thus contribute to the growth of the Si and SiO_2 domains. A schematic drawing of this model is shown in Fig. 4.1. Due to the similarity of Si and Ge, a similar behavior is expected for bulk a-GeO.

All bulk a-GeO samples were synthesized by evaporation of a 1:1 stoichiometric Ge/GeO_2 powder mixture in vacuum at 1000 °C and subsequent condensation on a molybdenum substrate which was kept at approximately 100 °C with a deposition rate of about 10 Å/s. This procedure is similar to the usual production[19] of a-SiO and yields a-GeO films of several µm thickness. After the deposition procedure, the molybdenum substrates were cut into 10×10 mm^2 pieces.

For the *ex situ* studies all samples were annealed in a nitrogen flushed or evacuated[20]

[15] Lützenkirchen-Hecht, D. et al. (2009). *J. Synchrotron Rad.* **16**, 264–272.
[16] Krywka, C. et al. (2007). *J. Synchrotron Rad.* **14**, 244–251.
[17] Hohl, A. et al. (2003). *J. Non-Cryst. Solids* **320**, 255–280.
[18] Tetrahedral Si clusters having one to three oxygen neighbors ($Si(Si_{4-n}O_n)$ $(n = 1, 2, 3)$).
[18] All bulk a-GeO samples were prepared at the TU Darmstadt by A. Hohl.
[19] Hohl, A. et al. (2003). *J. Non-Cryst. Solids* **320**, 255–280.
[20] Data taken from Schacht, A. et al. (2009). *J. Non-Cryst. Solids* **355**, 1285–1287.

quartz glass tube for 30 minutes. All *in situ* experiments were carried out using a custom built sample cell.[21] The stoichiometry of all samples was determined by energy dispersive x-ray spectroscopy (EDX) subsequent to the experiments and yields a Ge:O ratio of $x \approx 1$ for all samples.[22]

Nanocrystal formation in bulk a-GeO

The bulk a-GeO samples were characterized prior to the annealing procedure by XRD and showed an amorphous structure. The background subtracted XRD patterns for a native and selected annealed samples from the sample series annealed *ex situ* are depicted in Fig. 4.2 a) and b).[23] For annealing temperatures above $T = 243$ °C, small structural changes take place as evidenced by the formation of pronounced structure factor maxima. An additional shift of these maxima towards smaller scattering angles is indicated by the filled circles. The sample annealed at 509 °C shows first signatures of Ge crystallization. The three observed reflections are indicated by arrows in the figure and correspond to a mean crystal size of $d = (1.3 \pm 0.8)$ nm as estimated using the Scherrer equation.[24][25] The broad maximum in the structure factor at $q = 3.4$ Å^{-1} observed for samples annealed at temperatures between $T = 341$ °C and $T = 471$ °C is completely split into the Ge(220) and Ge(311) peaks at an annealing temperature of $T = 538$ °C as an unambiguous sign of crystallization.[26] The mean size of the Ge crystals is $d = (5.7 \pm 1.0)$ nm. The sample annealed at $T = 632$ °C shows also crystallization of GeO_2. Here, the mean crystal size is (7.6 ± 0.8) nm for the Ge crystallites and (11.4 ± 0.8) nm for the GeO_2 crystallites. A higher crystallization temperature of a-GeO_2 compared to a-Ge was reported earlier[27] and is advantageous when the formation of Ge crystallites in an amorphous oxide matrix is desired.[28]

In order to assign the maxima of the structure factor to atomic bonds in the sample, structure factors of atomic Ge and GeO_2 clusters were modeled using the Debye equation

$$I(q) = \sum_{i=1}^{N} \sum_{j=1}^{N} f_i(q) f_j(q) \frac{\sin(q r_{ij})}{q r_{ij}}. \tag{4.1}$$

Here, f_i and f_j are the atomic scattering factors, N is the number of atoms in the cluster, and r_{ij} is the distance between atoms of type i and j. The results are shown in Fig.

---

21 Sahle, Ch.J. (2008). "Disproportionierung und Kristallisation von massivem amorphen Germaniummonoxid." MA thesis. TU Dortmund, unpublished.

22 The EDX measurements were carried out by A. Hohl at TU Darmstadt, Darmstadt, Germany.

23 The *ex situ* studies were performed whilst the duration of the author's diploma thesis and were published in (Sahle, Ch.J. et al. [2009]. *Appl. Phys. Lett.* **95**, 021910–021910). All other measurements were performed during the author's PhD work.

24 Scherrer derived the following equation in order to estimate approximate crystal sizes: $d = K\lambda/\Delta_{2\Theta}\cos(2\Theta/2)$, where $K \approx 1$ is a constant shape factor (Patterson, A.L. (1939). *Phys. Rev.* **56**, 978), λ is the x-ray wavelength, $\Delta_{2\Theta}$ is the line broadening at half the maximum intensity, and Θ is the Bragg angle.

25 Langford, J.I. and Wilson, A.J.C. (1978). *J. Appl. Crystall.* **11**, 102–113.

26 Zacharias, M. et al. (1996). *Thin Solid Films* **278**, 32–36.

27 Yamaguchi, O. et al. (1982). *J. Chem. Soc., Dalton Trans.* (10 1982), 1907–1910.

28 Zacharias, M. and Streitenberger, P. (2000). *Phys. Rev. B* **62**, 8391–8396.

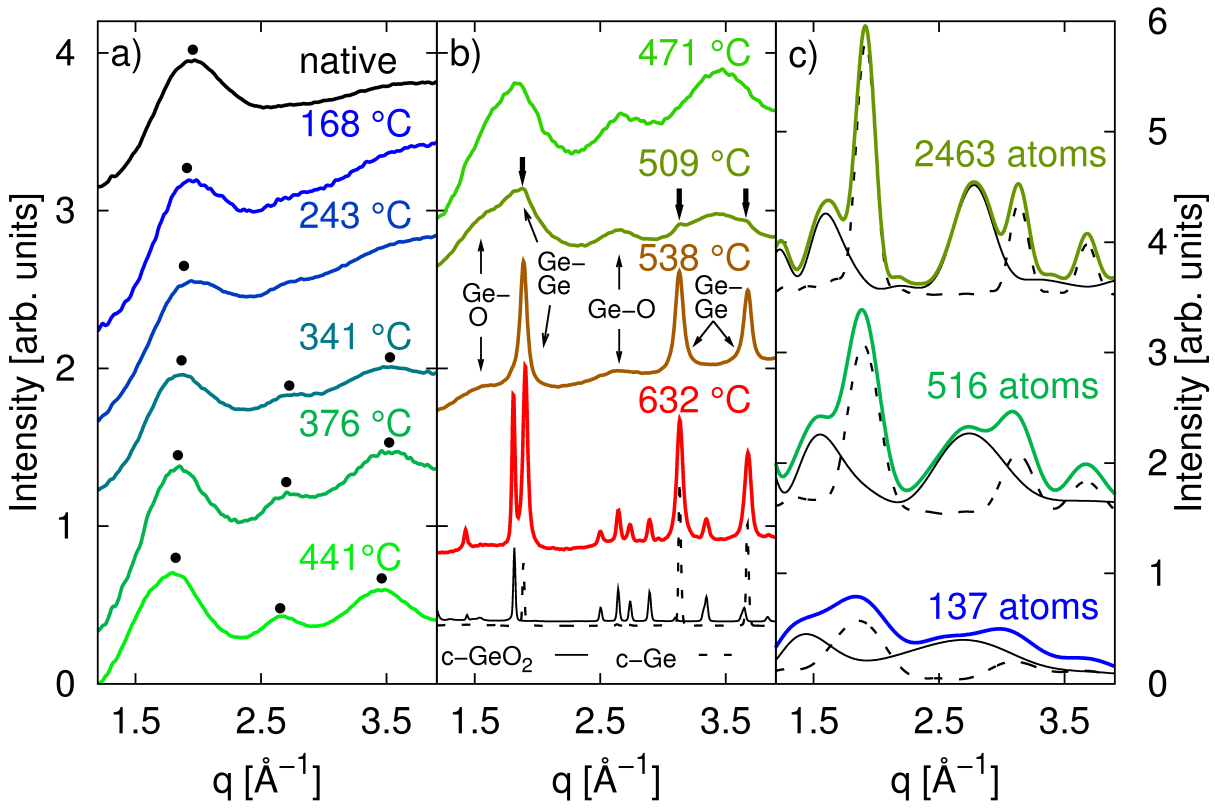

Figure 4.2: XRD patterns of a native and differently annealed a-GeO samples as recorded at DELTA beamline BL9. a) native – 441 °C; b) 471 – 632 °C as well as of polycrystalline Ge (dashed line) and GeO_2 (solid line) reference samples. Correlations resulting in peaks or maxima in the structure factor are indicated by arrows. c) Simulated structure factors of Ge (dashed lines) and GeO_2 (solid lines) clusters and their superposition (colored lines) using the Debye equation and atomic positions from crystalline atomic clusters of different sizes.

4.2 c) for different sizes of Ge (dashed line) and GeO_2 (solid line) clusters and their superposition (solid colored line). Comparison with the experimental data suggests that the maximum at $q = 3.4$ Å^{-1} is due to the Ge-Ge bonding distance, whereas the broad maximum at $q = 2.6$ Å^{-1} mainly stems from the average Ge-O bond length in GeO_2, i.e. the nearest neighbor shells. The broad maximum at $q = 1.7$ Å^{-1} can be attributed to both the second nearest Ge-Ge coordination in elemental Ge and the second shell of oxygen neighbors (Ge-O-Ge-O) in GeO_2. The correlations are indicated by arrows in the figure. Using more and more atoms for the calculation results in sharper features comparable to the temperature dependence of the experimental data. Even a splitting of the broad feature at $q = 3.5$ Å^{-1} into the Ge(220) and Ge(311) reflections can be suspected. The agreement between the largest cluster used for the simulation and the experimental data at $T = 538$ °C is remarkable. A shift in the position of the structure factor maxima cannot be simulated within this crude model since even for the small cluster sizes the crystalline structure and bond lengths were used. In addition, sub-oxides were totally neglected within this model.

In situ XRD measurements of the NC formation are shown in Fig. 4.3 a). Each group of curves corresponds to one temperature. Since the exposure time for each scan was 90 s and the readout time of the image plate detector is also 90 s the time between the beginning of two consecutive scans amounts to approx. 3 min. Changes in the spectra up to $T = 430$ °C are similar to the changes observed in the *ex situ* study and the spectral changes within one temperature group are below the time resolution. Starting at 430 °C crystallization can be observed within the first 15 min of heat exposure. The nanocrystal sizes for the Ge NCs at this temperature can be estimated to (1.6 ± 0.5) nm and grow to an average size of up to (2.9 ± 0.6) nm upon heat exposure at the highest annealing temperatures. First signs of GeO_2 crystallization can be seen at $T = 450$ °C. GeO_2 size estimation via Scherrer's equation yields (2.0 ± 0.8) nm for these crystallites. Crystalline GeO_2 regions grow up to an average size of (5.2 ± 0.3) nm after heat treatment at 530 °C. The time and temperature evolution of the Ge(111) and GeO_2(011) reflections are shown in Fig. 4.3 b) where the peak width multiplied by the peak intensity is plotted against the annealing time for the two reflections (this procedure results in a relatively smooth curve despite the temperature changes between groups of scans). Before reaching $T = 430$ °C the sample was investigated at temperatures between ambient and 410 °C for a total of 90 min. This explains the lower crystallization temperature as compared to the findings of the *ex situ* measurements. Again, the crystallization of Ge at lower temperatures than GeO_2 is evident.

XRD yields information about the NC formation in bulk a-GeO_x. A temperature window between the onset of Ge and GeO_2 crystallization allows for the production of Ge NCs embedded in an oxide matrix. Comparison of the experimental structure factors to simulated structure factors from simple crystalline Ge and GeO_2 clusters and their superposition provides a straightforward and efficient way to attribute features in the structure factor to bond lengths and coordinations in the material. *In situ* XRD confirms the temperature window for the production of Ge NCs in an amorphous oxide matrix in which GeO_2 crystallization is suppressed and provides a timescale for the formation of Ge NCs.

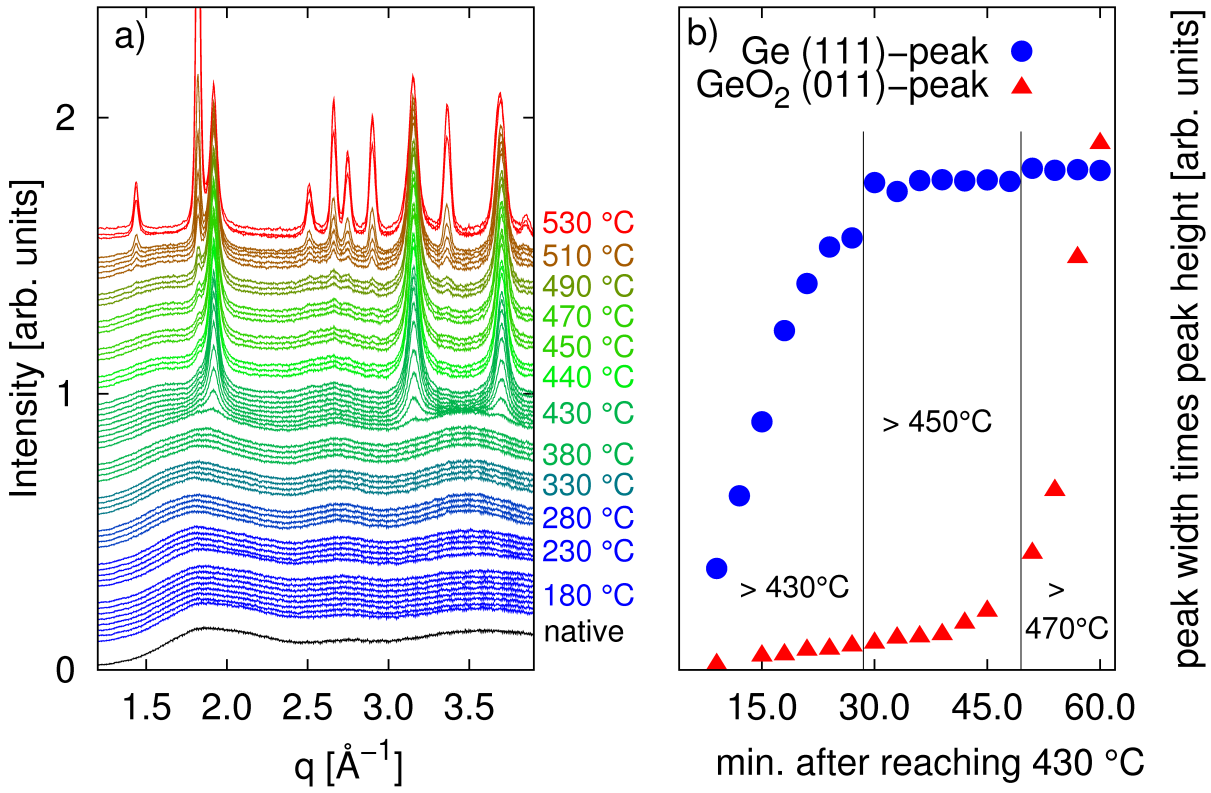

Figure 4.3: a) *In situ* XRD patterns of bulk a-GeO. Each group of scans corresponds to the temperature indicated to the right of the figure and a time sequence with 3 min between scans. b) Peak width times peak hight of the Ge(111) and GeO_2(011) reflections vs. the duration of the annealing. Before reaching $T = 430\,°C$ the sample was investigated at temperatures between ambient and 410 °C for a total of 90 min.

Phase separation in bulk a-GeO

The phase separation of bulk a-GeO, i.e. the disproportionation of GeO into Ge and GeO_2 ($2GeO \rightarrow Ge + GeO_2$), was investigated by XANES spectroscopy at the Ge K-edge to study the structural changes on the way to NC formation. The progression of the Ge K-edge of an a-GeO sample in its native state and after consecutive annealing in a nitrogen atmosphere at temperatures between $150 - 530\,^{\circ}C$ for 30 min is shown in Fig. 4.4 a), exemplarily. The statistical accuracy is in the order of the linewidth used in the figure. The spectrum of the native sample shows a strong shoulder at $E = 11106$ eV marked by a dot between the onset of the Ge K-edge in diamond Ge (11103.0 eV) and pure alpha-quartz GeO_2 (11108.4 eV) which indicates a contribution of significant amounts of sub-oxides, i.e. $Ge(Ge_{4-n}O_n)$ with $n = 1, 2, 3$. This is corroborated by calculations of the near edge absorption spectra of the central Ge atoms in $Ge(Ge_{4-n}O_n)$ ($n = 1, 2, 3$) clusters using the FDMNES program package[29]. The atomic coordinates of the clusters used for the calculation were derived from $Si(Si_{4-n}O_n)$ ($n = 1, 2, 3$) sub-oxide clusters taken from Sakko *et al.*[30]. All Si atoms in these clusters were replaced by Ge atoms and the structure was relaxed using a force field optimization routine provided by the OPENBABEL program package[31]. Since the average number of atoms within the clusters is about 35 the force field optimization routine converges within a few hundred steps. The relaxed clusters showed bond lengths within less than 10% error of the bond lengths found in crystalline Ge and GeO_2. The simulated spectra for the sub-oxides as well as small crystalline Ge and GeO_2 clusters are shown in Fig. 4.4 b). A systematic shift in the absorption edge onset with increasing oxidation state is well visible which confirms the suggestion that spectral weight in the region between the onset of the Ge K-edges in elemental Ge and GeO_2 can be attributed to sub-oxides in the samples and supports the interpretation of a decreasing shoulder in the a-GeO spectra with rising annealing temperature as a consequence of a decreasing sub-oxide content.

In order to analyze the temperature dependence of the phase separation in more detail, the parameter $A(T)$ is derived by the integrated difference D between the annealed samples and the native sample in the energy range between $E_1 = 11103.0$ eV and $E_2 = 11107.5$ eV (see Fig. 4.4). Thus, this phase separation parameter $A(T)$ is calculated as

$$A(T) = \int_{E_1}^{E_2} |I_{\text{annealed}} - I_{\text{native}}| \mathrm{d}E = \int_{E_1}^{E_2} D \mathrm{d}E. \tag{4.2}$$

The differences $D = |I_{\text{annealed}} - I_{\text{native}}|$ between the native and differently annealed samples shown in Fig. 4.4 a) are presented in part c) of the same figure. Lower and upper limits for the integration are indicated by vertical lines. The resulting $A(T)$ values for samples annealed under different conditions are depicted in Fig. 4.5. Different annealing procedures, i.e. annealing atmospheres and annealing times were chosen to investigate the influence of these on the phase separation. The annealing conditions for the different samples are summarized in table 4.1, parameters from Schacht *et al.*[32] are also listed.

[29] Joly, Y. (2001). *Phys. Rev. B* **63**, 125120.
[30] Sakko, A. et al. (2010). *Phys. Rev. B* **81**, 205317.
[31] See `www.openbabel.org` for details.
[32] Schacht, A. et al. (2009). *J. Non-Cryst. Solids* **355**, 1285–1287.

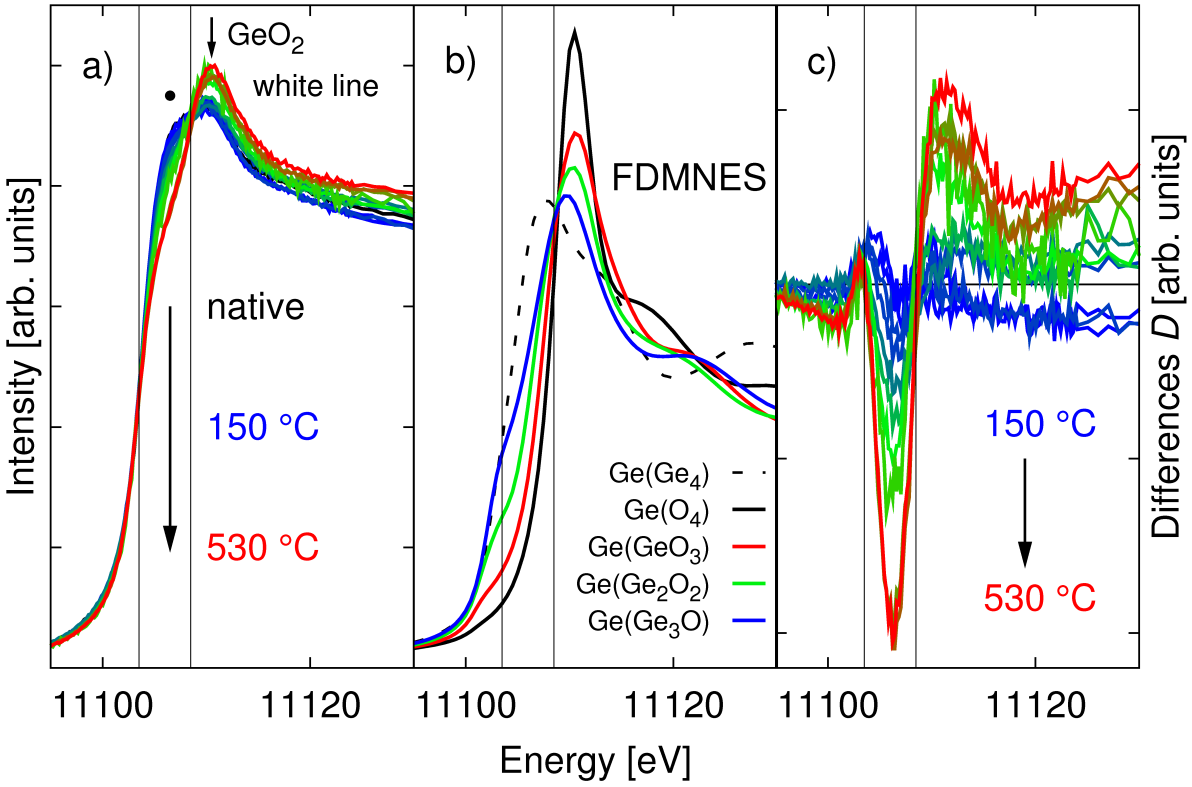

Figure 4.4: a) XANES spectra of a-GeO after systematic annealing at temperatures between $150 - 530$ °C (the colors represent temperatures as indicated in figure 4.2 a) and b)). The position of the GeO_2 white line is indicated by an arrow. b) Simulated absorption spectra using the FDMNES program package for central Ge atoms with successively increasing oxidation state (see text for details). c) Differences D between the spectrum of the native sample to spectra of the sample after the respective annealing.

		atmosphere	duration
sample series A	*ex situ*	N_2	30 min
sample B	*in situ*	N_2	30 min
sample C	*in situ*	N_2	100 min
sample D	*in situ*	N_2	60 min at 530 °C
Schacht *et al.*	*ex situ*	vacuum	30 min

Table 4.1: Summary of samples and annealing conditions used to investigate the phase separation of bulk a-GeO. Data from a temperature series of samples annealed *ex situ* and in vacuum conditions were taken from Schacht, A. et al. (2009). *J. Non-Cryst. Solids* **355**, 1285–1287.

The temperature dependence of $A(T)$ indicates a start-point of the phase separation at $T_{\text{start}} \approx (260 \pm 20)$ °C and an end-point at $T_{\text{end}} \approx (450 \pm 20)$ °C hardly depending of the annealing conditions. From the general temperature dependence and the nanocrystal formation temperature found in XRD it can be deduced that the nanocrystal formation sets in after the phase separation is almost completed. Since, as mentioned above, the crystallization temperature for Ge is lower than for GeO_2 a temperature window from at least $T = 450 - 510$ °C, where only Ge crystallites form, can be found.

The inset of figure 4.5 shows the phase separation parameter $A(T = 530\,°\text{C})$ of sample D annealed under a constant nitrogen flow as a function of annealing time. Within the errorbars, $A(T = 530\,°\text{C}, t)$ only changes in the first 20 min of heat exposure. The minimum annealing time for samples A, B, and C, as well as the sample annealed under vacuum conditions, was 30 min. Considering that both N_2 and vacuum conditions are inert, one can attribute the independence of $A(T)$ of the temperature series as caused by the long heat exposures. The time dependence found in the phase separation is in accordance with the findings of the *in situ* XRD experiments presented in Fig. 4.3. However, very long annealing times, as in the *in situ* XRD study, seem to lower the crystallization temperature.

XANES yields information about the structural changes in the bulk a-GeO samples during the phase separation. Systematic changes in the shape of the absorption spectra were found and can be associated with the phase separation of Ge sub-oxides into elemental Ge and pure GeO_2 which is in line with the ICM model. The experimental spectra can in principle be simulated using the FDMNES program package, however, more realistic atomic structure models are desirable. The time scales found in *in situ* XANES experiment agree well with the *in situ* XRD study.

4.2 Phase separation and size controlled growth of Ge nanocrystals in GeO/SiO_2 multilayers

As mentioned in the introduction to this chapter, the control of the NC size bears control of the electronic structure, i.e. band structure, of the NCs. Moreover, the origin of the photoluminescence is still subject of current debate where the ability to prepare monodispersed NCs will enable to distinguish size effects from surface effects.

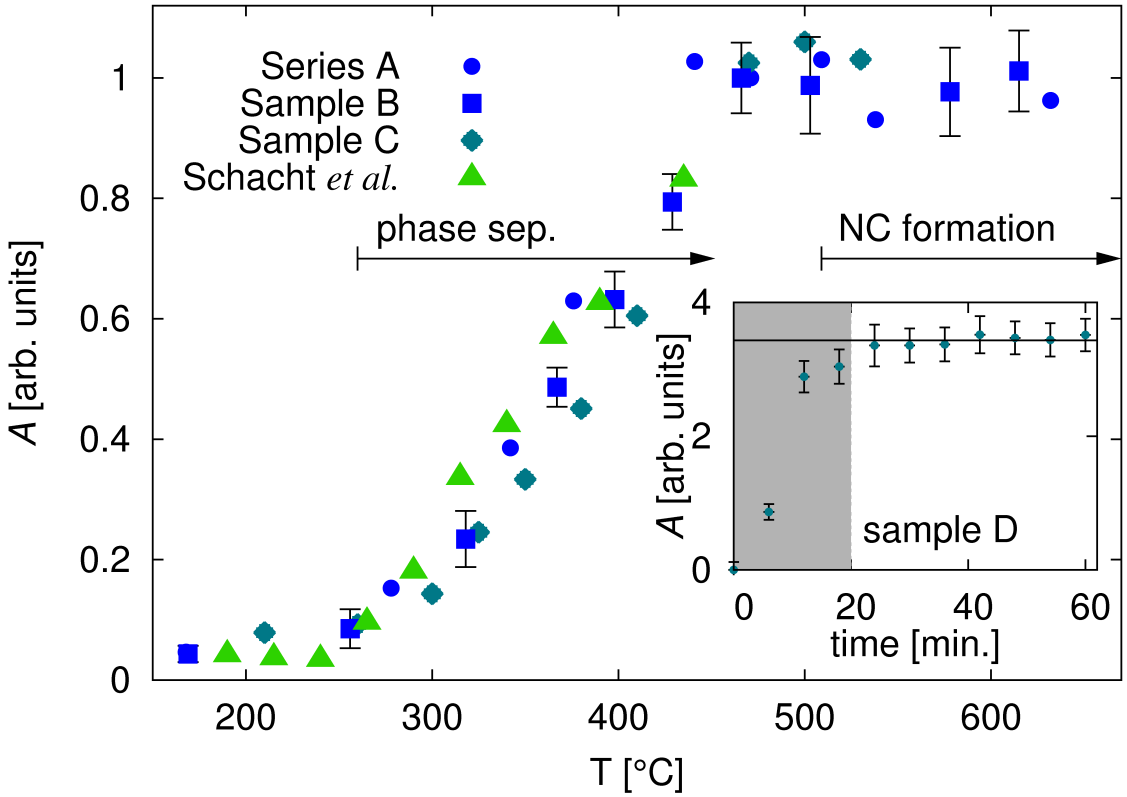

Figure 4.5: $A(T)$ values of different samples (see table 4.1) annealed *in* and *ex situ*. Data from a-GeO_x ($x \approx 1$) from Schacht, A. et al. (2009). *J. Non-Cryst. Solids* **355**, 1285–1287. The inset shows the time evolution of $A(T = 530\,°C)$ for sample D measured *in situ*.

Sample	final temperature	NC size	atmosphere
SL	500 °C	15 nm	Ar/H_2
	550 °C	15 nm	N_2
ML	500 °C	4.8 nm	Ar/H_2
	550 °C	6.5 nm	N_2

Table 4.2: Summarized NC sizes as derived from the Scherrer equation for the single layer and multilayer samples.

Following the multilayer approach of Zacharias *et al.*[33] for preparing size controlled Si NCs in an amorphous SiO_2 matrix, thin layers of GeO_x ($x \approx 1$) were separated by thin SiO_2 layers in order to confine the NCs' size in the direction perpendicular to the sample surface. Confinement in the lateral direction will be accomplished by the GeO_2 product of the phase separation within the GeO_x layers.

All multilayer samples were prepared by M. Zschintzsch as described in detail in Zschintzsch, M. et al. (2010). *J. Appl. Phys.* **107**, 034306. In short, alternate thin films of GeO_x and SiO_2 were deposited by reactive direct current (dc) magnetron sputtering employing a vacuum chamber equipped with two unbalanced 1 inch miniature magnetrons each tilted by 30° from the vertical position at a distance of 100 mm from a Si(001) substrate. Appropriate O_2/Ar gas mixture flow rates during the deposition allow for the preparation of the desired film composition. Thus, two GeO_x/SiO_2 multilayer samples (ML) with 50 periods each comprised of a 5.2 nm thick a-GeO_x and a 1.5 nm thick a-SiO_2 layer as well as two 65 nm thick a-GeO_x single layer samples (SL) were prepared. All samples were covered with a 30 nm thick a-SiO_2 cap layer to prevent evaporation of volatile GeO. The stoichiometry was checked by Rutherford backscattering (RBS) subsequent to the deposition and yields $x \approx 1$ for all samples.[34] As reference samples, 40 nm thick a-Ge and a-GeO_2 films were prepared.

The readily prepared ML and SL samples were consecutively annealed *ex situ* for 30 minutes at temperatures between $150 - 550$ °C in a reducing Ar/H_2 (7.5% H_2) and an inert N_2 atmosphere, respectively. The measurements of the Ge K absorption edge were carried out at beamline BL8 of DELTA as already described in chapter 4.1. The sample characterization was carried out using 8 keV Cu K_α radiation from a laboratory source for XRD and x-ray reflectivity (XRR) analysis and cross-sectional transmission electron microscopy (TEM) using a FEI Titan microscope (300 kV).[35]

Size controlled nanocrystal formation in GeO

XRD patterns of the native and readily annealed samples are shown in Fig. 4.6. No signs of crystallization can be found for the native samples. After the final annealing Ge NCs have formed in all samples. A rough estimate of the NCs' average size using the Scherrer

[33] Zacharias, M. et al. (2002). *Appl. Phys. Lett.* **80**, 661.

[34] The RBS measurements were carried out by M. Zschintzsch of the Helmholtz-Zentrum Dresden-Rossendorf (HZDR), Rossendorf, Germany.

[35] The sample characterization using XRD, XRR, and TEM was carried out by M. Zschintzsch and A. Mücklich at the HZDR, Rossendorf, Germany.

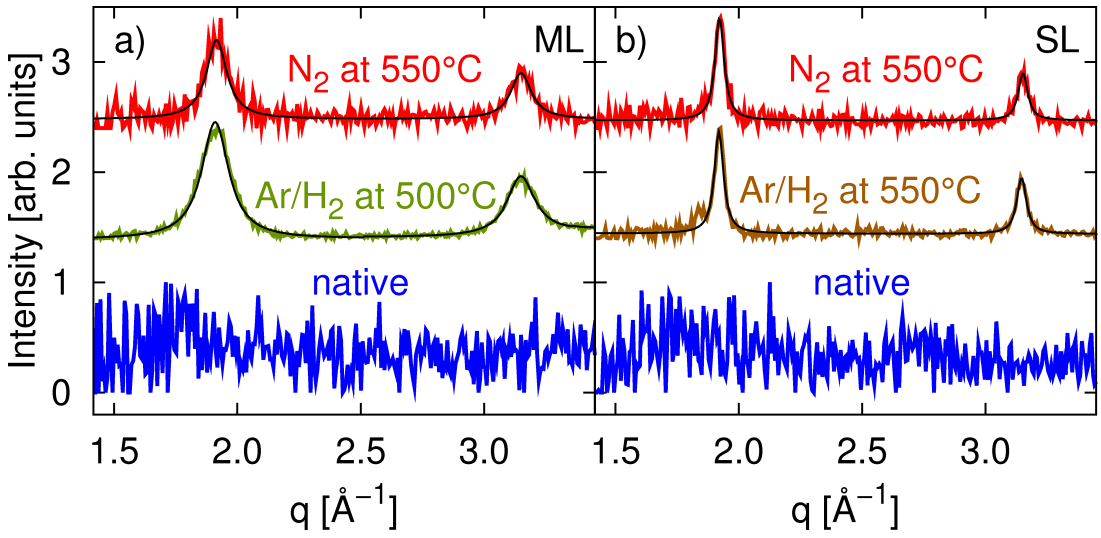

Figure 4.6: XRD patterns of a) the ML and b) SL samples in their native state and after annealing in Ar/H_2 and N_2 atmosphere, respectively. The solid black lines represent the best fits used for the estimation of the nanocrystal size via the Scherrer equation. The XRD scans were performed by M. Zschintzsch at the HZDR, Rossendorf, Germany.

equation yields the results summarized in table 4.2. Since the NC size is of the order of the GeO sublayer thickness in the ML sample and considerably bigger for equal annealing temperatures in the SL sample, the size of the NCs is effectively limited by the GeO layer thickness obtained for the native sample. From the considerably higher countrates in the XRD patterns of the ML and SL sample annealed in Ar/H_2 an increased NC density can be suspected. The XRR analysis shows that the multilayer structure is preserved after the final annealing step regardless of the annealing atmosphere, but the average layer thickness is reduced slightly when H_2 is present in the annealing atmosphere. TEM images of all readily annealed samples are shown in Fig. 4.7 and corroborate the conclusions drawn from the x-ray analysis. Here, the reduction in the GeO sublayer thickness in the ML sample annealed in Ar/H_2 compared to the ML sample annealed in N_2 can clearly be seen (Fig. 4.7 c) and d)). In addition, an increased NC density for the samples annealed in the reducing Ar/H_2 atmosphere is visible. For the ML sample this increased density can be observed throughout the multilayer stack, whereas in the SL sample an increased NC density at the surface of the sample is obvious.

Phase separation

XANES spectra of the native and annealed samples are shown in Fig. 4.8. The spectra of the samples annealed in an inert N_2 atmosphere (Fig. 4.8 a) and b)) exhibit a similar temperature dependence as the bulk amorphous GeO samples (compare section 4.1). The shoulder between the position of the edge onset in pure Ge and pure GeO_2 decreases systematically accompanied by an increase of the GeO_2 white line with increasing annealing temperature. Above $T = 400$ °C spectral changes are small and XANES curves resemble a 1:1 superposition of the spectra of the a-Ge and a-GeO_2 reference samples. This indicates

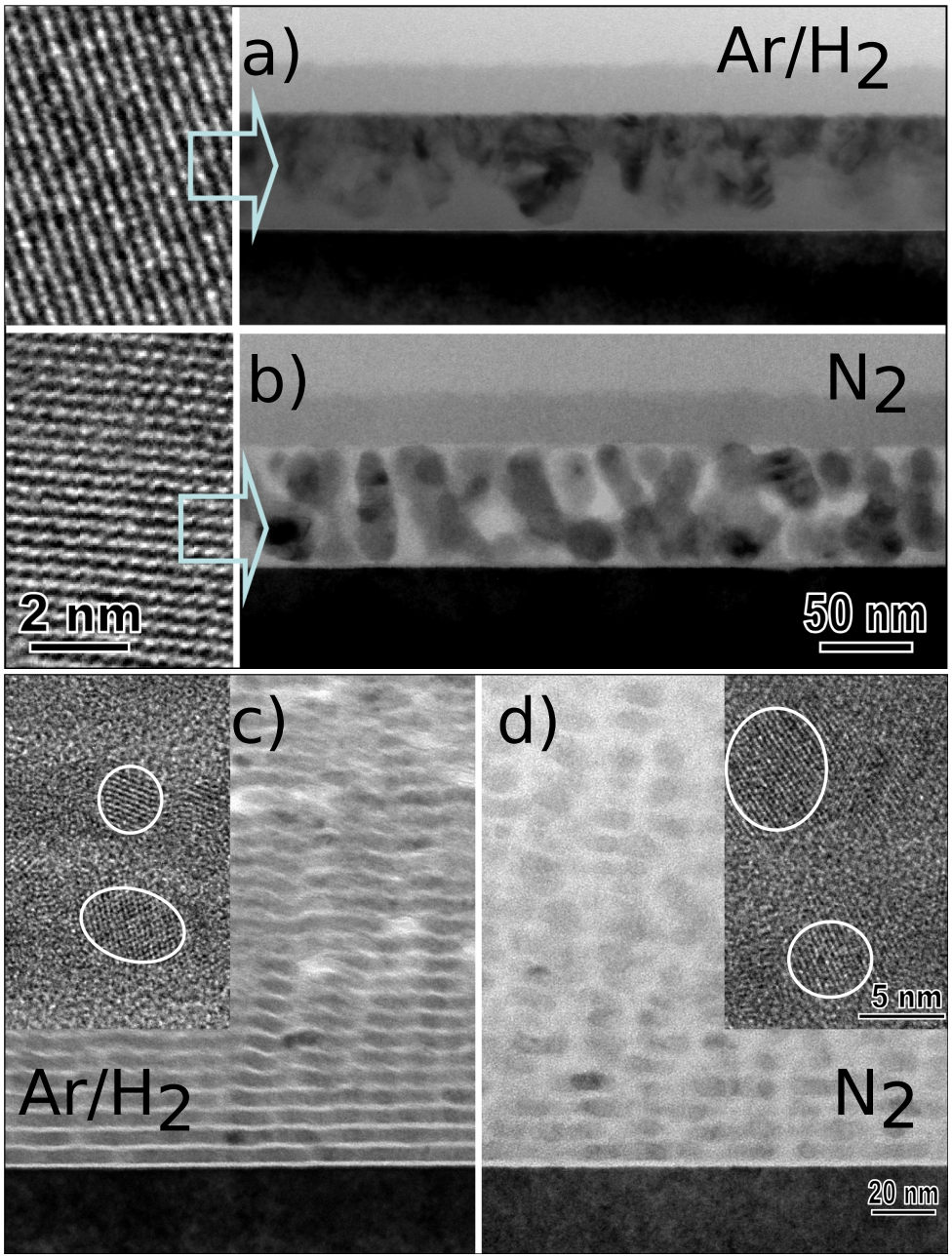

Figure 4.7: Cross-sectional TEM images of the readily annealed samples. a) SL sample annealed in Ar/H_2; an increased nanocrystal density close to the sample-cap layer interface is obvious in comparison with the SL sample annealed in N_2 b) which shows equally distributed Ge crystals. Lattice planes of single Ge NCs from the two single layer samples are shown in the high-resolution images on the left. c) Multilayer sample annealed in Ar/H_2, almost closed nanocrystalline Ge layers due to the reduction of Ge-oxides. d) Multilayer sample annealed in N_2 yielding well separated NCs. The insets of c) and d) show high-resolution TEM images which reveal the conservation of the ML structure as well as the lattice planes of single Ge NCs and their vertical size limitation due to the SiO_2 separation layers. The TEM images were taken by A. Mücklich at the HZDR, Rossendorf, Germany.

an almost complete phase separation at an annealing temperature of 400 °C as the spectra of both the ML and SL sample are dominated by contributions from equal amounts of Ge and GeO_2 domains. Likewise, the mean stoichiometry of the GeO_x sub-layers can be assumed to be $x \approx 1$ for temperatures below $T = 400$ °C and the changes in the absorption edge's shape up to this temperature can be assigned to the disproportionation of Ge sub-oxides into Ge and GeO_2. Contributions stemming from sub-oxides can be neglected for temperatures above 400 °C.

XANES spectra of the samples annealed in an Ar/H_2 atmosphere are depicted in Fig. 4.8 c) and d). For annealing temperatures up to 400 °C the temperature progression of the spectra is very similar to the samples annealed in a N_2 atmosphere. At $T \approx 400$ °C the spectra again resemble a 1:1 superposition of the XANES signals of the Ge and GeO_2 reference samples and the stoichiometry can be assumed to be $x \approx 1$ up to this temperature. When annealed at higher temperatures in a H_2 atmosphere, however, the spectra of both the ML and SL sample gain spectral weight in the region of the shoulder at $E = 11106$ eV accompanied by a reduction of the GeO_2 white line intensity. A shift in the edge onset can be observed as well. This can be assigned to the reduction of Ge-oxides due to the reducing H_2 in the annealing atmosphere. The reduction in the ML sample is almost completed at a temperature of 500 °C, inferred by the close similarity of the sample's spectrum at 500 °C with the spectrum of the Ge reference sample. In contrast, the SL sample is not fully reduced even at a temperature of 550 °C and an increased NC density close to the sample-cap layer interface is visible in the TEM image (Fig. 4.7). This is in accordance with the results of the RBS measurements which suggest a GeO_x stoichiometry close to pure Ge ($x \approx 0$) at the surface of the GeO_x layer while the stoichiometry is unchanged ($x \approx 1$) far away from the surface compared to the native sample.

For a more quantitative analysis, the phase separation parameter $A(T)$, as introduced in section 4.1, was calculated for the spectra from the ML and SL samples both annealed in N_2 and Ar/H_2. These $A(T)$ values are shown in Fig. 4.9 a) together with the envelope of the $A(T)$ values obtained for the bulk a-GeO samples (section 4.1). Whereas the temperature dependence of the samples annealed in pure N_2 is very similar to the findings for bulk a-GeO, the phase separation sets in earlier and proceeds faster in an Ar/H_2 atmosphere. Here, the phase separation is completed at least 50 °C below the value for samples annealed in a non-reducing atmosphere, i.e. at $T = 350 - 400$ °C. This points to a strong effect of H_2 on the phase separation even for temperatures where the reducing effect of H_2 can be assumed to be negligible.[36] A reducing effect was reported earlier and can clearly be deduced from the shape of the XANES spectra for temperatures higher than 400 °C in both the ML and SL samples, but a shift in $A(T)$ for temperatures below 400 °C indicates that also the growth of Ge and GeO_2 domains at the cost of sub-oxides is enhanced by the H_2 present in the annealing atmosphere. On the basis of the experimental findings, the following mechanism is suggested: instead of reducing regions of GeO_2, the H_2 in the annealing atmosphere reduces sub-oxides forming OH molecules which in turn may benefit the oxidation of other sub-oxide clusters. In an inert gas atmosphere, the phase separation is accomplished by a rearrangement of oxygen atoms following

$$2\mathrm{GeO} \rightarrow \mathrm{Ge} + \mathrm{GeO_2}. \tag{4.3}$$

[36] Baba, H. (1956). *Bull. Chem. Soc. Jpn.* **29**, 789–793.

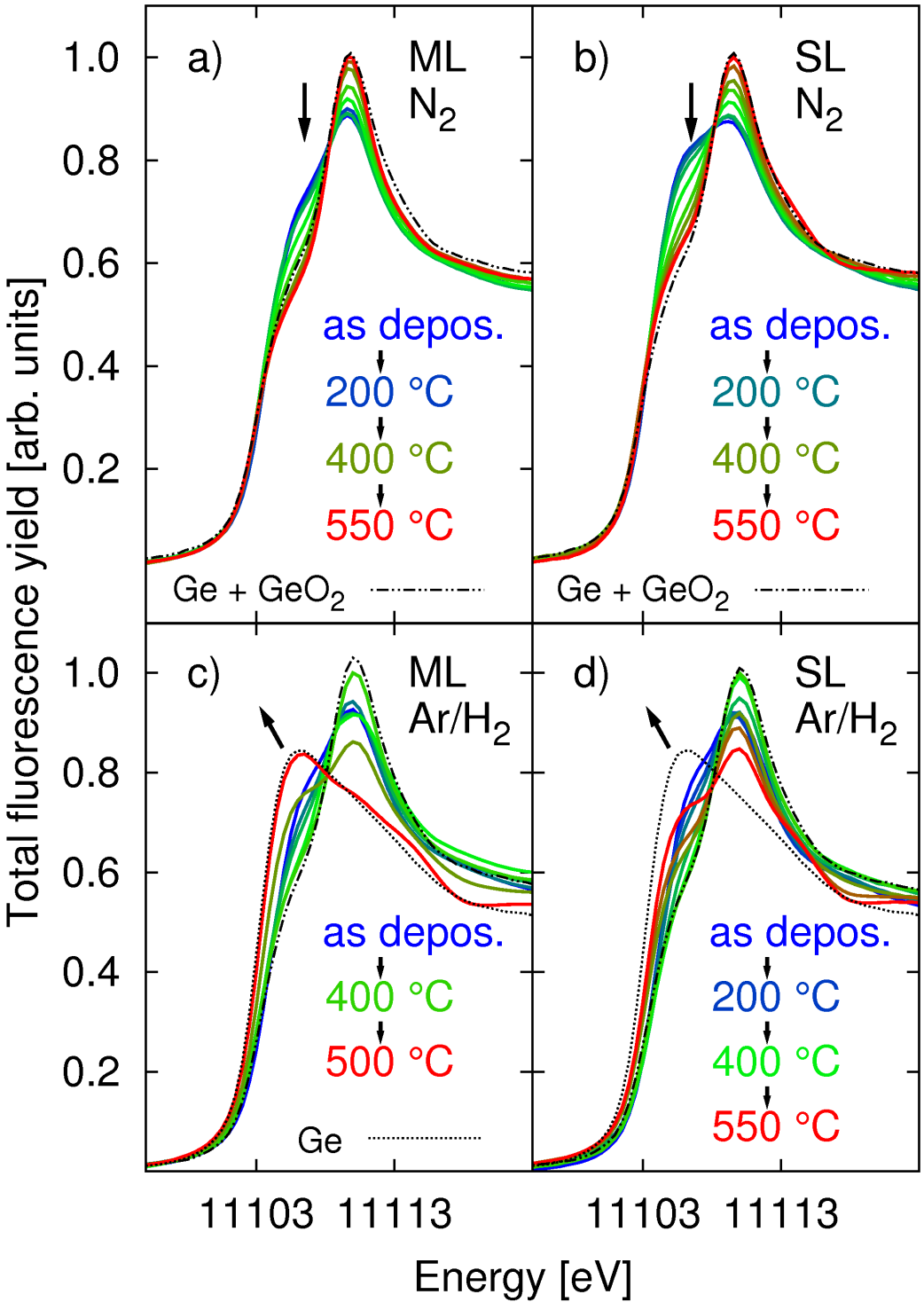

Figure 4.8: XANES spectra of the samples in their native state and after annealing in an inert N_2 atmosphere a) ML and b) SL) and in Ar/H_2 c) ML and d) SL). The temperature progression in 50 °C steps is indicated by a color progression from blue (as deposited) via green to red (highest annealing temperature). The spectra of the a-Ge reference sample (dashed line) and a 1:1 superposition of the a-Ge and a-GeO_2 samples (dashed dotted line) are also shown.

If H_2 is present in the sample, mobile OH molecules can be formed from the sub-oxide by

$$2\mathrm{GeO} + \mathrm{H_2} \rightarrow 2\mathrm{Ge} + 2\mathrm{OH} \tag{4.4}$$

and benefit the phase separation by oxidizing other sub-oxides as in

$$2\mathrm{GeO} + 2\mathrm{OH} \rightarrow 2\mathrm{GeO_2} + \mathrm{H_2}. \tag{4.5}$$

The mobility of the OH molecules is enhanced with increasing annealing temperature and for $T > 400$ °C may be large enough to allow diffusion out of the GeO layers explaining the reduction at higher temperatures.

The reduction reaction for temperatures > 400 °C causes the stoichiometry of the samples to change and since $A(T)$ is derived by taking the difference of XANES spectra of samples with comparable stoichiometry, $A(T)$ is not a representative measure any more. Instead, a weighted sum of the spectra of the a-Ge and a-GeO_2 reference samples is used to refine the XANES spectra where the weights yield the Ge and GeO_2 fraction contained in the sample. The results of this fitting procedure are shown in Fig. 4.9 b) and demonstrate the reduction of GeO_2 for temperatures above 400 °C when H_2 is present in the annealing atmosphere. The reduction in the ML proceeds faster than in the SL and is almost completed at $T = 500$ °C yielding nanocrystalline Ge layers in accordance with the TEM images and the XRD results. All samples annealed in a N_2 inert gas atmosphere show a nearly constant Ge fraction up to the highest annealing temperature of $T = 500$ °C. The stoichiometries, as derived from RBS, are also shown in the figure (datapoints circled in black) and agree reasonably well with the results from the refinement procedure described.

XANES reveals a phase separation mechanism in the ML and SL samples similar to the findings of bulk a-GeO. However, when H_2 is present in the annealing atmosphere, the phase separation and NC formation is shifted significantly to lower temperatures. Moreover, the NC density can be influenced after the phase separation is almost completed by introducing H_2 to the annealing atmosphere.

4.3 Ge-oxide free Ge nanocrystal formation in multilayered GeSiO/SiO$_2$

An important aspect for the usability of oxide matrix embedded NCs for light emitting devices or photo-voltaics are the NC's surface and/or NC-matrix interface properties. In this respect Ge NCs embedded in a Ge-oxide matrix have been proven to show an increased density of electronically active interface states which lead to a fast non-radiative exciton recombination. This phenomenon results in a considerably smaller photoluminescence yield of Ge NCs especially when embedded in a non-stoichiometric, i.e. $x \neq 2$, GeO_x matrix. For the use in photo-voltaics a maximum exciton lifetime is desirable to allow an efficient charge separation.

Following the approach described in section 4.2 but instead of using dc magnetron sputtering from Ge and Si targets separately to deposit layers of GeO and SiO_2, co-sputtering from both sputter targets was used to deposit $GeSiO_x$ layers separated by thin layers of SiO_2. Temperature treatment of $GeSiO_x$ results in a rearrangement of the constituent elements, where the reduction of Ge-oxides by Si is expected due to the

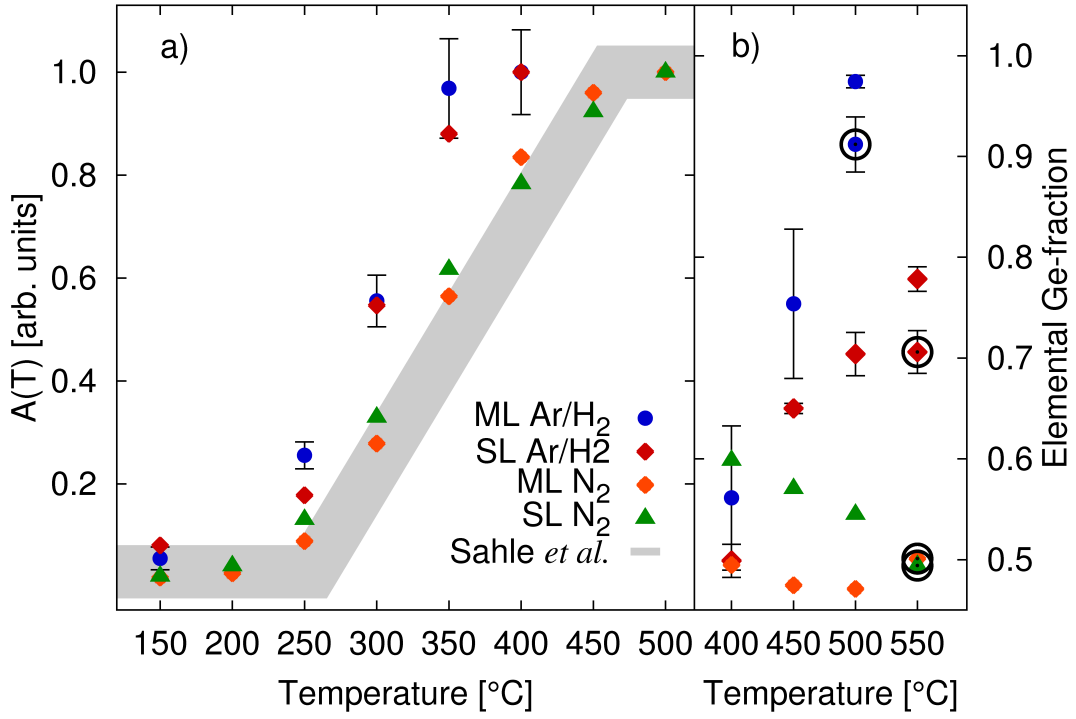

Figure 4.9: a) $A(T)$ of ML and SL sample annealed in an N_2 and Ar/H_2 atmosphere, respectively, as well as the envelope of $A(T)$ values derived from different bulk a-GeO samples (grey shaded area, data was published by Sahle, Ch.J. et al. (2009). *Appl. Phys. Lett.* **95**, 021910–021910). b) Elemental Ge-fraction of the same samples for temperatures above $T = 400$ °C from a fit of a weighted sum of the spectra of a-Ge and a-GeO_2 reference samples. Stoichiometries from RBS data are shown as data points circled in black.

higher enthalpy of formation for SiO_2 ($\Delta H_{SiO_2} = -902$ kcal/mol) compared to GeO_2 ($\Delta H_{GeO_2} = -538$ kcal/mol). This ternary phase separation, thus, will ultimately result in the formation of Ge NCs. With respect to the mentioned NC-matrix interface, the formation of pure Ge crystallites in a stoichiometric SiO_2 matrix preventing the formation of active interface states generating GeO_2 is desired.

The GeSiO/SiO_2 ML samples were prepared by M. Zschintzsch as described in detail by Zschintzsch *et al.*[37] and are comprised of 50 periods of $GeSiO_x/SiO_2$ with a SiO_2 separation layer thickness of 2 nm and a $GeSiO_x$ sublayer thickness of (4.3 ± 0.4) nm, where $x \approx 2$ and the ratio of Ge:SiO_2 is approx. 1. All samples were covered by a 40 nm cap layer to prevent the loss of volatile GeO. To study the influence of the oxygen content x of the sublayer on the amount of GeO_2 formed, three samples of slightly different oxygen content in the GeSiO layer were deposited: sample A has a slight oxygen deficit ($x_A = 1.5$), sample B has an almost stoichiometric oxygen content ($x_B = 1.9$), and sample C has a slight oxygen excess ($x_C = 2.2$).

Size controlled Ge-oxide free Ge NC formation

In order to monitor the nanocrystal formation in the samples, the samples were investigated using XRD[38] in their native state and after the final annealing at 650 °C (samples A and C) and 600 °C (sample B). The results are shown in Fig. 4.10. All native samples show a structure factor as the one shown for sample A in the figure, exemplarily. After the final annealing step, Ge NCs have formed in all samples. The derived NC sizes are 2.5, 3.3, and 3.8 nm for sample A, B, and C, respectively, and thus of the order of the sublayer thickness for samples where the matrix is saturated with oxygen, i.e. sample B and C. In sample A the NC size is smaller than the layer thickness and a higher thermal budget is necessary to produce NCs of the size of the layer thickness.

The crystallization of Ge NCs in a silica matrix requires a higher thermal budget than found for the Ge NC formation in a Ge-oxide matrix by some $100 - 200$ °C. This is in agreement with Zacharias *et al.*[39] who attributed this to a higher a-Ge/SiO_2 interface energy compared to the interface energy of a-Ge/GeO_2.[40] A different interface energy influences the crystal growth velocity which favors the growth of Ge NCs in a GeO_2 matrix.

Phase separation

For the XANES investigation, the samples were annealed *ex situ* consecutively for 30 min in a N_2 inert gas atmosphere. After each annealing step XANES scans of the Ge K-edge were recorded at the materials science beamline BL8 of DELTA, analogous to the procedure described in section 4.2. The results for the three samples are shown in Fig. 4.11. The inset of each sub-figure shows a magnification of the most prominent spectral features between $E = 11104$ eV and $E = 11113$ eV.

Sample A (Fig. 4.11 a)) has an oxygen deficiency and the changes in the absorption edge with increasing annealing temperature are small. Starting at $T = 250$ °C, the spectra ex-

[37] Zschintzsch, M. et al. (2010). *J. Appl. Phys.* **107**, 034306.
[38] The XRD measurements were performed by M. Zschintzsch of the HZDR, Rossendorf, Germany.
[39] Zacharias, M. et al. (1997). *J. Appl. Phys.* **81**, 2384–2390.
[40] Zacharias, M. and Streitenberger, P. (2000). *Phys. Rev. B* **62**, 8391–8396.

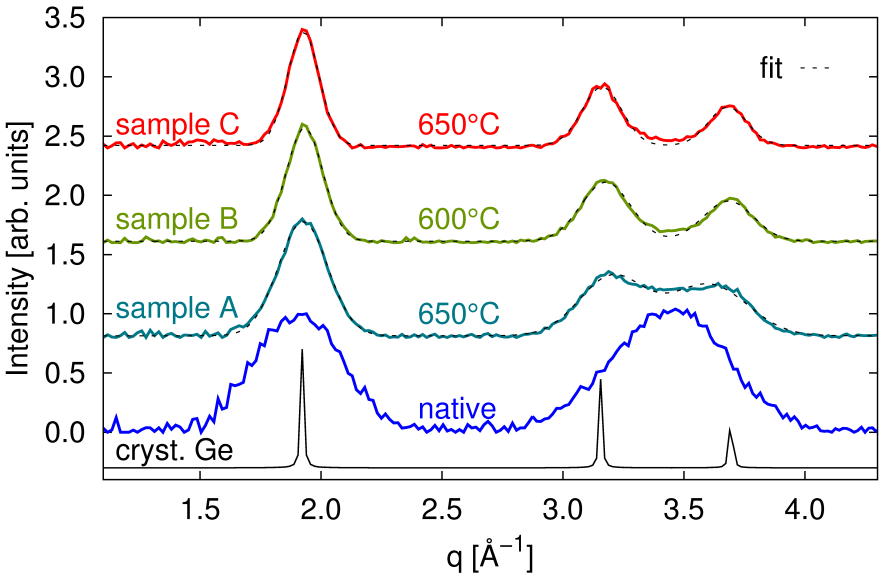

Figure 4.10: XRD patterns of the $GeSiO_x/SiO_2$ multilayer samples A, B, and C which have an oxygen deficit ($x_A = 1.5$), are almost stoichiometric ($x_B = 1.9$), or have an oxygen surplus ($x_C = 2.2$), respectively. The broad structure factor maxima of the native sample is proof of the amorphous structure of the samples in their native state. After the final annealing step, Ge NCs have formed in all samples. See text for details. The XRD analysis was performed by M. Zschintzsch from the HZDR, Rossendorf, Germany.

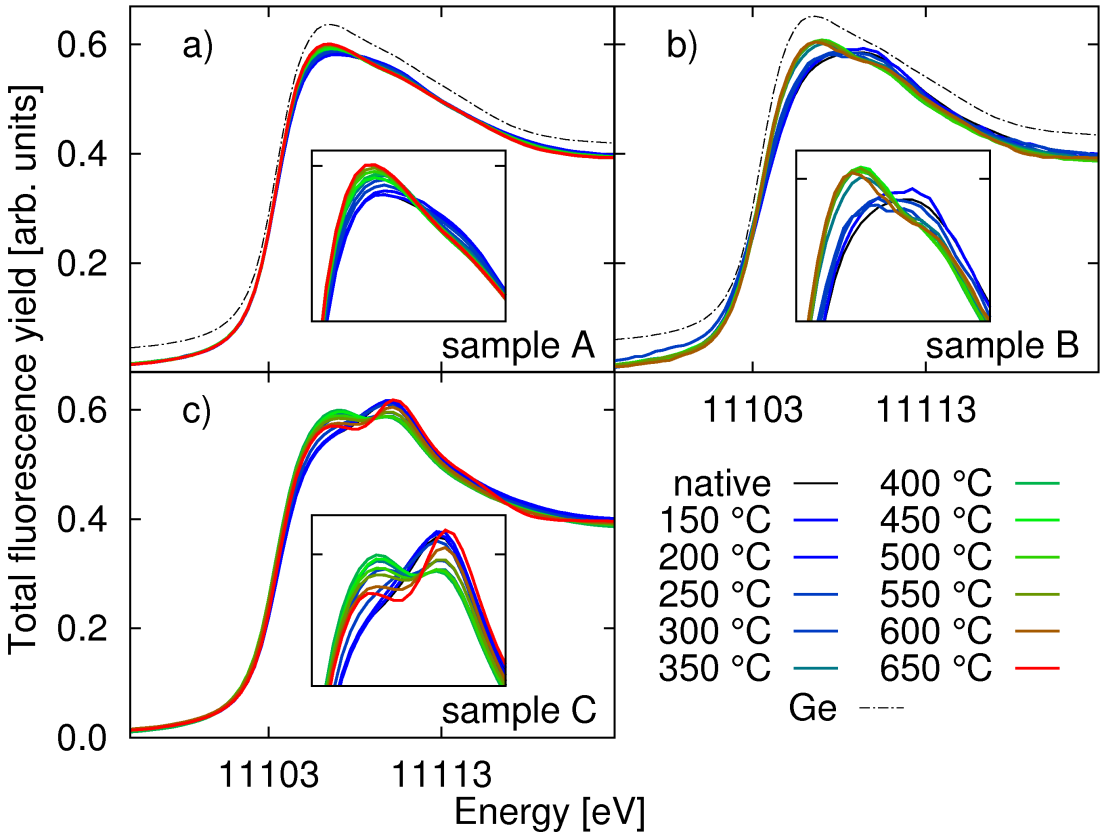

Figure 4.11: XANES spectra of native and differently annealed $GeSiO/SiO_2$ multilayer samples. The insets show a magnification of the most prominent features in the spectra. a) Spectra of sample A which has an oxygen deficit. The sample shows almost no contributions from GeO_2 after the final annealing at 650 °C. The spectrum of the Ge reference sample is shifted vertically for clarity. b) XANES scans of the stoichiometric sample B showing only small GeO_2 contributions. c) Sample C with excess oxygen leading to considerable spectral weight at the position of the GeO_2 white line.

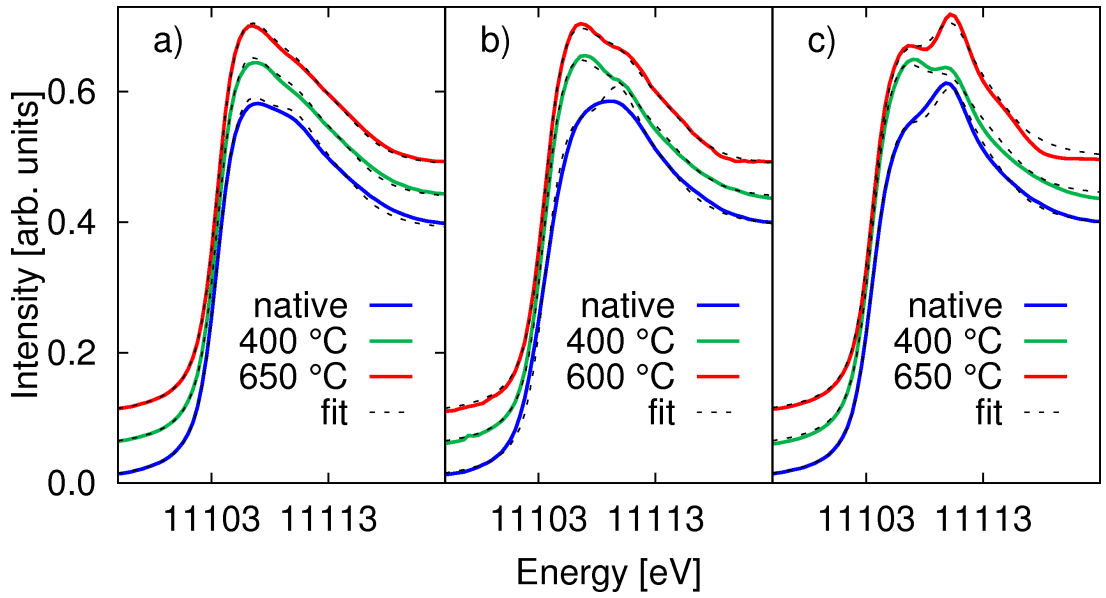

Figure 4.12: XANES spectra of the different $SiGeO_x/SiO_2$ multilayer samples in their native state and after annealing at 400 °C and their highest annealing temperature together with a fit of a weighted sum of the Ge and GeO_2 reference spectra. a) sample A with an oxygen deficit, b) sample B which is almost stoichiometric, and c) sample C which has a small oxygen surplus.

hibit a sharpening of the relatively flat region between $2-5$ eV above the absorption edge and a decrease in spectral weight at the position of the GeO_2 white line (ca. 11110 eV). With increasing temperature, the measured curves resemble more and more the spectrum of the Ge reference sample (dashed black line).

The spectrum of the native sample B shows a lack of spectral weight in the region of the absorption edge of pure Ge and a strong shoulder in the vicinity of the GeO_2 white line. From this it can be inferred that more Ge-oxide species are present in the as-deposited sample. With increasing annealing temperature spectral weight is shifted from the shoulder at $E \approx 11110$ eV to the region of the edge onset of pure Ge at $E \approx 11103$ eV. Above $T = 400$ °C spectral changes are small and a shoulder at the position of the GeO_2 white line remains up to the highest annealing temperature.

With the increased oxygen content of sample C, a higher Ge-oxide content is expected as compared to samples A and B. Indeed, the XANES spectra of sample C show a maximum at $E \approx 11110$ eV, the position of the GeO_2 white line, and a shoulder at $E = 11103$ eV. Up to $T = 500$ °C the temperature dependence of the spectra is similar to that of sample B. For temperatures above 500 °C the effect, however, is reversed. This can be inferred from the increase in white line intensity and decrease in spectral weight in the vicinity of the Ge K-edge onset in elemental Ge. However, a clearly bimodal shape of the spectra above 500 °C persists, indicating that there are no sub-oxides formed. A partial loss of volatile GeO and in-diffusion of oxygen from the annealing atmosphere despite the cap layer may explain this and is in line with a decreased $GeSiO_x$ sublayer thickness and a decreased Ge content as evidenced by XRR and RBS, respectively.

In order to explore the possible occurrence of Ge sub-oxides in the samples, the spectra

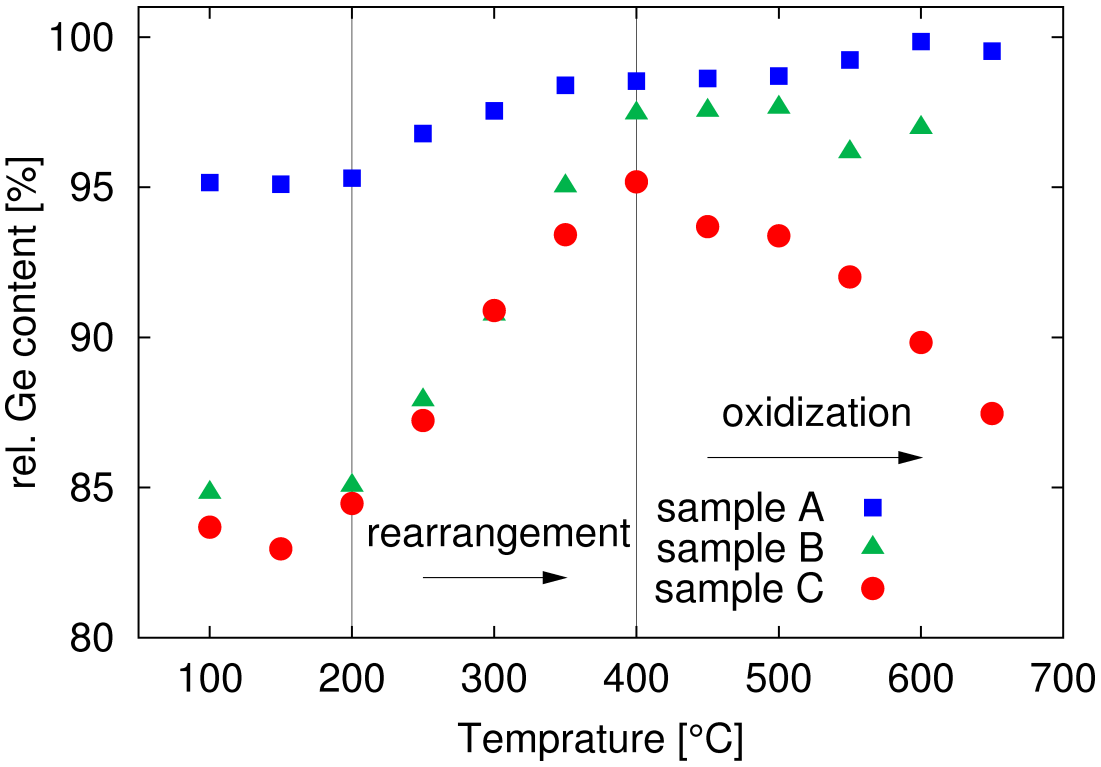

Figure 4.13: Relative Ge content of samples A, B, and C for the different annealing Temperatures as derived from a fit of the weighted sum of the Ge and GeO_2 reference spectra to the experimental data.

of the samples in their native state, after annealing at $T = 400$ °C, and their final annealing temperature are compared with a fit of a weighted sum of the spectra of the Ge and GeO_2 reference samples. A deviation of the samples' spectra in their native state from a weighted sum compared to the spectra at elevated temperatures would indicate the presence of sub-oxides since these sub-oxides are expected to obliterate with increasing annealing temperature similar to the case of bulk a-GeO, hence improving the fit. The results are depicted in Fig. 4.12 showing indeed an improvement of the fit for the annealed samples as compared to the spectra of the native samples. However, since the deviations of the fitted superposition are small even for the native samples, the sub-oxide content can be expected to be relatively small.

As the sub-oxide content is small, the refinement of a superposition of the reference samples' spectra can be extended throughout the entire annealing temperature regime. Similar to the procedure of section 4.2 the weights of the sum correspond roughly to the relative Ge and GeO_2 content in the samples. The resulting Ge content for the three samples for all annealing temperatures are presented in Fig. 4.13. For all samples, the Ge content is $> 85\%$ which stresses the effective suppression of Ge-oxide formation by introducing a silica matrix. The different oxygen contents of the samples are visible as an offset in Ge content, i.e. sample A with an oxygen deficit has the highest, sample B the medium and sample C the lowest Ge content. From the temperature dependence of the Ge content it can be inferred, that temperatures up to 200 °C have little influence on

Sample	x_{native}	$x_{\text{post-anneal}}$
A	1.5	1.9
B	1.9	2.2
C	2.2	2.4

Table 4.3: Summarized stoichiometries x as in $GeSiO_x$ for all samples.

the structure of the samples. Above this temperature a rearrangement of oxygen from remaining Ge-oxides to the Si matrix is evident by an increase in the Ge content up to a temperature of $T = 400$ °C in agreement with the changes observed for the Ge K-edge XANES spectra as discussed above. This is the same temperature regime where the phase separation in the binary GeO_x ($x \approx 1$) systems takes place. For $T = 400 - 500$ °C the Ge content of sample A and sample B is close to unity which would result in the desired Ge-oxide free NCs. At higher temperatures, the Ge content of sample A increases to unity, while it drops slightly for sample B. In contrast, the Ge content in sample C decreases already for temperatures above 400 °C. Using information about the samples' stoichiometry from RBS and the layer thickness from XRR, the decrease in Ge content in samples B and in particular C for temperatures above 400 °C can be interpreted. Comparison of RBS data of the native and post-anneal samples shows that sample B and C lose some of the Ge atoms during the annealing procedure, where the loss is substantial for sample C (30%) and moderate for sample B (7%). Ge loss for sample A is negligible (approx. 2%). Accompanying the loss of Ge atoms, RBS shows an increase in oxygen content for all samples and the stoichiometries of the samples change as summarized in table 4.3. The loss of Ge atoms during the temperature treatment can be traced back to the loss of volatile GeO despite the SiO_2 cap layer. This is in line with the results of the XRR analysis which shows a decreased GeSiO sublayer thickness for samples B and C. The increased oxygen content can be assigned to the intake of oxygen from an oxygen contaminated annealing atmosphere which is in line with an increased silica separation layer thickness for all samples as derived from XRR.

XANES spectroscopy shows that the formation of Ge-oxide free Ge NCs can be embedded in a silica matrix. The deposition of a slightly under-stoichiometric sample allows for the compensation of oxygen contaminants in the annealing atmosphere. The amount of sub-oxides in these ternary systems is small.

4.4 Summary and outlook

The phase separation and formation of Ge NCs in Ge-oxide and silica matrices was investigated using XANES spectroscopy and XRD, respectively. The study of bulk a-GeO_x ($x \approx 1$) showed that significant amounts of Ge sub-oxides are present in the native samples. The sub-oxides disproportionate into Ge and GeO_2 with increasing annealing temperature and Ge NCs are formed after this phase separation process is almost finished. These findings are in favor of a model for the structure of a-GeO in the native state similar to the ICM model derived for bulk a-SiO. With increasing annealing temperature Ge NCs form well before GeO_2 contained in the sample starts crystallizing. This

important fact allows for the production of Ge NCs embedded in an amorphous oxide matrix. Modeling the static structure factor from reference crystallographic atomic clusters using the Debye formula provides an easy and straightforward way to interpret the experimental findings. The agreement between calculated structure factors from clusters containing several thousand atoms and XRD spectra of small samples containing small NCs is remarkable. Likewise, real space cluster codes, i.e. FDMNES, for the calculation of x-ray absorption edges allows one to model and compare XANES spectra of atomic models with the experimental findings. The modeled spectra of elemental Ge, GeO_2, and Ge sub-oxides help corroborate the interpretation of the experimental findings, especially concerning the substantial amounts of Ge sub-oxides contained in the native samples.

Following an approach for the size controlled growth of Si NCs in a silica matrix, size controlled growth of Ge NCs in a Ge-oxide matrix was achieved using GeO_x/SiO_2 ($x \approx 1$) multilayers. Temperature treatment of the GeO_x/SiO_2 multilayers results, similar to the findings of bulk a-GeO, in a phase separation of sub-oxides into Ge and GeO_2 regions and ultimately Ge NC growth. The size control of the Ge NCs is obtained by a confinement in one direction by the period of the multilayer and in the other two, the GeO sublayer plane, by the GeO_2 yield of the disproportionation reaction. Addition of hydrogen to the annealing ambient was proven to influence the structure of the samples even at temperatures well below $T = 500\,^{\circ}\mathrm{C}$ and lower the temperature regime of the phase separation and NC formation by at least 100 °C. A lower crystallization temperature is desirable to decrease the thermal budget needed to produce Ge NCs embedded in an oxide matrix. At elevated temperatures, the reducing properties of hydrogen in the annealing atmosphere can be utilized to enhance the Ge NC density by reducing GeO_2.

The size controlled formation of Ge NCs in a silica matrix was accomplished using $GeSiO_x/SiO_2$ ($x \approx 2$) multilayers. XANES spectroscopy was used to monitor the amount of remaining Ge-oxides depending on the stoichiometry x. Here, Ge-oxide free Ge NCs, in contrast to those embedded in a GeO_2 matrix, are desirable because of the higher number of electronically active interface defect states which quench possible photoluminescence and prevent effective charge separation in potential photo-voltaic applications if embedded in GeO_2. It was found that, in a temperature regime where the phase separation in binary GeO compounds takes place, Ge-oxide species are reduced by unsaturated Si atoms. Further temperature treatment results, depending on the stoichiometry of the SiO_x matrix, in GeO_2 free Ge NCs. Here, a slightly under-stoichiometric SiO_x matrix with $x < 2$ is capable of compensating oxygen contaminants in the annealing atmosphere and the possible loss of volatile GeO.

Although the phase separation and NC formation in bulk a-GeO is now fully characterized in terms of the phase separation parameter $A(T)$ and x-ray scattering data, an understanding in terms of a model of the phase separation process and microscopic structure on an atomic scale, simulations in real space including large numbers of atoms and long time scales would be desirable. This will be a task for future large scale molecular dynamics (MD) simulations. The influence of the Si matrix on the formation of Ge NCs in a silica matrix can be studied by measuring Si absorption edges, such as the Si K- or $L_{2,3}$-edge. Here, XRS (see chapter 2 for details) could prove a valuable tool to study these edges bulk sensitively.

In terms of the applications the presented study aims at, the large scale production of the described structures remains challenging. Here, effort will have to be spent in order

to find and investigate suitable production methods that combine high quality structures and low production costs. Even better suited matrix materials, like the much discussed high k-materials, might be valuable to further increase the properties of oxide matrix embedded NCs.

5 Ba intercalated Si clathrates

Silicon clathrates are compounds which are composed of an extended three dimentional covalent bonded Si network that forms a strong structure made up of face sharing polyhedral cages.[1] The cages can be endohedrally intercalated by guest atoms, where so far a large variety of guest atoms such as alkali metals, alkaline earth-metals, and rare-earth metals have been introduced successfully into the voids[2]. Depending on the type and amount of guests, these clathrates exhibit numerous unusual physical properties. A low thermal conductivity while retaining a high electrical conductivity was found in Na_8Si_{46} which makes this compound a potential highly efficient thermoelectric material.[3] In this respect, Slack *et al.*[4] have proposed the phonon-glass electron-crystal concept as the origin of this property. Within this model, the so-called rattling, or translational vibrations, of the guest atoms disperses acoustic phonons of the crystal leading to a glass-like thermal conductivity.[5] The electronic properties of these clathrates can also be influenced by the type and amount of doping. A transition from semiconductor to metallic behavior, similar to a Mott transition[6], was observed with varying Na content in Na_8Si_{46}.[7] Despite their relatively open network structure Si clathrates exhibit a low compressibility which makes them interesting regarding the search for new super-hard materials.[8]

Group IV clathrates in general and Si clathrates in particular underwent a renewed interest after superconductivity was found in $Na_xBa_ySi_{46}$ $(x + y = 8)$ and Ba_8Si_{46}.[9] This was the first reported discovery of superconductivity in sp^3 covalent bonded structures[10]. The underlying mechanism for superconductivity is still subject of vivid debate. The ongoing scientific discussions include most notably the role of low frequency localized Ba vibrations, or rattling, and the collective Si framework vibrations to electron-phonon coupling as reason for the relatively high superconducting temperatures of Ba_8Si_{46} and anomalous thermal conductivity.[11]

In order to probe these interactions, isotropic compression has proven a valuable tool. So far, XRD and optical Raman scattering have been the experimental means of choice. XRD experiments revealed an isostructural homothetic volume collapse between $12 - 17$ GPa in

---

1 Bobev, S. and Sevov, S.C. (2000). *J. Solid State Chem.* **153**, 92–105.
2 Yamanaka, S. (2010). *Dalton Trans.* **39**, 1901–1915.
3 Tse, J.S. et al. (2000). *Phys. Rev. Lett.* **85**, 114–117.
4 Slack, G.A. (1995). *CRC Press, 1995* **407**,
5 Vining, C.B. (2008). *Nat. Mater* **7**,
6 Mott, S.N. (1978). *Rev. Mod. Phys.* **50**, 203.
7 Pouchard, M. et al. (2002). *Solid State Sci.* **4**, 723–729.
8 San-Miguel, A. et al. (1999). *Phys. Rev. Lett.* **83**, 5290–5293.
9 Kawaji, H. et al. (1995). *Phys. Rev. Lett.* **74**, 1427–1429; Yamanaka, S. et al. (1995). *Eur. J. Sol. State. Inor.* **32**, 799–807; Kawaji, H. et al. (1996). *Solid state commun.* **100**, 393–395; Yamanaka, S. et al. (2000). *Inorg. Chem.* **39**, 56–58.
10 Bobev, S. and Sevov, S.C. (2000). *J. Solid State Chem.* **153**, 92–105.
11 Tanigaki, K. et al. (2003). *Nat. Mater.* **2**, 653–655; Lortz, R. et al. (2008). *Phys. Rev. B* **77**, 224507; Christensen, M. et al. (2008). *Nat. Mater.* **7**, 811–815.

Ba_8Si_{46}[12] and most recently in $Ba_{24}Si_{100}$ at a pressure of approx. 23 GPa[13]. Raman studies confirmed this phase transition and revealed new phase transitions at 7 GPa and possibly 3 GPa.[14] A detailed understanding of the underlying mechanisms responsible for these phase transitions necessitates a detailed understanding of the local atomic environment around the guest atoms as well as of the electronic structure across these phase transitions. SanMiguel *et al.*[15] have investigated the Ba L_3 absorption edge in Ba_8Si_{46} under high pressure conditions and, from an edge shift to higher energies and an increase in white line intensity with increasing pressure, deduced a charge transfer from Si to Ba and an increased disorder in the Si cages across the homothetic volume collapse, respectively. Definite conclusions, though, were limited due to the limited experimental resolution and sensitivity of the Ba L_3 edge to changes in bonding and charge transfer effects.

Ba shows a giant resonance (GR) in the vicinity of the $N_{4,5}$-edge.[16] The shape of this GR was proposed to be dependent on the atomic environment of the Ba atoms.[17] This phenomenon can be studied in these Ba containing Si clathrates as they are composed of Ba atoms encaged in different nanostructured local environments. Thus, detailed spectroscopic investigations of these fascinating and complex materials are highly desirable.

In section 5.1 a study of the Ba GR in Ba intercalated Si clathrates is presented. This investigation was conducted in order to investigate the debated modulations of the giant resonance due to the different local environments of the encaged Ba atoms and to asses the possibility of using the GR as a fingerprinting tool for the study of the geometric and electronic structure of these clathrates across phase transitions. The idea was raised by Sternemann *et al.*[18] who studied the Ba GR in Ba_8Si_{46} under ambient and high pressure conditions as well as for different Ba containing clathrates using XRS. However, the experimental results remained ambiguous regarding the role of double electron excitations and finite momentum transfer in the measurements. These issues were addressed by XRS measurements of the Ba GR of Ba_8Si_{46} and $Ba_{24}Si_{100}$ over a wide momentum transfer range.

The energy regime, where the GR takes place, coincides in large parts with the onset of the K-edge of the often used Be gasket material which complicates the spectroscopic investigation of Ba_8Si_{46} under high pressure conditions. In order to overcome this experimental bottleneck, the Ba $N_{4,5}$-multiplet structure occurring at smaller onset energies than the GR was measured using XRS. The results are presented and integrated into the series of experimental results obtained from other techniques in section 5.2. This study was part of a collaboration of the groups of Prof. M. Tolan (TU Dortmund, Dortmund, Germany) and Prof. J.S. Tse (University of Saskatchewan, Saskatoon, Canada). The presented findings were published as: J.S. Tse, L. Yang, S.J. Zhang, C.Q. Jin, Ch.J.

---

12 San-Miguel, A. et al. (2002). *Phys. Rev. B* **65**, 054109.

13 Toulemonde, P. et al. (2011). *Phys. Rev. B* **83**, 134110.

14 Kume, T. et al. (2003). *Phys. Rev. Lett.* **90**, 155503.

15 Miguel, A.S. et al. (2005). *Europhys. Lett.* **69**, 556.

16 Connerade, J.P. et al. (1987). "Giant resonances in atoms, molecules, and solids."*NATO ASIB Proc. 151: Giant Resonances in Atoms, Molecules, and Solids.* Vol. 1.

17 Wendin, G. and Wästberg, B. (1993). *Phys. Rev. B* **48**, 14764; Luberek, J. and Wendin, G. (1996). *Chem. Phys. Lett.* **248**, 147–152; Connerade, J.P. et al. (2000). *J. Phys. B: At. Mol. Phys.* **33**, 2279; Amusia, M.Y. and Baltenkov, A.S. (2006). *Phys. Rev. A* **73**, 062723.

18 Sternemann, H. et al. (2007*a*). *Phys. Rev. B* **75**, 245102; Sternemann, H. (2008). *A non-resonant inelastic x-ray scattering study on silicon oxides and clathrates.* PhD Thesis, TU Dortmund.

Sahle, C. Sternemann, A. Nyrow, V. Giordano, J.Z. Jiang, S. Yamanaka, S. Desgreniers, and C.A. Tulk (2011). Pressure-induced Electron Topological Transitions in Ba-doped Si Clathrate, Phys. Rev. B 84, 184105.

5.1 Modulations of the Ba GR in Si-Clathrates

Giant resonances are characteristic excitations of many-fermion systems and can be found in atoms, molecules, and solids.[19] In atomic and ionized barium, the GR occurs in the regime of the $4d-f$ transition and has been studied extensively during the past decades.[20] A simple quantum well model explains the origin of these GRs for atoms with $Z \geq 55$ as caused by the centrifugal potential of the nuclear charge.[21] For these atoms the well potential is strong enough to cause the $4f$ wave functions to collapse into the well and thus overlap spatially with the 4d orbitals. This in turn leads to a strong $4d-f$ excitation channel.

From a condensed matter perspective, Zangwill[22] pointed out that a GR can be understood in terms of strongly damped collective oscillations of the electrons of entire atomic sub-shells in the electromagnetic field of the screened x-ray wave. Below resonance, the induced dipolar charge separation within the sub-shell oscillates in phase with the external field and screens this field within the sub-shell's mean radius. Above the onset of the resonance, this situation is reversed and the external field is amplified within the sub-shell. This gives rise to suspect that giant resonances can be modeled using time dependent local density approximation (TDLDA).

Contradictory to the perception of giant resonances as an inherently atomic feature, Wendin and Wästberg[23] predicted changes in the shape of the giant resonance of Ba when intercalated in complex cage-like surroundings. Indeed, calculated x-ray absorption spectra using TDLDA showed a dependence on the surrounding of the resonating atoms for e.g. Ba and Xe encapsulated in fullerenes[24].

First experiments evidencing variations of the GR shape in Ce-halides in comparison to the metal were reported as early as 1975 by Suzuki *et al.*[25]. More recent experiments on C_{82} encaged lanthanides showed first hints for a modulation of the giant resonances of atoms in complex surroundings.[26] However, the limited statistical accuracy of their experiments

---

[19] Connerade, J.P. et al. (1987). "Giant resonances in atoms, molecules, and solids."*NATO ASIB Proc. 151: Giant Resonances in Atoms, Molecules, and Solids.* Vol. 1; Sternemann, C. et al. (2008). *J. Anal. At. Spectrom.* **23**, 807–813.

[20] Connerade, J.P. et al. (1987). "Giant resonances in atoms, molecules, and solids."*NATO ASIB Proc. 151: Giant Resonances in Atoms, Molecules, and Solids.* Vol. 1; Richter, M. et al. (1989). *Phys. Rev. A* **40**, 7007; Brechignac, C. and Connerade, J.P. (1994). *J. Phys. B: At. Mol. Phys.* **27**, 3795.

[21] Connerade, J.P. et al. (1987). "Giant resonances in atoms, molecules, and solids."*NATO ASIB Proc. 151: Giant Resonances in Atoms, Molecules, and Solids.* Vol. 1.

[22] Zangwill, A. (1987). "A Condensed Matter View of Giant Resonance Phenomena."*NATO ASIB Proc. 151: Giant Resonances in Atoms, Molecules, and Solids.* Vol. 1, 321.

[23] Wendin, G. and Wästberg, B. (1993). *Phys. Rev. B* **48**, 14764.

[24] Luberek, J. and Wendin, G. (1996). *Chem. Phys. Lett.* **248**, 147–152; Amusia, M.Y. and Baltenkov, A.S. (2006). *Phys. Rev. A* **73**, 062723.

[25] Suzuki, S. et al. (1975). *J. Phys. Soc. Jpn.* **38**, 156.

[26] Mitsuke, K. et al. (2005*a*). *J. Chem. Phys.* **122**, 064304; Mitsuke, K. et al. (2005*b*). *Int. J. Mass Spectrom.* **243**, 121–125; Katayanagi, H. et al. (2008). *J. Quant. Spectrosc. Ra.* **109**, 1590–1598.

hardly allows for definite conclusions. Müller *et al.*[27] presented spectra of higher quality of Ce encaged C_{82}^+ fullerenes which seemed to exclude the occurrence of a shape modulation by the comparison of spectra of the encaged and isolated Ce atoms, however, a significant redistribution of decay channels of the Ce atom encapsulated in a cage in contrast to the free atom was proclaimed. This was underlined by a recent theoretical study of Madjet *et al.*[28]. Korol *et al.*[29] pointed out that the displacement of the resonating atom within the cage due to either a static displacement, i.e. through hybridization with the cage atoms, or thermal excitation can strongly suppress confinement resonances explaining the discrepancy between theoretical predictions and experimental results. Kilcoyne *et al.*[30] reported an enhancement of double photo-ionization for Xe atoms encaged in C_{60} and in addition found an oscillatory structure in the photo-absorption cross section which they attributed to the multipath interference of the outgoing 4d photo-electron wave with its transmitted and reflected self from the carbon cage.

As mentioned in the introduction to this chapter, investigations by Sternemann[31] showed first clear modulations of the GR of Ba in Ba containing Si clathrates. The questions raised regarding the influence of finite momentum transfer in their measurements and the role of double electron excitations will be addressed in the following.

The structures of the different Ba containing clathrates and compounds under investigation are shown in Fig. 5.1 together with the local environment of the non-equivalent atoms in the respective unit cell. $BaSi_6$ crystallizes in the space group Cmcm and a single non-equivalent Ba atom occupies an irregularly shaped Si_{18} polyhedron. These polyhedra are connected by sharing faces to form Ba containing tunnels[32] (Fig. 5.1 a)). Ba_8Si_{46} has two non-equivalent Ba atoms in each unit cell one of which is occupying a Si_{20} (this Ba atom is referred to as Ba(S) from here on) and the second one occupies a Si_{24} cage (referred to as Ba(L) from here on). Two pentagonal dodecahedra (Si_{20}) and six tetrakaidecahedra (Si_{24}) are connected by sharing faces forming a space filling crystal structure.[33] The resulting crystal structure has cubic symmetry and is usually referred to as a type-I clathrate. The crystal structure and the two cages are shown in Fig. 5.1 b). $Ba_{24}Si_{100}$ was first prepared by Fukuoka *et al.*[34] under high pressure and high temperature conditions. It forms a chiral network of Si_{20} cages which host one non-equivalent Ba atom per unit cell. Two more non-equivalent Ba atoms placed in an open Si_{20} cage and a small pseudo-cubic Si_8 space, respectively. In each cubic unit cell of space group $P4_132$ there are eight symmetric Si_{20}, four pseudo-cubic Si_8 spaces, and 12 open Si_{20} cages. This structure is shown schematically in Fig 5.1 c) and is referred to as a type-III clathrate. In a sense, type-III clathrates may be viewed as a modification of type-I clathrates where four Si atoms have been removed from the large Si_{24} cage.[35] All crystallographic information is

---

27 Müller, A. et al. (2007). "Photoionization of the endohedral fullerene ions $Sc_3N@C_{80}^+$ and $Ce@C_{82}^+$ by synchrotron radiation."Vol. 88, 012038; Müller, A. et al. (2008*a*). *Phys. Rev. Lett.* **101**, 133001.

28 Madjet, M.E. et al. (2010). *Phys. Rev. A* **81**, 013202.

29 Korol, A.V. and Solov'yov, A.V. (2010). *J. Phys. B: At. Mol. Phys.* **43**, 201004.

30 Kilcoyne, A.L.D. et al. (2010). *Phys. Rev. Lett.* **105**, 213001.

31 Sternemann, H. (2008). *A non-resonant inelastic x-ray scattering study on silicon oxides and clathrates*. PhD Thesis, TU Dortmund.

32 Yamanaka, S. and Maekawa, S. (2006). *Z. Naturforsch.* **61b**, 1493–1499.

33 Yamanaka, S. et al. (2000). *Inorg. Chem.* **39**, 56–58.

34 Fukuoka, H. et al. (2000). *J. Organomet. Chem.* **611**, 543–546.

35 San-Miguel, A. et al. (1999). *Phys. Rev. Lett.* **83**, 5290–5293.

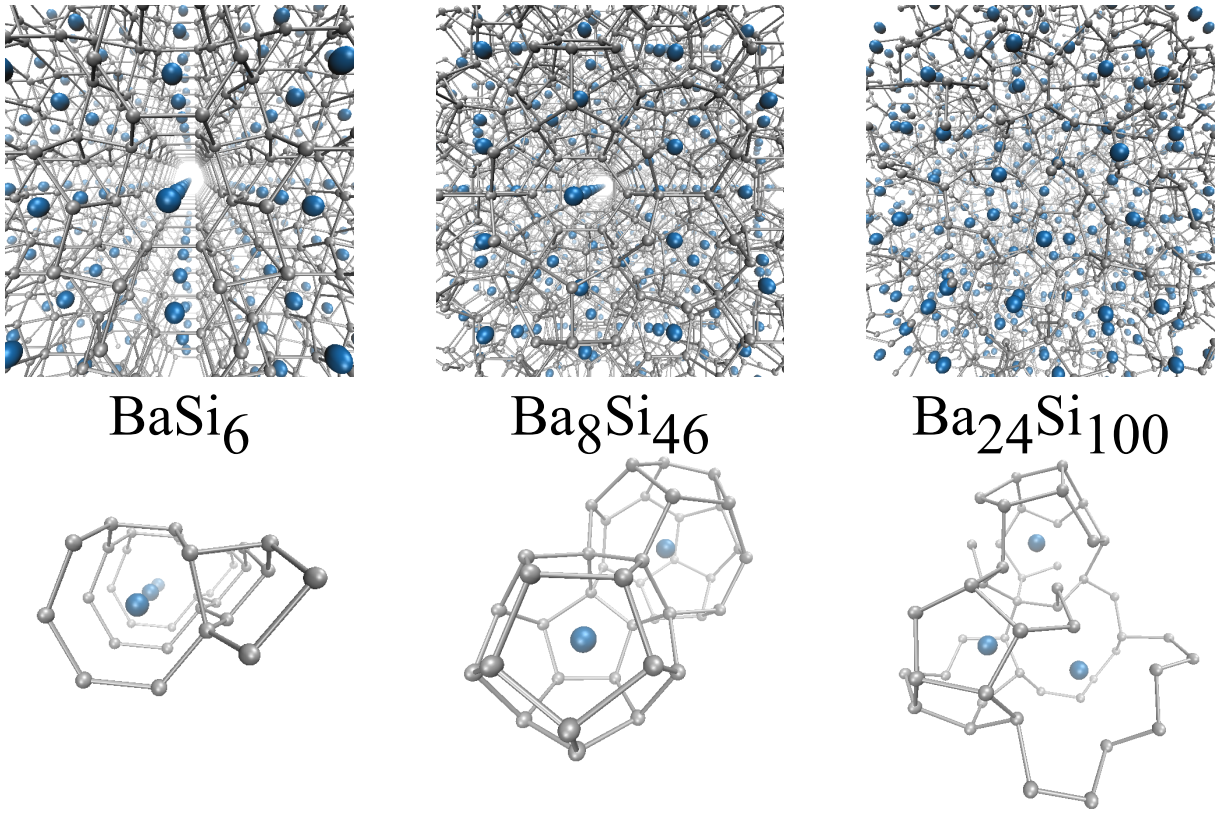

Figure 5.1: a) Crystal structure of $BaSi_6$ (top) and single non-equivalent Ba atom in the unit cell in its tube like surrounding (bottom). b) Type-I clathrate structure (top) and the two Ba filled cages of which Ba_8Si_{46} is composed of (bottom). c) Type-III clathrate structure of $Ba_{24}Si_{100}$ (top) and the three non-equivalent Ba atoms in the unit cell which occupy two open cages and one void (bottom). The more complex local environments of the compounds from left to right is evident.

Compound	Space group	a [Å]	b [Å]	c [Å]	N_{Ba}
$BaSi_6$	Cmcm	4.49	10.38	11.97	1
Ba_8Si_{46}	$Pm\bar{3}n$	10.33	–	–	2
$Ba_{24}Si_{100}$	$P4_132$	14.07	–	–	3

Table 5.1: Summary of crystallographic parameters of the compounds measured and analyzed. N_{Ba} is the number of non-equivalent Ba atoms in the unit cell.

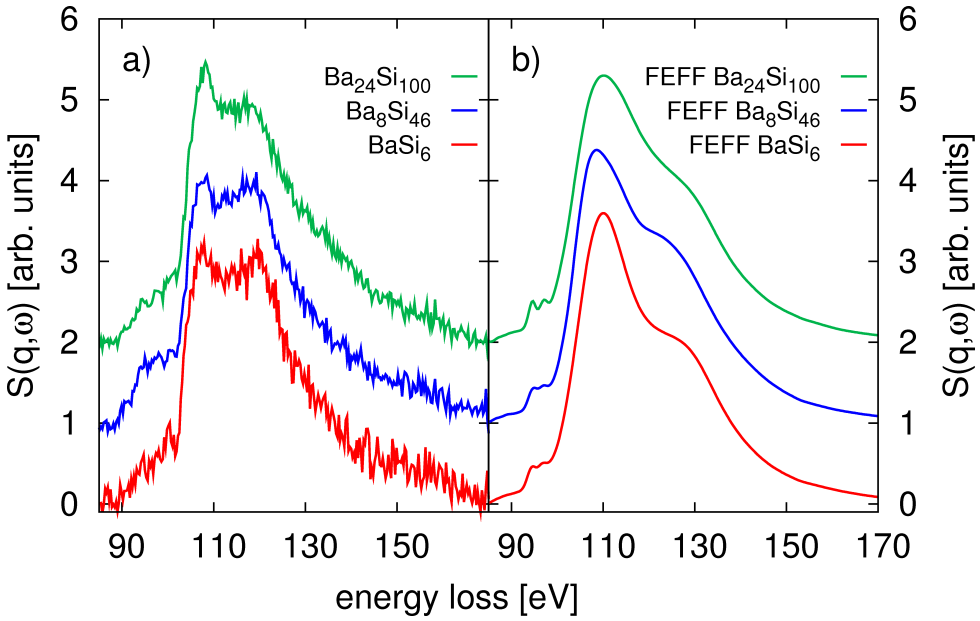

Figure 5.2: a) Experimental spectra of the different Ba containing clathrates and compounds Ba_8Si_{46}, $Ba_{24}Si_{100}$, and $BaSi_6$. Experimental data taken from Sternemann, H. (2008). *A non-resonant inelastic x-ray scattering study on silicon oxides and clathrates*. PhD Thesis, TU Dortmund. b) Simulated absorption spectra of the $N_{4,5}$ absorption edge in the named clathrates and compounds.

summarized in table 5.1.

As was shown by Sternemann[36], the GR in Ba can be reproduced qualitatively using the FEFF program package employing TDLDA. However, the use of TDLDA is not supported by FEFF9 for q-dependent calculations. Therefore, calculations of the GR with the cluster code FEFF9 are only possible in the dipole limit, i.e. the corresponding absorption spectra. As pointed out in chapter 2 a comparison of XAS and XRS spectra is justified for small momentum transfers. To simulate the spectra of the investigated clathrates and compounds, the Ba $N_{4,5}$ absorption spectra were calculated for each non-equivalent atom in the unit cell and the resulting spectra were normalized by a normalization factor provided by the TDLDA card of the program package and added up accounting for the corresponding multiplicity.

[36] Sternemann, H. (2008). *A non-resonant inelastic x-ray scattering study on silicon oxides and clathrates*. PhD Thesis, TU Dortmund.

Experimental results taken from Sternemann[37] together with spectra calculated in the dipole limit are shown in Fig. 5.2. All spectra were normalized to the integrated intensity in the region $101 - 150$ eV energy loss. The spectra are dominated by the GR at energy losses between $101 - 165$ eV. In this energy range, all materials show a broad two peak structure with two broad maxima at 108 and 119 eV. Whereas the spectra of $BaSi_6$ and Ba_8Si_{46} are very similar to $BaSi_6$ showing only a slightly sharper first maximum, the GR of $Ba_{24}Si_{100}$ exhibits a strong first maximum while showing a shoulder structure at the position of the second maximum observed for $BaSi_6$ and Ba_8Si_{46}.

The general shape of the resonances are well reproduced and a qualitative agreement between the experimental results and the calculations can be observed. The second maximum around 119 eV is strongly suppressed in the calculated spectra of all materials as compared to the experimental findings. However, a clearly pronounced shoulder structure between $120 - 130$ eV is present in the simulated spectra of $BaSi_6$ and Ba_8Si_{46} whereas the calculated $Ba_{24}Si_{100}$ spectrum only shows a weak shoulder at this position analogous to the experimental findings.

It has been discussed earlier that besides a possible resonance modulation induced by the surroundings predicted by Wendin[38], double ionization processes could significantly contribute to the spectrum in the energy loss range between 111 and 130eV.[39] Several authors discussed the possibility that such double electron excitations might obscure the GR's shape.[40] Double ionization processes are not accounted for in the theoretical approach. Likewise, the finite momentum transfer XRS measurements, i.e. non-negligible contributions arising from multipole transitions in the experimental spectra, could complicate a direct comparison with theory.

In order to assess the influence of finite momentum transfer, measurements of $Ba_{24}Si_{100}$ and Ba_8Si_{46} over a large momentum transfer range were performed using the LERIX setup of the APS beamline 20-ID-B (compare chapter 3.3). The extracted spectra (run 2) together with the results of Sternemann *et al.* (run 1) are depicted in Fig. 5.3. A direct comparison between spectra of run 1 and run 2 averaged over momentum transfers between $1.90 - 3.17$ Å^{-1} is shown in Fig. 5.3 a) and b) and demonstrates the accordance of the two experimental data sets. The higher statistical accuracy of data from run 1 favors these data for all discussions except the momentum transfer dependence. Spectra for each momentum transfer are shown in Fig. 5.3 c) and d). The second maximum of the GR around 119 eV loses spectral weight for decreasing momentum transfer for both compounds. This is quantified by the ratio of the height of the second and first peak which is plotted against the according momentum transfer in Fig. 5.3 e) and f) for $Ba_{24}Si_{100}$ and Ba_8Si_{46}, respectively. Linear regression and extrapolation to $q = 0$ nearly reproduces the peak height ratio of the TDLDA calculations in the case of $Ba_{24}Si_{100}$ and fits well for that of Ba_8Si_{46}. Thus, contributions arising from a finite momentum transfer in the experimental spectra largely account for the difference in spectral weight in the vicinity of the second maximum of the GR. However, the calculated spectrum still shows

[37] Sternemann, H. (2008). *A non-resonant inelastic x-ray scattering study on silicon oxides and clathrates*. PhD Thesis, TU Dortmund.

[38] Wendin, G. and Wästberg, B. (1993). *Phys. Rev. B* **48**, 14764.

[39] Sternemann, H. (2008). *A non-resonant inelastic x-ray scattering study on silicon oxides and clathrates*. PhD Thesis, TU Dortmund.

[40] Richter, M. et al. (1989). *Phys. Rev. A* **40**, 7007; Crljen, Z. et al. (1994). *Phys. Rev. A* **50**, 3529; Müller, A. et al. (2008*b*). *Phys. Rev. Lett.* **101**, 133001.

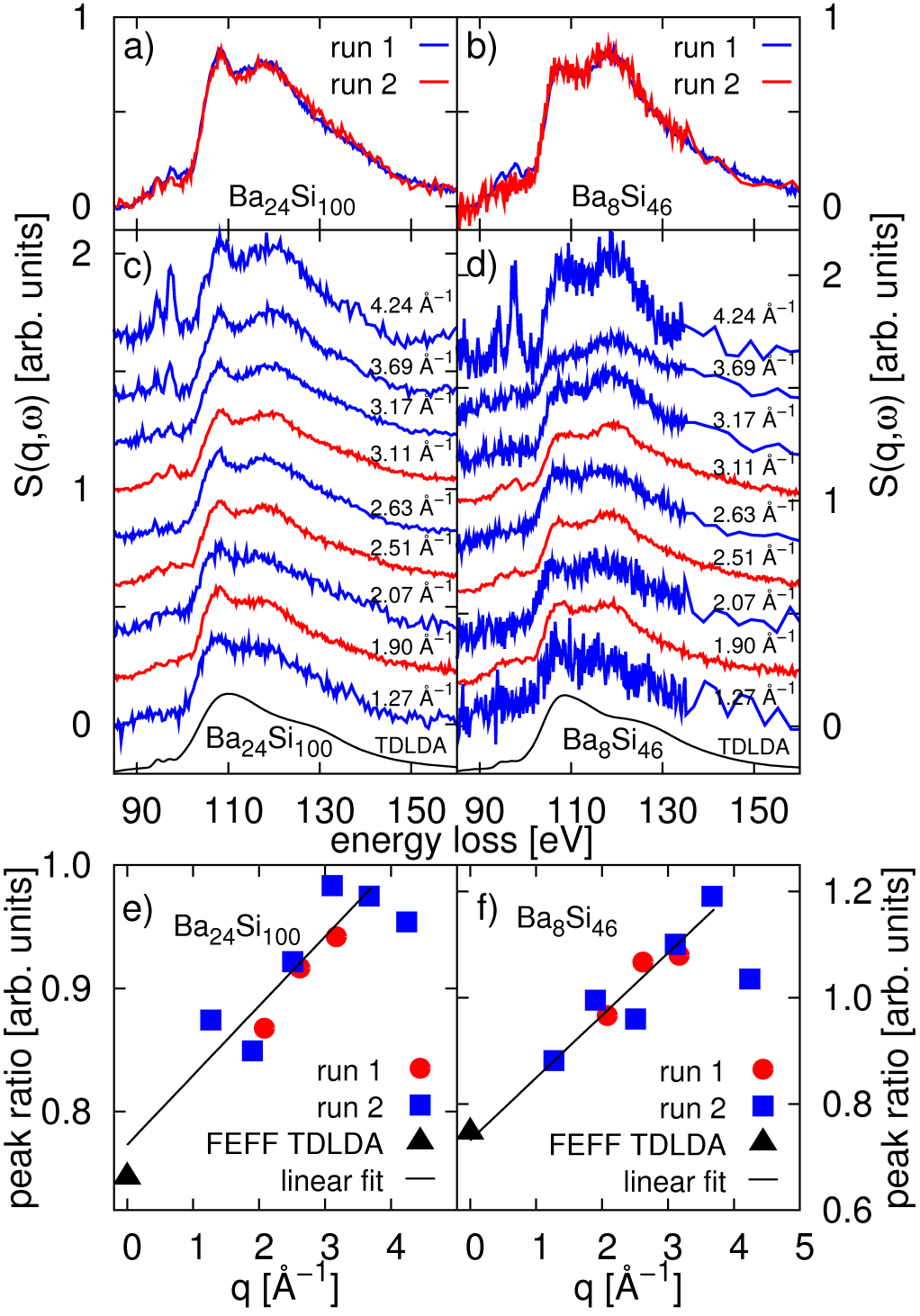

Figure 5.3: Comparison of experimental data from run 1 and run 2 for a) $Ba_{24}Si_{100}$ and b) Ba_8Si_{46}, averaged over momentum transfers of $1.90 - 3.17$ Å^{-1} showing the comparability of the two experimental data sets. Measurements of the Ba GR of c) $Ba_{24}Si_{100}$ and d) Ba_8Si_{46} over a large energy range. The second maximum systematically loses spectral weight with decreasing momentum transfer value which is given on the right side of each of the plotted data sets. Peak height ratios for e) $Ba_{24}Si_{100}$ and f) Ba_8Si_{46} and extrapolation to $q = 0$ show good agreement with the calculated absorption edge. Red curves and data points are taken and/or derived from Sternemann, H. (2008). *A non-resonant inelastic x-ray scattering study on silicon oxides and clathrates*. PhD Thesis, TU Dortmund.

deviations in peak intensities around 119 eV energy loss. Moreover, the second maximum in the calculations is shifted to higher energies by approx. $8-10$ eV. Fig. 5.4 a) depicts the difference between spectra of successive q values of run 1 for all compounds. This representation again points out the systematic dependence of the spectra on the value of the momentum transfer q. The differences show an increase of the first maximum (positive difference in the regime $100-120$ eV energy loss) and a decrease of the second maximum (negative difference in the regime $120-150$ eV energy loss) with decreasing momentum transfer value. This q-dependence is similar for Ba_8Si_{46} and $Ba_{24}Si_{100}$ and thus not depending on the local environment of the Ba atoms.

Modulations of the GR for the different samples are most clearly visible when the differences between the spectra and a reference compound are examined. Here, the spectrum of $Ba_{24}Si_{100}$ was chosen as a reference sample as it shows the highest statistical accuracy. The differences between the GR of $Ba_{24}Si_{100}$ reference and the spectra of Ba_8Si_{46} and $BaSi_6$ are shown in Fig. 5.4 b) for each of the three momentum transfers measured by Sternemann *et al.*[41] and an average over the three momentum transfers in part c). Since the differences are very similar for different momentum transfers this averaging is justified. As expected from the overall shape of the GR, the difference between the $Ba_{24}Si_{100}$ reference and the two compounds Ba_8Si_{46} and $BaSi_6$ is prominent in the regime of the two maxima, namely at approx. 108 eV and 119 eV energy loss. This clearly demonstrates a change in the Ba GR's shape for $Ba_{24}Si_{100}$ as opposed to Ba_8Si_{46} and $BaSi_6$. Comparing the two differences with each other leaves to conclude that a GR modulation between Ba_8Si_{46} and $BaSi_6$, if existing, is beyond the detection limits in this experiment. Notably, the average over all differences between successive q values from Fig. 5.4 a), plotted in the background of Fig. 5.4 c), shows an opposing trend compared to the modulations of the GR between the compounds. Thus, clear evidence for a different modulation of the Ba GR in different local environments is found and can most importantly be excluded to originate in the finite momentum transfer inherent to the XRS measurements.

The origin of the change in GR shape between $Ba_{24}Si_{100}$ on the one hand and Ba_8Si_{46} and $BaSi_6$ on the other can now be discussed. From a structural point of view the two Ba atoms in Ba_8Si_{46} (Ba(L) and Ba(S)) and the single unique Ba atom in $BaSi_6$ are contained in symmetric surroundings. In $Ba_{24}Si_{100}$, on the contrary, only one of the three non-equivalent Ba atoms is situated within an intact polyhedron which amounts to eight of the 24 Ba atoms in each unit cell. The two other Ba atoms in $Ba_{24}Si_{100}$ are contained in an open Si_{20} cage and pseudo Si_8 space and thus are contained in asymmetric environments. This might explain the similarity of the GR of the two structures Ba_8Si_{46} and $BaSi_6$ compared to the GR of $Ba_{24}Si_{100}$. Moreover, in $BaSi_6$ the Si_{18} cages are connected to form Ba containing tunnels, in Ba_8Si_{46} the two cages are linked by sharing faces in a way that also a Ba containing tunnel is formed whereas none of the Ba atoms in $Ba_{24}Si_{100}$ can be referred to as being situated within a Si tunnel.

Although the calculated spectra (see Fig. 5.5) show only qualitative agreement with the experimental findings and thus cannot be used for a direct comparison with the experimental data, calculations may be useful to support this hypothesis about the origin of the modulations between the measured compounds. The influence of the cage's shape is exemplified in Fig. 5.5 a) by a comparison of the GR calculated for a Ba atom inside a Si_{24}

[41] Sternemann, H. (2008). *A non-resonant inelastic x-ray scattering study on silicon oxides and clathrates.* PhD Thesis, TU Dortmund.

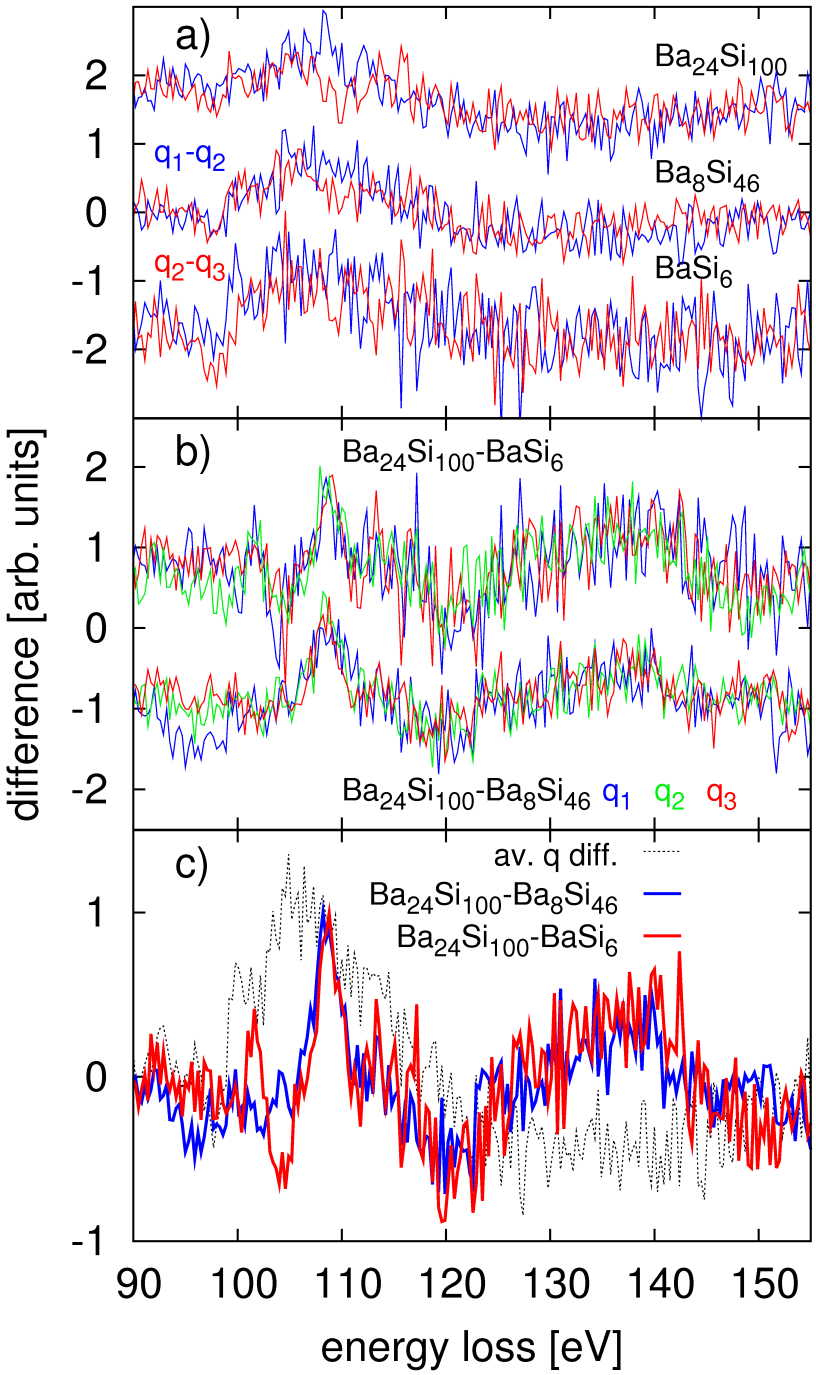

Figure 5.4: a) Differences between XRS spectra measured for consecutive momentum transfers for the compounds $Ba_{24}Si_{100}$ and Ba_8Si_{46}. b) Differences between the GR of Ba_8Si_{46} and $BaSi_6$ from that of $Ba_{24}Si_{100}$ for three momentum transfers. c) Differences between the GR of Ba_8Si_{46} and $BaSi_6$ from that of $Ba_{24}Si_{100}$ averaged over all three momentum transfers and an average over the q-dependent differences from a) showing an opposite trend which clarifies that a shape modulation can clearly be separated from the q-dependence of the spectra.

cage and the Ba atom inside a pseudo-cubic Si_8 space. The two-peak-structure in the GR of the Ba atom inside a Si_{24} cage is smeared out for the Ba atom inside a pseudo-cubic Si_8 space. Since a single simulation might not be reliable, the influence of an opening of a Si_{24} cage and of an off-centered Ba position within a Si_{24} cage was modeled by successively reducing the number of Si atoms of the cage and successively increasing the off-center position of a Ba(L) atom, respectively. Thus, in both series of calculations an increasing degree of artificial asymmetry is induced to observe systematic changes in the resulting spectra and compare them to the trends in the experimental data. The results of these calculations are shown in Fig. 5.5 b) and c). Opening up a Si_{24} cage, i.e. breaking the symmetry of the cage, shifts the first maximum to slightly higher energy losses and most notably reduces the intensity of the second maximum. A similar trend can be observed when the Ba atom is displaced from the center of the cage, i.e. the first maximum shifts to higher energy losses and the two peak structure is smeared out. This is in line with the results of Korol *et al.*[42]. As pointed out, the structure of $Ba_{24}Si_{100}$ can be viewed as modification of the Ba_8Si_{46} structure with four Si atoms missing in the large Si_{24} cages. Moreover, the chiral nature of the arrangement of the cages prevents the formation of Si tunnels. Thus, the observed modulation of the GR of $Ba_{24}Si_{100}$ as compared to those of Ba_8Si_{46} and $BaSi_6$ might be caused by the more complex and less symmetric surroundings of the Ba atoms in $Ba_{24}Si_{100}$, especially in the open Si_{20} and pseudo-cubic Si_8 cages. The observed trend in the simulated data with increasingly asymmetric surrounding of the Ba atoms, in particular a loss of intensity in the vicinity of the second maximum at approx. 119 eV, is also observed when comparing the GR of Ba_8Si_{46} and $BaSi_6$ with the GR of $Ba_{24}Si_{100}$. Thus, the formulated hypothesis of a different modulation of the GR for Ba contained in different local environments is supported by the presented simulations.

The influence of finite momentum transfer on the GR of Ba atoms in different Si clathrates was investigated by studying the q-dependence of these GRs for Ba_8Si_{46} and $Ba_{24}Si_{100}$ and comparison with calculations employing TDLDA. Finite momentum transfer explains for a major part of the differences between experiment and calculations leaving one to suspect that double electron excitations have little influence on the spectra's shape. The similarity of the GR of Ba_8Si_{46} and $BaSi_6$ compared to the GR of $Ba_{24}Si_{100}$ suggests structural influences as the cause of a modulation. In particular, the more complex and less symmetric surrounding of the Ba atoms in $Ba_{24}Si_{100}$ seems to change the GR's shape significantly compared to the Ba GR of compounds with higher symmetry. This is supported by calculations of a series of spectra of Si_{24} cages when systematically inducing asymmetry by removing cage atoms or displacing the Ba atom from the center of the cage.

The similarity of the GR of Ba_8Si_{46} and $BaSi_6$ suggests that the experimental accuracy of the presented measurements is still insufficient to study in detail the changes in bonding and structure across phase transitions as observed for Ba_8Si_{46} and $Ba_{24}Si_{100}$ when high pressure is applied. A way to circumvent this obstacle is presented in the following section.

[42] Korol, A.V. and Solov'yov, A.V. (2010). *J. Phys. B: At. Mol. Phys.* **43**, 201004.

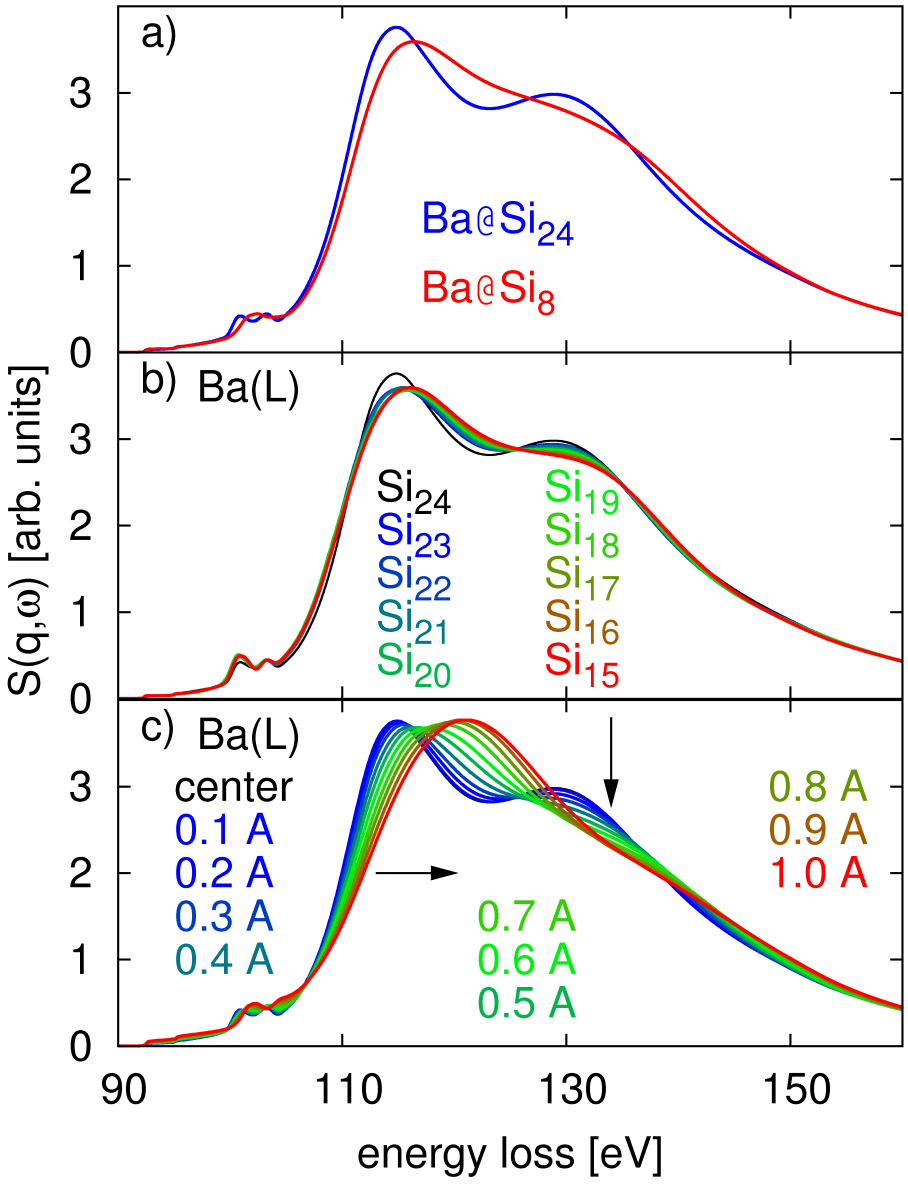

Figure 5.5: a) Ba GR of a Ba atom in a symmetric Si_{24} cage in comparison with the GR of a Ba atom inside a Si_8 cage. The two peak structure observed for the Ba atom in the Si_{24} cage is smeared out for the Ba atom in the Si_8 space. b) Series of calculations of the GR of a Ba atom in a symmetric Si_{24} cage showing the influence of consecutively stripping Si atoms from the cage. With a decreasing number of Si atoms in the cage, the first maximum shifts slightly to higher energy losses whereas the second maximum loses spectral weight. c) Influence of asymmetry within a Si_{24} cage by a series of calculations where the Ba atom is consecutively displaced from the center. The first maximum shifts towards higher energies while the second maximum loses intensity. All calculations show a smearing of the spectral features when asymmetry is induced.

5.2 Pressure induced phase transitions in Ba_8Si_{46}

As pointed out in the introduction to this chapter, a detailed understanding of the mechanisms responsible for the high pressure phase transitions of Ba_8Si_{46} and $Ba_{24}Si_{100}$ are still elusive. Apart from information about the structural changes across these phase transitions as explored by XRD, a complementary direct study of the electronic structure in these materials is essential. Here, XAFS has proven a valuable tool and studies of the Ba L_3 edge in Ba_8Si_{46} under high pressure conditions using conventional absorption spectroscopy yield an energy shift in the edge position to smaller energies with increasing pressure.[43] This shift is of the order of 0.6 eV over the entire pressure range and was related to a charge transfer from the Si cage atoms to the Ba guests. For pressures above 10 GPa also an increase in white line intensity was observed. This change in white line intensity was attributed to an increasingly distorted environment of the Ba atoms with increasing pressure. However, a definite conclusion cannot be drawn as the experimental resolution is insufficient and the sensitivity of the Ba L_3 edge to changes in the local electronic structure of the material is limited. The use of XRS overcomes these limitations and allows for the study of the Ba $N_{4,5}$- and Si $L_{2,3}$-edge even under high pressure conditions. The close vicinity of the Ba $N_{4,5}$-edge at approx. 89 eV and the Si $L_{2,3}$-edge at approx. 100 eV allows them to be recorded in a single scan.

The Ba $N_{4,5}$- and Si $L_{2,3}$-edges were measured at high momentum transfer for pressures between $1.5 - 19.4$ GPa at the ESRF inelastic scattering beamline ID16 (compare chapter 3.2). The polycrystalline Ba_8Si_{46} sample was loaded into a panoramic DAC together with a small ruby chip for pressure calibration[44]. For the extraction of the spectra, the extraction scheme described in section 3.2 was used and only detector pixels that could be assigned to record scattering from the sample were taken into account. Remaining background scattering was removed by subtraction of a parameterized Pearson function from each data set. The scattering signals from all nine analyzer crystals were summed up such that an average momentum transfer of $q = (9.3 \pm 0.4)$ Å^{-1} was achieved. For comparison all spectra were normalized to the integrated intensity between $90 - 108$ eV energy loss. The extracted spectra are shown in Fig. 5.6 a) for the different pressures. For energy losses between 92 and 99 eV the strong Ba multiplet lines in the vicinity of the Ba $N_{4,5}$-edge can be observed whereas for energy losses above 99 eV the contribution of the Si $L_{2,3}$-edge dominates the spectra. At the high momentum transfers realized in this experiment, the GR is entirely suppressed and the non-dipole contributions to the scattering spectra allow probing also p-type uDOS which is important in view of the sp^3 covalent bonded Si cages and corresponding hybridization effects.

At a pressure of 1.5 GPa, the Ba multiplet resembles the shape of multiplet lines measured for other materials in which interaction with $4f$ states plays and important role[45], i.e. rare earth elements. The three peak structure observed in the Ba $N_{4,5}$-multiplet was also reported for the Ce^{4+} and La^{3+} $4d^{10}f^0 \rightarrow 4d^9f^1$ multiplet of CeO_2 and $LaPO_4$ by Gordon *et al.*[46]. The energy spread of the peaks is about 8 eV in Ba_8Si_{46} and thus smaller than in CeO_2, consistent with a lower nuclear charge of Ba compared to Ce which leads to

[43] Miguel, A.S. et al. (2005). *Europhys. Lett.* **69**, 556.
[44] Chervin, J.C. et al. (2001). *High Pressure Res.* **21**, 305–314.
[45] Gordon, R.A. et al. (2008). *Europhys. Lett.* **81**, 26004.
[46] Gordon, R.A. et al. (2008). *Europhys. Lett.* **81**, 26004.

a smaller multiplet splitting in Ba ($Z = 56$) than in Ce ($Z = 58$). At this low pressure the Si $L_{2,3}$-edge is featureless and directly adjacent to the high energy tail of the Ba multiplet structure.

At pressures between 3.8 and 6.2 GPa the shape of the Ba multiplet lines is somewhat broadened. This can be inferred by the vanishing of both the first feature at 92.8 eV (see dot in Fig. 5.6 a)) and the dip observed at 96.0 eV for a pressure of 4.9 GPa. A smearing of multiplet features can also be observed when comparing the reference compounds $LaPO_4$, CeO_2, and $CeRh_3$ as measured by Gordon *et al.*[47]. These reference spectra are directly compared to the Ba_8Si_{46} spectra measured at 3.8 and 4.9 GPa in Fig. 5.6 b). Apparently, a stronger covalent interaction as in $CeRh_3$ compared to CeO_2 induces a smearing of the multiplet features. Hence, an increased degree of covalent interaction between the Ba guest and Si cage atoms can be inferred for pressures between 3.8 and 6.2 GPa.

This is in line with XRD data. Yang *et al.*[48] reported a decrease in thermal parameters for the Ba atoms up to a pressure of 7 GPa as derived from Rietveld refinement. Using the same XRD data Tse *et al.*[49] found a narrowing of the peaks in the pair distribution function (PDF) assigned to the distances between Ba atoms in the large cages (Ba(L)) and between the Ba atoms and the Si atoms of the cage itself, respectively. The PDFs from Tse *et al.*[50] were obtained by a reverse Monte Carlo (RMC) simulation. The structure factor is modeled using a supercell from the replication of $8 \times 8 \times 8$ unit cells and the structural model is then refined by fitting the model structure factor to the experimental data in an iterative process. The starting atom positions were taken from the Rietveld data of Yang *et al.*[51]. The PDFs are presented in figure Fig. 5.7 showing the Ba-Ba, Ba-Si, and Si-Si distributions in part a), b), and c), respectively. The first three peaks in the Ba-Ba distance distributions (Fig. 5.7 a)) at 5.0, 5.7, and 6.3 Å are assigned to the separations between neighboring Ba(L) atoms, neighboring Ba(L) and Ba(S) sites, and the second nearest Ba(L) neighbors. The second set of peaks in the Ba-Ba correlations are assigned to the longer Ba(S)-Ba(S) distances (9.0 Å), Ba(S)-Ba(L) (9.3 Å), and Ba(L)-Ba(L) (9.7 Å) correlations. Tse *et al.*[52] assigned the Ba-Si PDF below 4 Å to two groups, the Ba(S)-Si and the Ba(L)-Si distances in the small and large cages, respectively. The sharpening in the peaks involving Ba(L) atoms from $2.4 - 6.2$ GPa is clearly visible and indicates an ordering of the Ba(L) atoms in the large Si cages. With respect to the observed smearing of the Ba multiplet features (Fig. 5.6 a)), a more centrosymmetric arrangement and less disorder of the Ba(L) atoms as observed in the PDFs, indicated by the sharpening of the Ba(L)-Si correlation, allows for a higher degree of isotropic interaction between the Ba guest and Si host atoms, thus explaining a smearing of the spectral features comparable to the trend observed for the reference compounds (Fig. 5.6 b)). Also in line with this interpretation are the findings of an optical Raman study[53]. Optical Raman shows a sharpening of spectral features assigned to localized vibrational modes of the encaged Ba(L) for pressures between 0 and 5.4 GPa also suggesting an increased ordering of Ba in the large cages. It was shown that the Ba atoms in the small

[47] Gordon, R.A. et al. (2008). *Europhys. Lett.* **81**, 26004.
[48] Yang, L. et al. (2006). *Phys. Rev. B* **74**, 245209.
[49] Tse, J.S. et al. (2011). *Phys. Rev. B* **84**, 184105.
[50] Tse, J.S. et al. (2011). *Phys. Rev. B* **84**, 184105.
[51] Yang, L. et al. (2006). *Phys. Rev. B* **74**, 245209.
[52] Tse, J.S. et al. (2011). *Phys. Rev. B* **84**, 184105.
[53] Kume, T. et al. (2003). *Phys. Rev. Lett.* **90**, 155503.

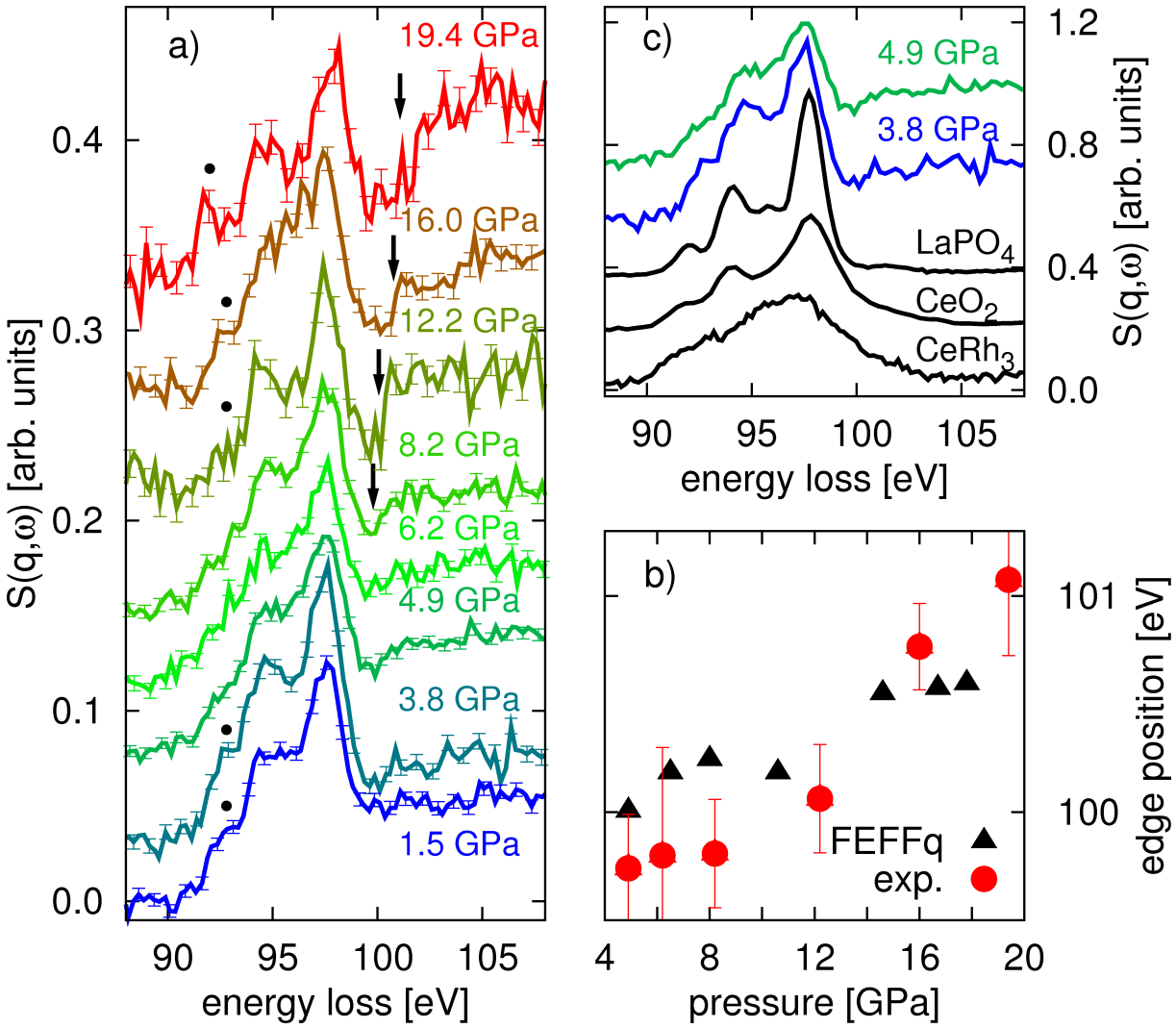

Figure 5.6: a) XRS spectra of the Ba $N_{4,5}$- and Si $L_{2,3}$-edges of Ba_8Si_{46} for pressures between $1.5 - 19.4$ GPa. The first feature of the Ba multiplet at 92.8 eV is indicated by dots, the onset of the Si $L_{2,3}$-edge is indicated by arrows. The spectra are shifted by a vertical offset for clarity. b) Comparison of spectra of Ba_8Si_{46} at 3.8 and 4.9 GPa with results for $LaPO_4$, CeO_2, and $CeRh_3$ of Gordon, R.A. et al. (2008). *Europhys. Lett.* **81**, 26004. The spectra of CeO_2 and $CeRh_3$ were shifted by -14 eV, the spectrum of $LaPO_4$ by -7.4 eV on the energy loss scale. c) Position of the Si $L_{2,3}$-edge onset as derived from a fit of a hyperbolic tangent function to the experimental data and spectra simulated using the FEFFq program package.

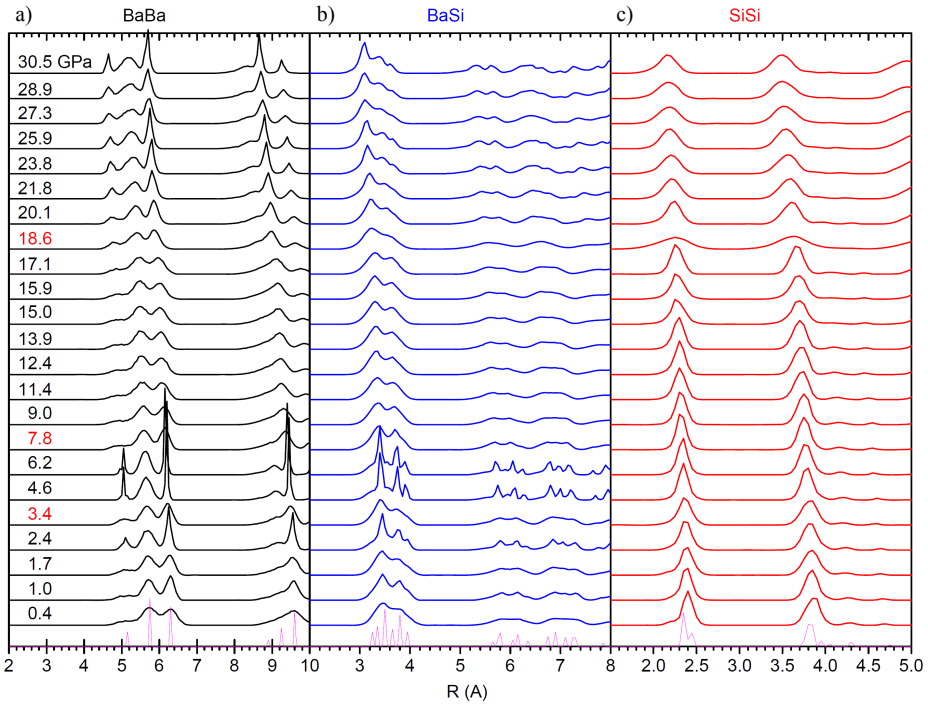

Figure 5.7: PDFs from RMC simulations of Ba_8Si_{46} for pressures between $0.4 - 30.5$ GPa. a) Ba-Ba correlations. The pressures where the phase transitions take place are highlighted in red. b) PDFs for the different Ba-Si and c) for the Si-Si correlations. The pink stick diagram at the bottom of each sub-figure corresponds to the atom separations in an ideal crystal at ambient conditions. The figure is taken from Tse, J.S. et al. (2011). *Phys. Rev. B* **84**, 184105.

cages (Ba(S)) are Raman inactive.[54]

Above 6.2 GPa, the multiplet features sharpen again and at the highest pressure of 19.4 GPa the peaks shift slightly in their energy loss position. The sharpening of the multiplet peaks indicates again a change in the interaction between the Ba guest and the Si host, where a shift in the onset of the multiplet peaks to smaller energy losses is indicative of an increase in electronic charge of the Ba atoms. The increased sharpening of the multiplet lines for pressures above 6.2 GPa again is in line with the XRD results[55] which show an increase in the thermal parameters for the Ba(L) atoms as well as a broadening of the Ba-Ba PDFs and thus an increasing disorder and/or displacement of the Ba atoms from their ideal crystallographic sites.

The Si $L_{2,3}$-edge changes most prominently for pressures above 8.2 GPa. At this pressure the edge onset starts to shift to higher energy losses and an increase in intensity compared to the multiplet features is observable. To quantify the shift in the edge onset energy, a hyperbolic tangent function was fitted to the data between 99 and 104 eV taking into account a constant background due to the high energy tail of the Ba multiplets. The results of this procedure are depicted in Fig. 5.6 c) and a sudden increase in edge position

[54] John, S. et al. (1997). *J. Phys. Chem. A* **101**, 4491–4495.
[55] Yang, L. et al. (2006). *Phys. Rev. B* **74**, 245209; Tse, J.S. et al. (2011). *Phys. Rev. B* **84**, 184105.

at ca. 12 GPa as a sign of the onset of the isostructural phase transition is clearly observable. Although the FEFFq program package is not capable of taking multiplet splitting into account and thus the modeling of the Ba multiplet features is not possible using FEFFq, a good agreement between calculation and experimental spectra of the Si $L_{2,3}$-edges was reported earlier.[56] Therefore, the Si $L_{2,3}$-edges were calculated for Ba_8Si_{46} using structural parameters from the Rietveld refinement of Yang *et al.*[57]. The edge positions of the calculated spectra are compared to the positions derived from the experiment and show a good agreement with the general trend of the experimental values. A shift of the edge onset to higher energies evidences an increased ionicity of the Si atoms. A transfer of charge from the covalent bonds to the interstitial regions was also reported for pure Si under high pressure[58] and was associated with the promotion of 3p-valence electrons into more diffuse Si 3d-orbitals. The participation of the Si 3d orbitals in chemical bonding also allows for a charge transfer from Si to the Ba atoms, slightly increasing the charge and softening the Si-Si bonds which consequently enables the homothetic volume collapse to take place[59]. This is corroborated by electron density maps of Ba_8Si_{46} as determined by Tse *et al.*[60] from high pressure XRD data using a combined Rietveld and maximum-entropy method (Rietveld/MEM) analysis. The resulting charge density maps for the (100) and (200) crystal planes are shown in Fig. 5.8. The Ba(L) atoms are in the middle of the (100) plane (5.8 a)) whereas the Ba(S) atoms can be seen in the (200) plane (5.8 b)). Systematic changes in the charge density difference contour plots are visible. At low pressure, the electron densities are mostly concentrated around the atom centers. With increasing pressure the electron density becomes more diffuse. Beyond 16 GPa, the electron density around both Ba(L) and Ba(S) atoms becomes distorted and most notably a redistribution of significant amount of electron density around the Si atoms into interstitial regions can be observed. Furthermore, there is a significant overlap between electrons of Si and both types of Ba atoms.

A total of three phase transitions is observed in Ba_8Si_{46} for pressures between 1.5 and 19.4 GPa. The first two phase transitions at 4 and 7 GPa are related to the Ba atoms trapped in the large Si_{24} cages. From ambient pressure up to 4 GPa these Ba atoms become more centrosymmetric in the large cages and occupy their ideal crystallographic positions between ca. 4 and 7 GPa. This finding is in line with results from earlier XRD studies and also gives a reasonable explanation for results from optical Raman studies. Above 7 GPa, the Ba atoms in the large cages again become distorted leading to the spectral changes observed in the presented XRS spectra and explains earlier XRD and optical Raman studies. The homothetic volume collapse between $12 - 16$ GPa is related to the Si cage atoms which are distorted while the Ba atoms remain in their crystallographic sites. A transfer of significant amount of charge from the bonding to the interstitial regions, evidenced by a shift in the Si $L_{2,3}$-edge onset, softens the Si-Si bond, and enables the collapse to take place. This is also in line with the observed shift of the Ba L_3 edge and increase of white line intensity by SanMiguel *et al.*[61].

All three phase transitions are related to changes in the electronic structure of the ma-

[56] Sternemann, H. et al. (2007*b*). *Phys. Rev. B* **75**, 075118.
[57] Yang, L. et al. (2006). *Phys. Rev. B* **74**, 245209.
[58] Tse, J.S. (2005). *Z. Kristallogr.* **220**, 521–530.
[59] Tse, J.S. (2005). *Z. Kristallogr.* **220**, 521–530.
[60] Tse, J.S. et al. (2007). *Phys. Rev. B* **76**, 174109.
[61] Miguel, A.S. et al. (2005). *Europhys. Lett.* **69**, 556.

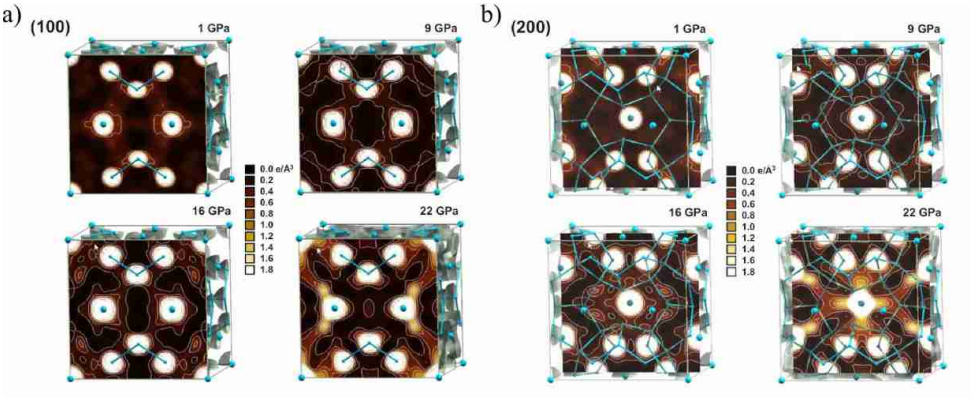

Figure 5.8: Charge density contour plots of Ba_8Si_{46} for the (100) plane (a)) and (200) crystal plane (b)) as derived from a combined Rietveld/MEM analysis of high-resolution XRD data by Tse *et al.*. Ba(L) atoms lie in the (100) plane whereas the Ba(S) atoms lie in the middle of the (200) plane. For each plane the charge density is plotted for selected pressures. For increasing pressure, a significant redistribution of electronic charge from the bonding to interstitial regions is observable. The figure is taken from Tse, J.S. et al. (2007). *Phys. Rev. B* **76**, 174109.

terial. In contrast to the experimental probes used so far, XRS provides for the first time a direct probe of the electronic structural changes across the observed phase transitions. Since these transitions originate in changes in the interaction between Ba and Si as well as in a re-hybridization of Si at elevated pressures that does not affect the crystal symmetry, these phase transitions are referred to as electron topological transitions.

5.3 Summary and outlook

The atomic and electronic structure of complex Ba intercalated Si clathrates was investigated using XRS. This unique energy loss technique enables one to study low lying absorption edges bulk sensitively even under extreme conditions such as high pressure. The momentum transfer dependence of XRS allows the choice of different excitation channels for different scattering angles.

In a first study the influence of a finite momentum transfer realized in the XRS experiments on the shape of the Ba GR was investigated. A previous study[62] showing the modulation of the Ba GR by the immediate surroundings raised the question of how a finite q value and double ionization effects influence the shape of the GR after comparing measured data with calculations employing TDLDA. Measurements of the GRs of Ba_8Si_{46} and $Ba_{24}Si_{100}$ over a large momentum transfer range show that the deviations between experiment and calculated spectra are in large part due to the finite momentum transfer in the measurements. Moreover, the presented data allows for the separation of influences of a finite momentum transfer from changes in spectral shape due to the different local Ba environments in the different clathrates. Remaining deviations between experiment

[62] Sternemann, H. (2008). *A non-resonant inelastic x-ray scattering study on silicon oxides and clathrates*. PhD Thesis, TU Dortmund.

and calculations leave little room for speculations about the influence of double electron excitations.

Similarities of the GR of Ba_8Si_{46} and $BaSi_6$ compared to the GR of $Ba_{24}Si_{100}$ suggest the origin of the GR modulations to be of structural cause and points out the influence of the direct spacial vicinity of the Ba atoms. In particular, the more complex and less symmetric surrounding of the Ba atoms in $Ba_{24}Si_{100}$ seems to be the reason for the different shape of the GR. As in the previous study the GR could be modeled within the dipole limit from first principles using the TDLDA option of the FEFF9 program package. The agreement between the calculations and the experiment is only qualitative emphasizing the need for more sophisticated theoretical models. However, the speculations about the origin of the GR modulation in a reduced symmetry around Ba atoms in open Si_{20} cages and pseudo-cubic Si_8 surroundings are supported by calculations using the FEFF program package. Likewise, a position of the Ba atoms deviating from the center of the cages influences the shape of the GR. This stresses the importance of new experiments with even higher statistical accuracy and energy resolution for the study of isolated intercalated cages to prevent interference of different environments as is the case when several unique atoms per unit cell are present.

The pressure induced phase transitions of Ba_8Si_{46} were investigated for pressures between $1.5 - 19.4$ GPa by measurements of the Ba multiplet lines in the vicinity of the Ba $N_{4,5}$-edge and the adjacent Si $L_{2,3}$-edge. In line with earlier XRD and optical Raman experiments, for the first time three electron topological transitions at 4 , 7 , and 16 GPa could be observed directly. The interpretation of the measured XRS spectra is corroborated using results from a Rietveld/MEM and/or RMC simulations and optical Raman spectroscopy.

6 XRS studies of geologically relevant materials: the case of water and silicate melts

X-ray absorption spectroscopy has proven a valuable tool to study the local atomic and electronic structure of matter, especially in disordered systems where the information drawn from other structural probes such as XRD is limited. As such, XAS has found its way into the different scientific communities from physics, chemistry, materials science, to the life- and geosciences. The following chapter will be dedicated to geoscientific questions, where XAS is widely used to study the properties of materials under conditions prevailing in the earth. In this respect, especially studies of materials under conditions comparable to those common in the earth's interior, i.e. high pressure and high temperature, are of great interest as they bear information about the earth's composition as well as the processes in the earth's interior such as heat and mass transfer. High pressure and high temperature conditions can be reached in the laboratory using DACs with resistive or laser heating and for absorption edges in the keV regime, conventional XAS can be used in both fluorescence and transmission geometry. This is possible due to the high penetration depth of hard x-rays in diamond. Conventional XAS, however, fails for elements with absorption edges in the soft x-ray regime of samples contained in diamond anvil cells and only investigations on quenched samples are possible. Light elements with absorption edges only in the soft x-ray regime like Si, Na, O, Mg, Al, and C, though, are abundant in the earth, especially in the earth's crust and mantle. In the two studies presented in this chapter, XRS is used to overcome this difficulty and the shallow absorption edges of oxygen and silicon are measured with this energy loss technique.

In a first study, the oxygen K-edge of water at elevated temperatures and pressures, especially at supercritical conditions, was measured. Changes in the shape of the O K-edge are related to structural changes in the liquid, calculations of the O K-edge from snapshots of *ab initio* molecular dynamics simulations are used to corroborate the results. This is presented in section 6.1.

In section 6.2, a second study is presented which assesses the possibility to study the influence of structural changes in silicate glasses upon intake of H_2O by monitoring the Si $L_{2,3}$-edge. The Si $L_{2,3}$-edges of different Si bearing minerals and glasses are compared and a first *in situ* study of a silicate melt at high temperature and high pressure conditions is presented. The results are compared to calculations of the Si $L_{2,3}$-edge using FEFFq. Implications for future experiments are given.

6.1 Water at high temperature and high pressure

Water is one of the most fascinating substances and one of the most widely studied systems in condensed matter physics.[1] It is the most important solvent of the earth and exhibits a rich phase diagram. Besides abundant ice phases[2] water shows a remarkable complexity over a large p-T range also in the liquid state which gives rise to speculations about different liquid phases.[3] This was resolved by a vast number of investigations of the atomic and electronic structure of water under extreme conditions, covering the ice phases, supercooled water, and water in confinement and/or within hydration layers at interfaces[4]. Spectroscopic investigations, in particular using XRS, have complemented investigations using x-ray and neutron diffraction.[5]

Due to the experimental difficulties, water under supercritical conditions has only scarcely been subject of detailed spectroscopic investigations so far. The p-T regime of supercritical water, however, is especially interesting for geoscientists since water plays a key role in heat and mass transfer as well as element fractionation processes in the earth's lithosphere, such as volcanism and ore deposit formation.[6] Geochemical processes and reactions like the formation of petroleum[7] and even contributions to the origin of life[8] have been linked to the high temperature and high pressure properties of water. The polar character of the H_2O molecule and the tendency to dissociate makes it a more powerful solvent than other volatiles. This is also taken advantage of in chemical processing, where supercritical water is used as a reaction medium for chemical and materials synthesis, waste destruction, plastics recycling, and biomass processing.[9] These solvent properties of H_2O do not only depend on density and dissociation, but also on structural parameters which are poorly understood especially at the supercritical conditions prevalent in the earth's interior. Soper[10] reported a huge degree of disorder with a largely broken hydrogen-bond (H-bond) network in supercritical water. On the other hand, optical Raman spectra of water suggest that a significant fraction of network water is still present even at high temperatures, pressures, and solute concentrations.[11] Based on XRS measure-

---

1 Debenedetti, P.G. (1996). *Metastable liquids: concepts and principles*. Princeton Univ Press; Ball, P. and Stillinger, F.H. (1999). *Nature* **401**, 850–850; Ball, P. (2000). *A Biography of Water: Life's Matrix*. New York: Farrar, Straus and Giroux; Ball, P. (2008). *Nature* **452**, 291–292.

2 Petrenko, V.F. and Whitworth, R.W. (1999). *Physics of ice*. Oxford University Press.

3 Debenedetti, P.G. (2003). *J. Phys.: Condens. Matter* **15**, R1669; Soper, A.K. et al. (2010). *Proc. Nat. Acad. Sci.* **107**, E44.

4 Israelachvili, J. and Wennerström, H. (1996). *Nature* **379**, 219–225; Rasaiah, J.C. et al. (2008). *Annu. Rev. Phys. Chem.* **59**, 713–740.

5 Bergmann, U. et al. (2002). *Phys. Rev. B* **66**, 092107; Bergmann, U. et al. (2007*b*). *J. Chem. Phys.* **127**, 174504; Bergmann, U. et al. (2007*a*). *Phys. Rev. B* **76**, 024202; Cai, Y.Q. et al. (2005). *Phys. Rev. Lett.* **94**, 25502; Fukui, H. et al. (2007). *J. Chem. Phys.* **127**, 134502; Tse, J.S. et al. (2008). *Phys. Rev. Lett.* **100**, 95502; Huang, C. et al. (2009). *Proc. Natl. Acad. Sci.* **106**, 15214; Pylkkänen, T. et al. (2010). *J. Phys. Chem. B* **114**, 3804–3808; Nilsson, A. et al. (2010). *J. Electron. Spectrosc. Relat. Phenom.* **177**, 99–129.

6 Keppler, H. (1996). *Nature* **380**, 237–240; Manning, C.E. (2004). *Earth. Planet. Sci. Lett.* **223**, 1–16.

7 Siskin, M. and Katritzky, A.R. (1991). *Science* **254**, 231.

8 Huber, C. and Wächtershäuser, G. (1997). *Science* **276**, 245.

9 Shaw, R.W. et al. (1991). *Chem. Eng. News* **69**, 26–39; Akiya, N. and Savage, P.E. (2002). *Chem. Rev.* **102**, 2725–2750.

10 Soper, A.K. (2000). *Chem. Phys.* **258**, 121–137.

11 Schmidt, C. and Watenphul, A. (2010). *Geochim. Cosmochim. Acta* **74**, 6852–6866.

ments Wernet *et al.*[12] proposed supercritical water to consist of small H-bonded patches surrounded by less dense non-H-bonded regions in line with local density inhomogeneities revealed by small angle x-ray and neutron scattering.[13]

Here, a resistively heated HDAC[14] is used to produce high pressure and high temperature conditions. A schematic drawing of the HDAC is given in Fig. 6.1. A recess hole in the culet of the lower diamond minimizes the length of the x-ray path through the diamond. With a recess hole of 500 µm diameter and depth of 150 µm in the center of a 1000 µm culet an average of approx. 325 µm diamond material remains for each the incoming and scattered x-ray beam. The sample in the HDAC can be monitored optically using a camera and lens system. A series of images of the sample in the vicinity of the homogenization temperature is shown in the right part of Fig. 6.1. A vapor bubble, clearly visible at room temperature, dissolves between $160 - 163$ °C. Using this homogenization temperature, the volume of the sample, and the equation of state after Wagner and Pruß[15] the pressure of the sample can be evaluated.[16] This is of great advantage over other used techniques[17] since it not only allows for an accurate determination of the sample's pressure and/or density but also allows the sample to be monitored during the experiment. The experiments were carried out using a Rh gasket. Milli-q water was used in all experiments. All measurements were conducted at an average momentum transfer of $q = (2.9 \pm 0.4)$ Å^{-1} corresponding to an average scattering angle of $2\theta = 30°$ and an analyzer energy of 9.7 keV. A total energy resolution of 0.8eV was achieved. Signals from all nine analyzer crystals from the multi analyzer crystal spectrometer of the inelastic scattering beamline ID16 (compare section 3.2) were averaged. All spectra were normalized in the energy loss range between $532 - 546$ eV.

The well known water phase diagram is depicted in Fig. 6.2. The experimental pressure and temperature values are indicated by red stars in the figure. The resulting spectra are shown in Fig. 6.3. Spectra taken along the vapor pressure curve are shown in part a) of the figure. The spectrum at ambient conditions shows a shoulder at 535 eV energy loss, usually referred to as the pre-edge (see Fig. 6.3 a)), is dominated by a broad maximum at 538 eV energy loss, the main-edge, and significant intensity up to energy losses of 544 eV. The high energy region of the near edge structure will be referred to as the post-edge (see Fig. 6.3 a)). With increasing temperature and pressure the pre- and main-edge gain spectral weight and shift considerably towards smaller energy losses whereas the post-edge loses intensity. Fig. 6.3 b) shows the influence of the water pressure and thus density on the K-edge spectrum of water at $T = 400$ °C. A clear drop in intensity in the pre-edge regime is visible for the spectrum measured at 503 MPa/0.93 g/cm^3 as compared to the one at 54 MPa/0.54 g/cm^3. The spectrum of the sample at ambient temperature and

[12] Wernet, P. et al. (2005). *J. Chem. Phys.* **123**, 154503.

[13] Morita, T. et al. (2000). *J. Chem. Phys.* **112**, 4203; Sedlmeier, F. et al. (2011). *J. Am. Chem. Soc.* **133**, 1391–1398.

[14] Bassett, W.A. (2003). *Eur. J. Mineral.* **15**, 773; Schmidt, C. and Rickers, K. (2003). *Am. Mineral.* **88**, 288.

[15] Wagner, W. and Pruß, A. (1999). *J. Phys. Chem. Ref. Data* **31**, 387.

[16] The parametrical solutions to the equation of state after Wagner and Pruß (Wagner, W. and Pruß, A. (1999). *J. Phys. Chem. Ref. Data* **31**, 387) are illustrated for temperatures up to 900 °C and 1500 MPa in appendix 7, taken from C. Schmidt, private communications. The melting curves of the ice phases are taken from Wagner, W. et al. (1994). *J. Phys. Chem. Ref. Data* **23**, 515–528.

[17] E.g. Wernet, P. et al. (2005). *J. Chem. Phys.* **123**, 154503 used the temperature in combination with an estimate of the water density by x-ray absorbance.

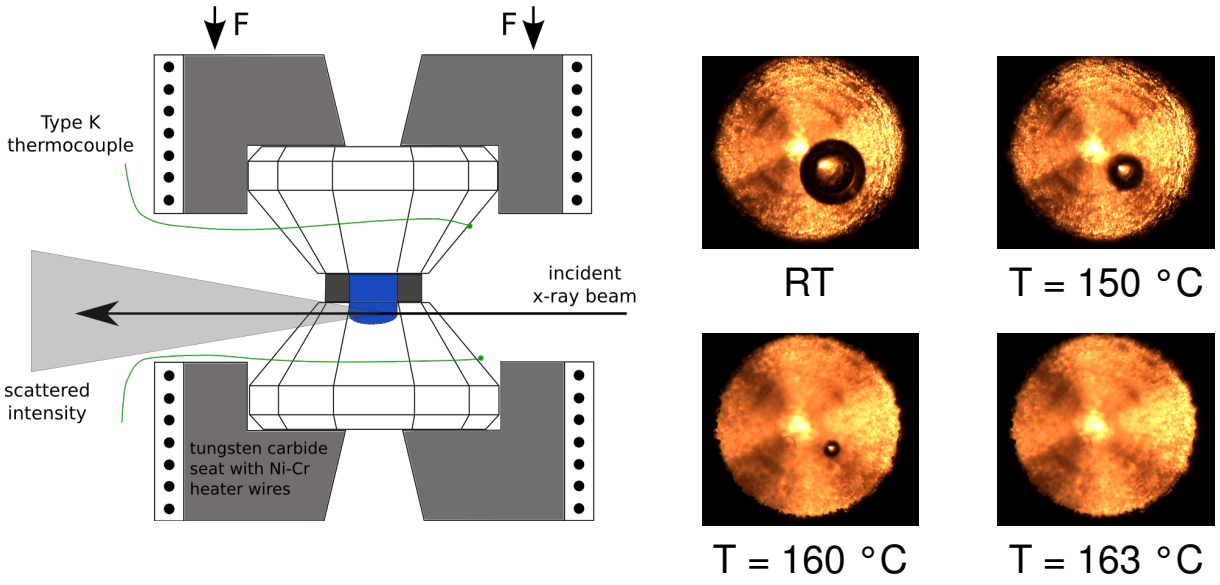

Figure 6.1: Left: Schematic drawing of the HDAC used. The lower diamond has a recess hole in its culet in order to minimize the length of the beam-path through the diamond. The seats of the diamonds are heated resistively and the temperature is monitored by two thermocouples mounted onto the diamonds as close to the sample as possible. Right: Series of images taken using a camera and lens system which is mounted on top of the HDAC and a light source which is mounted below the HDAC. A vapor bubble, clearly visible at room temperature, dissolves between 160-163°C.

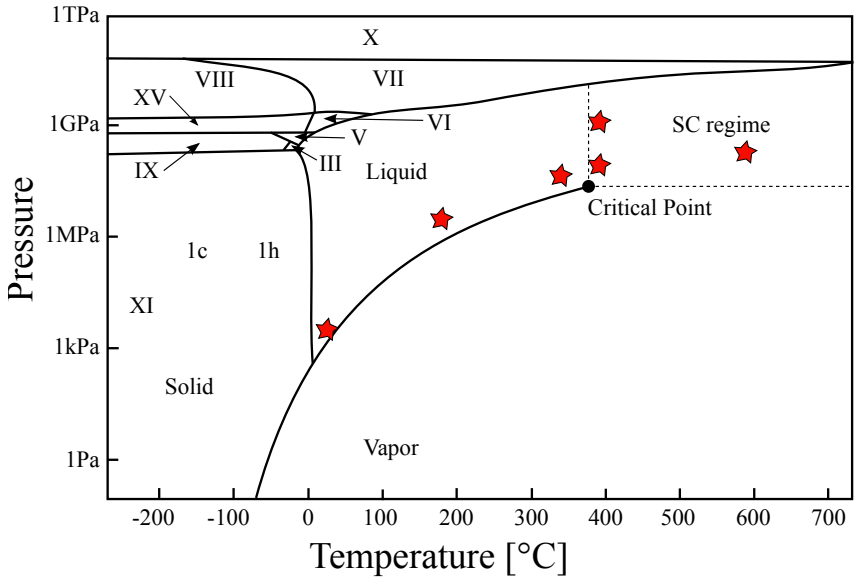

Figure 6.2: The phase diagram of water. Roman letters indicate the different ice phases. Measurements were conducted along the vapor pressure curve and in the supercritical regime (SC regime). The approximate p and T values that were measured are indicated by red stars.

pressure is also shown as reference. This trend is also observable in Fig. 6.3 a) when the spectrum of the 400 °C sample is compared to the spectrum measured at 370 °C. Thus, increasing the density of the water sample results in a drop in pre- and main-edge intensity.

Wernet *et al.*[18] assigned the spectral features as follows. The prominent post-edge feature in ambient water is due to the formation of an extended H-bonded water network. This was deduced by comparison of water spectra to those of ice[19] showing an even more pronounced post-edge which was linked to the perfect tetrahedral H-bonded H_2O molecule network in the crystalline phase. A greater degree of order results in a more pronounced post-edge as compared to the main-edge intensity. Wernet *et al.* assigned the pre-edge peak at 535 eV to contributions from H_2O molecules with a broken or weakened donor H-bond[20], i.e. weakened or broken O–H$\cdots$O bond, which was motivated by comparison of the bulk water spectrum with a spectrum of a water surface. The O K-edge spectrum of water in the gas phase is dominated by two main transitions at 534 and 536 eV in the pre-edge region stemming from excitations into the O-H anti-bonding $4a_1$ and $2b_1$ orbitals, respectively.[21] It should be noted at this point that the assignment of spectral features is strongly debated in the scientific community.[22] In particular, a consensus on the origin of the pre-edge feature in the O K-edge of water is far from being reached. Tse *et al.*[23] assigned the pre-edge to a core-excitonic feature and did not observe a systematic depen-

[18] Wernet, P. et al. (2004). *Science* **304**, 995; Wernet, P. et al. (2005). *J. Chem. Phys.* **123**, 154503.
[19] Wernet, P. et al. (2004). *Science* **304**, 995.
[20] Wernet, P. et al. (2005). *J. Chem. Phys.* **123**, 154503.
[21] Myneni, S. et al. (2002). *J. Phys.: Cond. Matter* **14**, L213.
[22] Nilsson, A. et al. (2010). *J. Electron. Spectrosc. Relat. Phenom.* **177**, 99–129.
[23] Tse, J.S. et al. (2008). *Phys. Rev. Lett.* **100**, 95502.

dence of the pre-edge intensity with the H-bond characteristics. Pylkkänen *et al.*[24] found a dependence of pre-edge intensity and position on the non-H-bonded oxygen neighbors by studying the O K-edge of different ice phases.

The experimental finding for supercritical water at 380 °C, 30 MPa, and 0.54 g/cm^3 of Wernet *et al.*[25] is shown in Fig. 6.3 d) (solid green line). A prominent pre-edge at 534 eV energy loss and shoulder at 536 eV, corresponding to the excitation energies of the $4a_1$ and $2b_1$ anti-bonding orbitals in the gas phase, as well as significant intensities in the post-edge region around 544 eV, interpreted as due to a significant amount of H-bonded molecules (*vide supra*), lead the authors to propose supercritical water to consist of small H-bonded patches surrounded by less dense non-H-bonded regions. This was underlined by a simulated spectrum of randomly oriented non-H-bonded H_2O molecules with an intermolecular distance corresponding to the experimental density (O-O distance 3.9 Å) which shows peaks only at the position of the $4a_1$ and $2b_1$ anti-bonding orbitals and little intensity in the post-edge region (red curve in Fig. 6.3 d)). A fit of a superposition of the gas phase spectrum and the bulk water spectrum to the spectrum of supercritical water lead Wernet *et al.*[26] to propose that approx. 35% of the water molecules in supercritical water have two or fewer H-bonds.

Utilizing this train of thoughts to interpret the presented experimental findings leads to conclude that the extended H-bonded network persistent in ambient water, evidenced by the prominent post-edge, is increasingly distorted and broken as the temperature and pressure increase along the vapor pressure line. This is connoted by a systematic decrease of the post-edge and increase as well as shift of the pre- and main-edge towards the peaks found in the gas phase. A significant amount of tetrahedral H-bonding even above the critical point such as Wernet *et al.*[27] found in their study cannot be identified as a prominent post-edge is not present in the measured data. However, a certain degree of H-bonding persists even at the highest temperatures and pressures as the spectra still significantly differ from the gas phase spectrum in line with recent optical Raman data of the OH stretching modes in different aqueous solutions at high T and p that show bands assigned to network components even at 600 °C and 920 MPa.[28]

The effect of pressure can be studied when comparing spectra recorded at 400 °C and 54 and 503 MPa, respectively. A reversal effect can be observed: the pre- and main-edge lose spectral weight and shift to higher energy losses, whereas the post-edge gains spectral weight at approx. 544 eV. As mentioned earlier, this can also be observed when comparing the spectra measured at 370 and 400 °C and densities of 0.45 and 0.54 g/cm^3, respectively.

Nilsson *et al.*[29] used the "bond-length-with-a-ruler" model, introduced by Stöhr[30], to explain a shift of the post-edge position towards smaller energies with an increasing O-O distance. They assigned the post-edge to a shape resonance similar to those found in molecules like N_2, O_2, CO, C_2H_2, C_2H_4, etc. for which the energy position depends on the bonding-anti-bonding molecular orbital splitting that in turn is depending on the

[24] Pylkkänen, T. et al. (2010). *J. Phys. Chem. B* **114**, 3804–3808.
[25] Wernet, P. et al. (2005). *J. Chem. Phys.* **123**, 154503.
[26] Wernet, P. et al. (2005). *J. Chem. Phys.* **123**, 154503.
[27] Wernet, P. et al. (2005). *J. Chem. Phys.* **123**, 154503.
[28] Schmidt, C. and Watenphul, A. (2010). *Geochim. Cosmochim. Acta* **74**, 6852–6866.
[29] Nilsson, A. et al. (2010). *J. Electron. Spectrosc. Relat. Phenom.* **177**, 99–129.
[30] Stöhr, J. (1992). *NEXAFS Spectroscopy*. Vol. 222238. Springer Berlin.

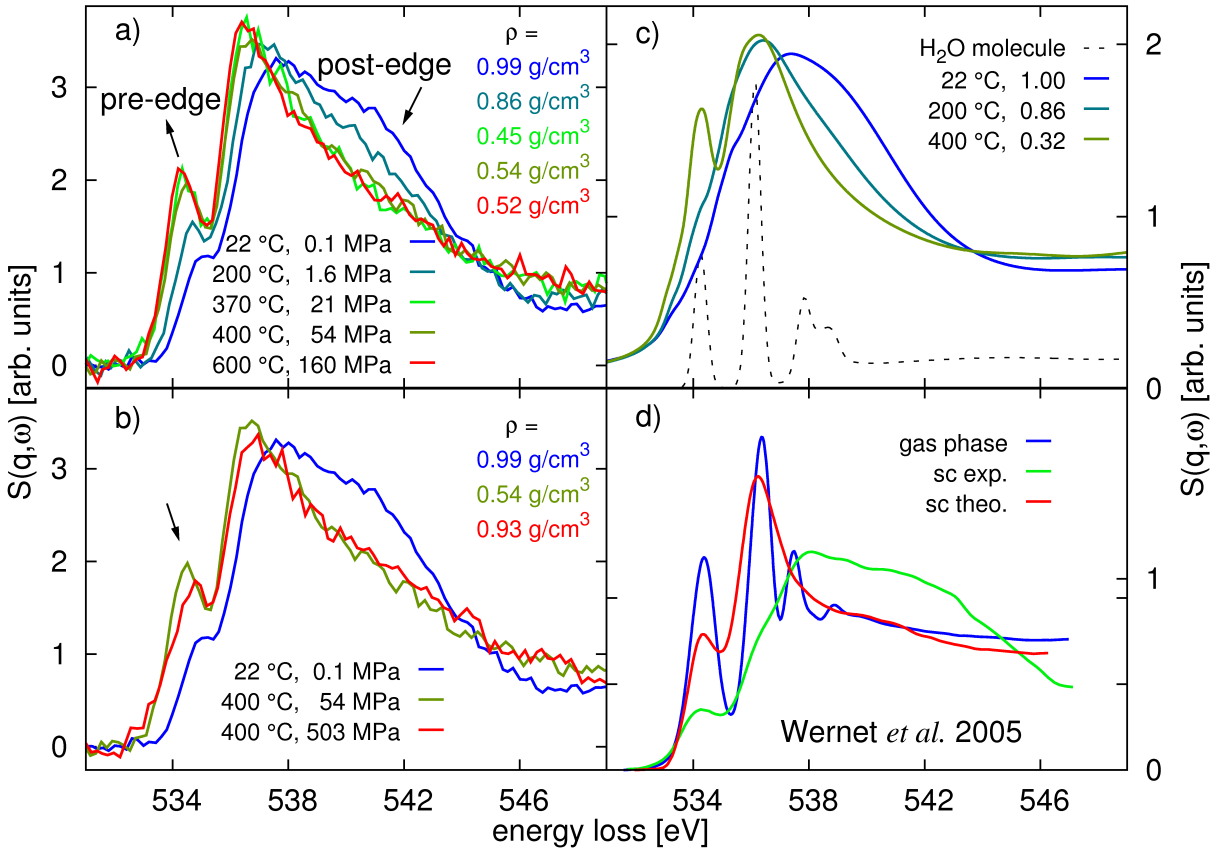

Figure 6.3: Experimental results showing XRS spectra at the O K-edge of water under high pressure and high temperature conditions. a) XRS spectra of water measured along the vapor pressure line. Spectral changes are obvious in both the pre-edge and post-edge region. b) Oxygen K-edge of water at ambient conditions and at T = 400 °C at two different pressures. The water densities are indicated in the same color code as the according spectra. c) Simulated spectra for similar conditions as in the experiment as well as a simulated spectrum of a single H_2O molecule. d) Experimental data of a gas phase and supercritical water spectrum as well as a simulation of randomly oriented water molecules all taken from Wernet, P. et al. (2005). *J. Chem. Phys.* **123**, 154503.

bond distance. The fact that the observed shift depends linearly on the change in bond distance gives this concept its name. An example of a linear relation between oxygen-oxygen distance and position of the shape resonance is given by Sette *et al.*[31] for O_2 adsorbed on Pt(111). A linear shift of the post-edge position towards smaller energies was observed in calculated spectra of ice for different donating H-bond oxygen-oxygen distances[32].

Regarding the experimental findings, the drop in post-edge intensity and gain as well as shift of main-edge intensity could also be explained using the bond-length-with-a-ruler concept. As the density decreases with increasing temperature and pressure up to 400 °C the oxygen-oxygen distance increases resulting in a shift of the post-edge feature to lower energy losses until it coincides with the main-edge, thus increasing it. However, since for the highest temperature (600 °C) water spectrum, the density of the sample is close to the preceding 400 °C sample, this concept implies that the temperature induced fluctuations in the sample at this temperature result in an average oxygen-oxygen distance that is slightly higher than the bond length in the preceding water samples. Isothermal compression (see Fig. 6.3 b)) results in an opposite trend, i.e. a shortening of the oxygen-oxygen distances, and a reversal effect is observed in line with the bond-length-with-a-ruler concept.

In order to elaborate these findings and tentative interpretations, the experimental data are compared to calculations of the O K-edge within KS-DFT using the StoBe-deMon program package and the framework of Sakko *et al.*[33] as described in section 2.2.3. The atomic structures were taken from snapshots of *ab initio* MD[34] simulations.[35]

Using the periodic boundary conditions of the MD simulation, clusters of radius between $8 - 11$ Å were cut out around each of the 64 oxygen atoms resulting in atomic clusters of approx. 60–70 H_2O molecules. The O K-edge was calculated for the central O atom of each of the 64 clusters using LDA. The resulting stick spectra were broadened by Gaussians of line width 0.6 eV below 532 eV energy loss and 6.0 eV width above 545 eV energy loss. Between 532 and 545 eV the line width was increased linearly.[36] A rigid shift of 3.4 eV on the energy loss scale was applied to coincide the edge onset of the calculated spectra with the experimental edge onset. From the limited number of water molecules in the MD simulation box it is obvious that long range fluctuations as expected to occur in the supercritical regime are not accounted for. However, since the measured absorption edges are inherently sensitive to the local environment of the absorbing atom, this approach is justified. The use of snapshots for simulating the spectra is further justified, because the time scale of the photoabsorption process is much faster than any H-bond dynamics[37] which implies that on its time scale the photoelectron probes a more or less frozen snapshot of the local environment. Vibrational effects can, in principle, be accounted for via the Franck-Condon principle.[38]

The simulated spectra are shown in Fig. 6.3 c). Although the pre-edge is underesti-

[31] Sette, F. et al. (1984). *J. Chem. Phys.* **81**, 4906.
[32] Odelius, M. et al. (2006). *Phys. Rev. B* **73**, 024205.
[33] Sakko, A. et al. (2007). *Phys. Rev. B* **76**, 205115.
[34] Car, R. and Parrinello, M. (1985). *Phys. Rev. Lett.* **55**, 2471–2474.
[35] All MD simulations were carried out by Dr. Sandro Jahn of the GFZ Potsdam, Potsdam, Germany.
[36] Leetmaa, M. et al. (2010). *J. Electron. Spectrosc. Relat. Phenom.* **177**, 135–157.
[37] Nibbering, E.T.J. and Elsaesser, T. (2004). *Chem. Rev.* **104**, 1887–1914.
[38] Sakko, A. et al. (2011). *Phys. Chem. Chem. Phys.* **13**, 11678–11685.

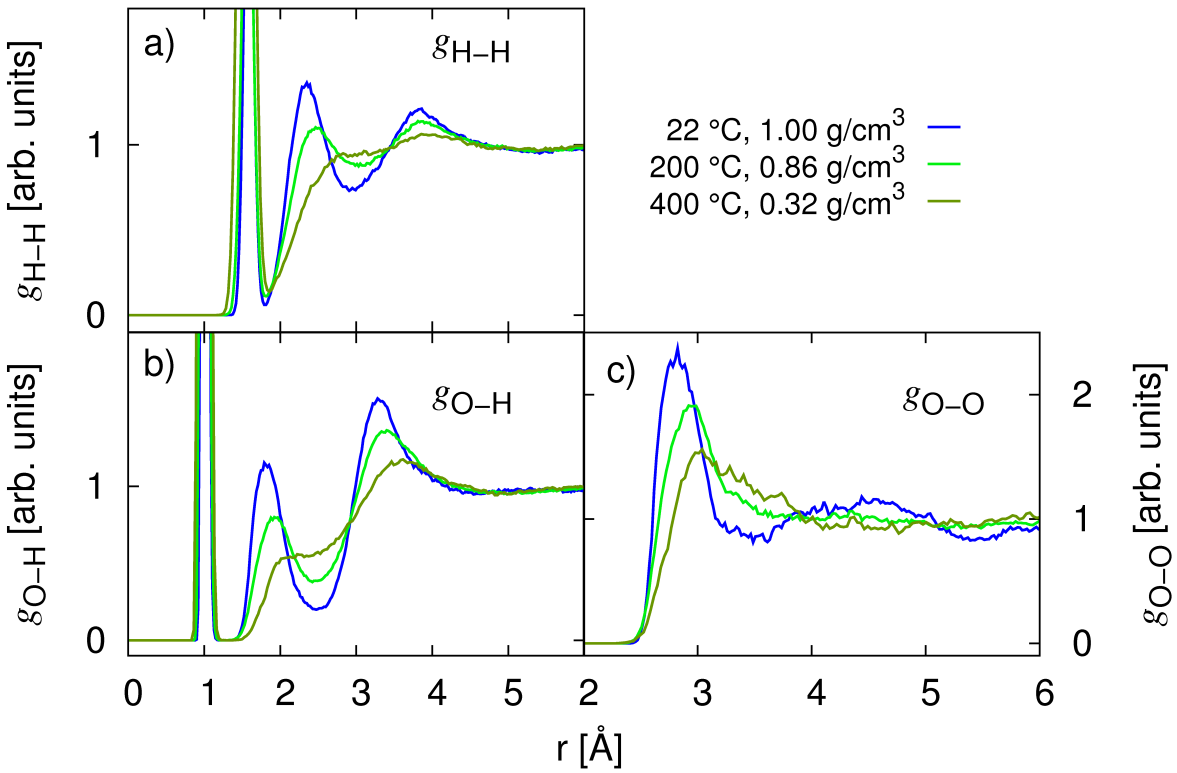

Figure 6.4: Radial distribution functions extracted from the *ab initio* MD simulations for a) the O-H coordination, b) H-H coordination, and c) O-O coordination for the different simulated structures. The MD simulations as well as the extraction of the radial distribution functions was carried out by Dr. Sandro Jahn from the GFZ, Potsdam, Germany.

mated for 22 °C and 200 °C, the overall agreement between experiment and simulation is remarkable. With increasing temperature the post-edge loses intensity systematically and the two highest temperature spectra coincide in this energy range. A shift and increasing sharpness in main-edge intensity can also be observed. Simulating the pre-edge is a formidable task[39] and agreement between experiment and simulation is not as good as for the other spectral features. However, a systematic increase and shift in pre-edge intensity from $22 - 400$ °C can be observed analogous to the experimental data. The overall accordance of the simulated and measured spectra suggest that structural information from the MD simulation can be used to explain the experimental findings. Structural information from the MD simulations are most easily represented by the partial radial distribution functions (RDF) $g_{\mathrm{O-O}}$, $g_{\mathrm{O-H}}$, and $g_{\mathrm{H-H}}$ shown in Fig. 6.4.[40] At ambient conditions, all partial RDFs exhibit a pronounced multi-peak structure evidencing the network structure of RT water. With increasing temperature this multi-peak structure smears out. In particular, a systematic shift of the peaks towards longer correlation lengths is visible up to $T = 400$ °C. A large degree of H-bond breaking and weakening can also be observed with increasing temperature. The first non-intra-molecular peak in the $g_{\mathrm{O-H}}$ RDF, i.e. the peak at 1.8 Å, often associated with H-bonding, shifts to higher distances and loses considerable intensity. These observations are in line with the formation of a pronounced pre- and main-edge in the XRS data and a local structure of water at these high T and p conditions of a largely H-bond disrupted arrangement of H_2O molecules with a high degree of fluctuations. Clear inhomogeneities as reported earlier[41] cannot be deduced from the presented data.

To further the understanding of the structural changes in the water network induced by the solution of ions, the measurements at RT, 200°C, and 400 °C were repeated in a first test experiment on 4.4molal aqueous solutions of HCl. The resulting spectra are shown in Fig. 6.5 a). Throughout the entire temperature and pressure regime, the solvation of HCl seems to have a reversal effect compared to the application of T and p. The pre- and main-edge lose spectral weight whereas the post-edge region increases slightly. Nilsson *et al.*[42] discussed the effect of HCl solution in terms of the bond-length-with-a-ruler concept. For HCl concentrations above 4 molal the so called Eigen structural motif (H_3O^+) dominates which has a smaller H-bond length than the Zundel motif ($H_5O_2^+$) and thus exhibits a higher post-edge energy position. The effect of HCl solvation on the oxygen K-edge of water is very similar to the effect observed for an increase in pressure (shown again in Fig. 6.5 b)). Ion induced changes in the water structure similar to the influence of pressure were found before by Leberman *et al.*[43] who used neutron scattering to study the influence of salts on the local structure of water. For a more detailed analysis of the structural changes, a comparison to calculated spectra from MD simulation snapshots is highly desirable.

The oxygen K-edge of water under ambient as well as high pressure and high temperature conditions was measured by XRS using a HDAC. The extended H-bonded network

[39] Leetmaa, M. et al. (2010). *J. Electron. Spectrosc. Relat. Phenom.* **177**, 135–157; Nilsson, A. et al. (2010). *J. Electron. Spectrosc. Relat. Phenom.* **177**, 99–129.

[40] The radial distribution functions were extracted from the MD trajectories by Dr. Sandro Jahn, GFZ Potsdam, Potsdam, Germany.

[41] Wernet, P. et al. (2005). *J. Chem. Phys.* **123**, 154503.

[42] Nilsson, A. et al. (2010). *J. Electron. Spectrosc. Relat. Phenom.* **177**, 99–129.

[43] Leberman, R. and Soper, A.K. (1995). *Nature* **378**, 364–366.

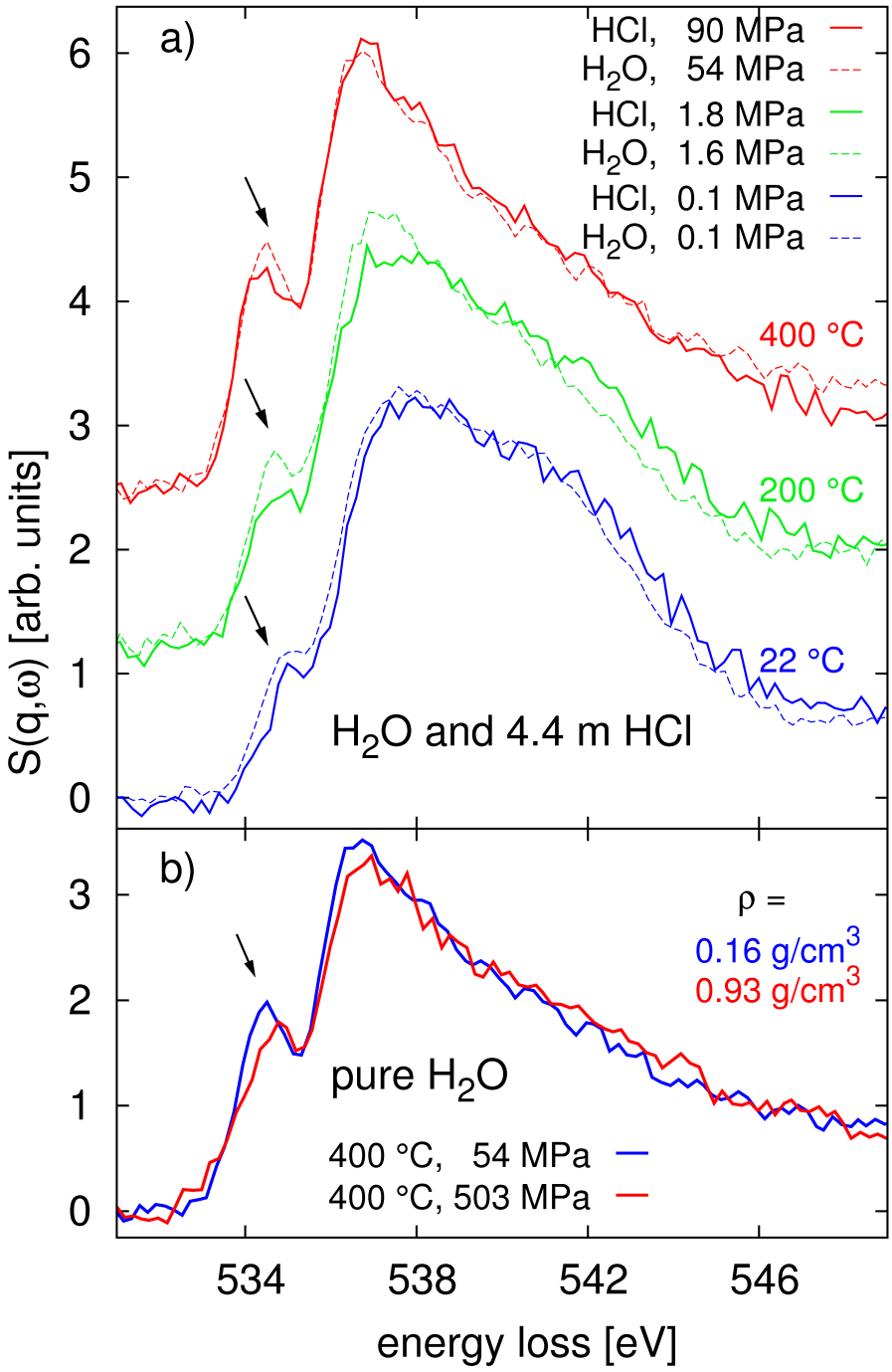

Figure 6.5: a) XRS spectra of 4.4 molal aqueous HCl solutions for different temperatures and pressures compared to the pure water spectra at similar conditions. The drop in pre-edge intensity is indicated by an arrow. A more pronounced post-edge is evident for the RT and 200 °C data. b) XRS spectra of pure water at 400 °C for two different pressures for the sake of comparison to the effect of HCl solvation.

structure prevalent in ambient water is found to be more and more disrupted as temperature and pressure increase. A model of an inhomogeneous water structure, i.e. patches of higher density water surrounded by regions of lower density, as reported earlier[44] is not supported by the experimental findings. Spectra calculated within DFT in TPA from MD simulation snapshots reproduce the experimental findings and corroborate the interpretation. First measurements of aqueous HCl solutions under the influence of temperature and pressure reveal that the influence of ion solvation on the local water structure is similar to the application of pressure in the pure water phase, in line with previous neutron scattering experiments.

6.2 Silicate melt NS3 at high temperature and high pressure

Silicon is the most abundant metalloid of the earth. Especially in the earth's crust and mantle, Si is one of the most common elements. However, it rarely occurs as elemental Si and is usually found as an anion in one of the many silicate minerals which constitute approx. 90% of the earth's crust and a large fraction of the earth's mantle. Thus, it is the chemical and physical properties of these minerals and their melts under the high pressures and temperatures prevailing in the lithosphere and asthenosphere which largely govern the geological processes like heat and mass transfer in the earth's interior. These processes are inherently linked to plate tectonics, magmatism, and vulcanism and thus have affected the history and shape of the earth.

This section is dedicated to the study of structural changes of silicates inferred by the dissolution of water at high pressure and high temperature. The understanding of these structural changes may provide a deeper insight into the relation between the structure of hydrous melts and their physical properties. Especially in the vicinity of subduction zones, the downwelling plates can take large volumes of water into the mantle, where it can be taken up in substantial amounts by silicate melts, particularly at high pressure. The dissolution of water in the silicate melts was shown to have a strong influence on physical and transport properties[45] but the inferred structural changes accompanied with the intake of H_2O are still vividly debated.[46]

Soft x-ray absorption spectroscopy was used to study changes in the coordination environment of Si, Al, and Na in hydrous glasses[47]. Direct conclusions with regard to the melt structure, however, are difficult owing to the low bulk sensitivity of soft XAS and the problematics of quenching H_2O-bearing melts[48].

As mentioned in the previous chapters and sections, XRS overcomes the difficulties inherent to soft XAS of samples contained in complicated sample environments like DACs and thus makes the *in situ* study of hydrous silicate melts possible. To assess the feasibility

[44] Wernet, P. et al. (2005). *J. Chem. Phys.* **123**, 154503.

[45] Mysen, B.O. and Richet, P. (2005). *Silicate glasses and melts: Properties and structure.* Vol. 10.

[46] Kohn, S.C. et al. (1989). *Geochim. et Cosmochim. Acta* **53**, 2925–2935; Kümmerlen, J. et al. (1992). *J. Phys. Chem.* **96**, 6405–6410; Nowak, M. and Behrens, H. (1995). *Geochim. et Cosmochim. Acta* **59**, 3445–3450; Schmidt, B.C. et al. (2000). *Geochim. et Cosmochim. Acta* **64**, 513–526.

[47] Farges, F. et al. (2007). *AIP Conf. Proc.* **882**, 214–216.

[48] De Wispelaere, S. et al. (2004). *Chem. Geol.* **213**, 63–70; Nowak, M. and Behrens, H. (1995). *Geochim. et Cosmochim. Acta* **59**, 3445–3450.

of an *in situ* study of silicate melts, the Si $L_{2,3}$-edge in different Si containing quenched glasses and minerals was measured and a first investigation of the Si $L_{2,3}$-edge of a hydrous silicate melt under high temperature and high pressure conditions was conducted. The measurements were carried out using the multi-analyzer spectrometer at the inelastic scattering beamline ID16 of the ESRF. The Si(880) analyzer reflection at 12.92 keV was used and averaging over all nine analyzers resulted in an average momentum transfer of $q = (12.1 \pm 0.2)$ Å^{-1}. This corresponds to an average scattering angle of 135°. The overall energy resolution was 2.5 eV. All spectra were normalized to the integrated intensity between $100 - 130$ eV energy loss.

The results of the *ex situ* measurements are depicted in Fig. 6.6 a) showing the Si $L_{2,3}$-edges of water bearing and water free glassy NS3 ($Na_2Si_3O_7$) and Albite ($NaAlSi_3O_8$) samples as well as of a crystalline Albite sample. Changes in the shape of the absorption edges are rather small. The maximum at approx. 130 eV energy loss has a bimodal shape for the crystalline Albite sample (see arrows in the figure) which is smeared out for the glassy samples. This maximum is broad for the glassy NS3 samples and asymmetric for the glassy Albite samples. A small shift in the position of the second maximum at approx. 130 eV energy loss to smaller values might be present for the Albite samples when compared to the NS3 samples. A shoulder on the high energy side of the white line may be present in the water free glass samples but not in the water free glasses (indicated by an arrow). These small spactral differences are in line with the findings of Farges *et al.*[49].

A first *in situ* measurement of the Si $L_{2,3}$-edge of a hydrous silicate melt at $T = 600$ °C and a pressure of $p \approx 230$ MPa is shown in Fig. 6.6 b). For this measurement, a small glass piece was loaded into a HDAC together with Milli-q water. The HDAC was heated resistively and the pressure of the fluid increases approximately along an isochore resulting in a water saturated melt. The fluid pressure and density are calculated using the homogenization temperature of the aqueous fluid after the run using an appropriate equation of state.[50]

Differences between the spectrum of the *in situ* sample and the spectra of the glassy and crystalline reference samples are hardly visible. As in the reference glasses, a white line at approx. 108 eV energy loss and a broad maximum around 130 eV energy loss are the most prominent features. The similarity between the *in situ* and reference spectra may be explained by the rigid Si-O bond which leaves the direct vicinity of the Si atoms in the different samples almost unchanged, i.e. tetrahedrally coordinated by oxygen atoms. The considerable noise level in the *in situ* data as well as the limited number of data points far above the edge onset complicate the data treatment and proper background subtraction.

In order to evaluate a possible procedure of comparing calculated spectra with experimental data, similar to the case of liquid water as presented in section 6.1, the Si $L_{2,3}$ and Na K-edges of crystalline NS3 and Albite were calculated using the FEFFq program package. The results are presented in Fig. 6.7 a). Each edge was calculated for all non-equivalent atoms in the unit cell and the resulting spectra were averaged taking

[49] Farges, F. et al. (2007). *AIP Conf. Proc.* **882**, 214–216.

[50] The pressure was estimated by Dr. Christian Schmidt, GFZ Potsdam, Potsdam, Germany, using the equation of state after Wagner and Pruß (Wagner, W. and Pruß, A. (1999). *J. Phys. Chem. Ref. Data* **31**, 387) for H_2O, this is, although underestimating the actual pressure at pressures above 1.0 GPa, the most reliable pressure calibration. C. Schmidt, private communications (2011).

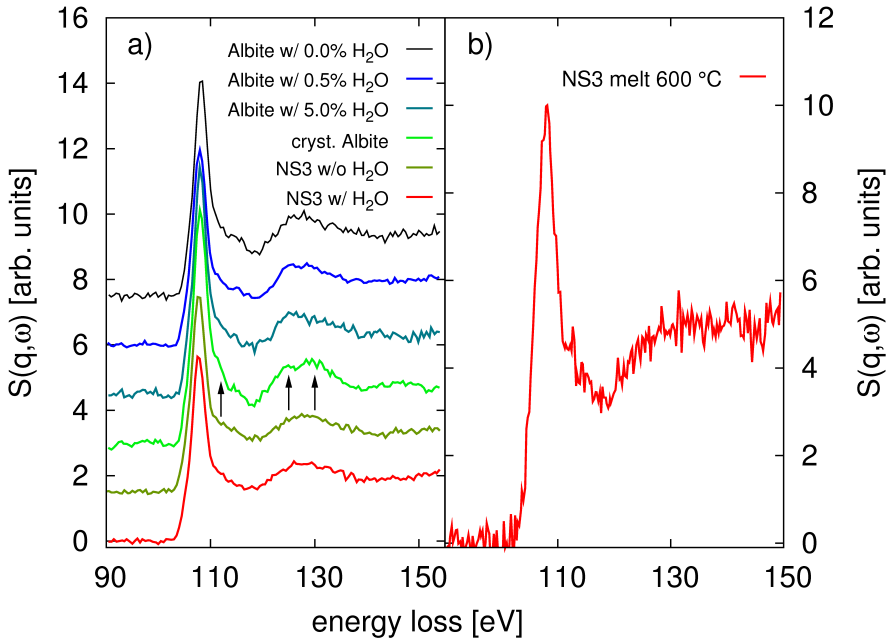

Figure 6.6: a) Si $L_{2,3}$-edge of different water bearing and water free glasses (NS3: $Na_2Si_3O_7$ and Albite: $NaAlSi_3O_8$) as well as a crystalline Albite reference sample. Small changes of the glassy samples as compared to the crystalline sample are indicated by arrows. b) Results of a first *in situ* measurement of the Si $L_{2,3}$-edge in a hydrous silicate melt at $T = 600$ °C and a pressure of approx. $p = 230$ MPa.

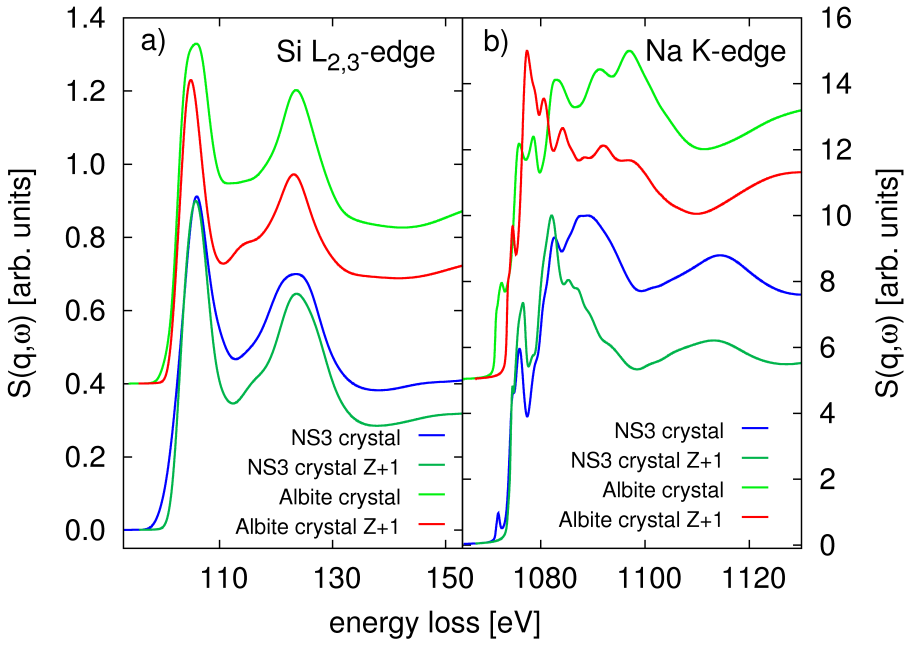

Figure 6.7: a) Simulated XRS of the Si $L_{2,3}$-edge in crystalline NS3 and Albite using the FEFFq program package. The calculated spectra agree qualitatively with the measured data. b) Na K-edge of crystalline NS3 and crystalline Albite using the Z and Z+1 approximation. The Z+1 approximation data were shifted by −231 eV (Na K-edge) and −27.5 eV (Si $L_{2,3}$-edge) on the energy loss scale.

the according multiplicities into account. The momentum transfer was set to a value of 9.2 $Å^{-1}$. The used crystallographic data is summarized in table 6.1. Fractal occupation of atomic sites, as is the case in crystalline Albite, was accounted for by calculating each possible configuration in the first shell and subsequently averaging over the resulting spectra taking the probability of the according fractal occupation into account. The simulation of the absorption edges was also performed in the Z+1-approximation[51], the resulting Na K-edge spectra were shifted by −231 eV, the Si $L_{2,3}$-edge spectra by −27.5 eV on the energy loss scale. Changing the core potential of a FEFF simulation by increasing the atomic number of the absorbing atom (here denoted Z+1 approximation) has been shown to enhance lower energy features, especially the white line in insulators.[52] This might prove to be useful for the measured materials. The results of the calculations are presented in Fig. 6.7 b).

The prominent white line and maximum around 130 eV energy loss in the Si $L_{2,3}$-edge are reproduced by the FEFF calculation, however, the maximum at 130 eV is overestimated in comparison with the white line by the simulation for both minerals. In contrast to the simulations of the Si $L_{2,3}$-edge simulations of the Na K-edge of crystalline NS3 and Albite reveal stronger spectral changes.

The near edge structure of the Na K-edge of Albite is much more pronounced than of

[51] Farges, F. et al. (2007). *AIP Conf. Proc.* **882**, 214–216.
[52] Nakanishi, K. and Ohta, T. (2009). *J. Phys.: Condens. Matter* **21**, 104214.

Compound	Space group	a [Å]	b [Å]	c [Å]	N_{Si}	N_{Na}
NS3	C2/m	7.192	10.604	9.804	3	2
Albite	P 21/C	8.274	12.991	7.144	4	1

Table 6.1: Summary of crystallographic parameters of NS3 and Albite. N_{Si} (N_{Na}) is the number of non-equivalent Si (Na) atoms in the unit cell.

NS3 showing a multi peak structure in the energy range from $1075 - 1100$ eV energy loss, whereas the near edge of NS3 is dominated by two (three) peaks at 1078 and 1082 eV (1078 , 1082 , and 1090 eV) for the Z+1 (Z) calculation. Moreover, the first EXAFS oscillations between 1100 and 1130 eV are markedly different showing a dip for Albite and a maximum for NS3 at approx. 1110 eV energy loss. Thus, *in situ* investigations of the Na K-edge in hydrous silicate melts might reveal structural changes more easily than is suggested by the presented Si $L_{2,3}$-edge data.

These preliminary results of the first *in situ* study of a silicate melt show the feasibility of using XRS and the HDAC technique to study shallow absorption edges of geologically relevant samples *in situ*. The observed spectral changes at the Si $L_{2,3}$-edge of different reference samples, however, are small and the limited quality of the *in situ* data allows no definite conclusion. Simulations of the $L_{2,3}$ and K absorption edges of crystalline NS3 and crystalline Albite demonstrate the feasibility of a direct comparison between calculated and experimental data and show that more prominent influence of changes in the local atomic structure on the shape of the absorption edges might be expected when investigating the Na K-edge. This gives rise to an approach similar to the strategy described in section 6.1 of comparing modeled spectra from MD simulation snapshots to the measured data which will lead to a thorough understanding of the structural changes of these materials under the influence of high pressure and high temperature and the intake of water.

6.3 Summary and outlook

XRS was used to investigate structural changes in geologically relevant samples under the influence of high pressure and high temperature. A resistively heated HDAC was employed to generate these extreme conditions. In contrast to soft x-ray absorption spectroscopy, XRS allowed to study the shallow absorption edges of the light elements oxygen and silicon of water and hydrous melts even when contained within the highly absorbing HDAC.

In a first experiment, the oxygen K-edge of water was measured for ambient and high pressure and temperature conditions. Measurements were conducted along the vapor pressure line and in the supercritical regime. Stark spectral changes were observed in the oxygen K-edges of water at elevated temperatures and pressures in comparison to spectra of the sample at ambient conditions. These changes were interpreted as due to changes in density, i.e. oxygen-oxygen distance, and a decreasing degree of H-bonding with increasing temperature. An increase in pressure at constant temperature reverses the effect observed with increasing p and T along the vapor pressure line. These interpretations are corroborated using *ab initio* MD simulations. Spectra calculated for MD simulation

snapshots using DFT in the TPA agree well with the experimental findings. No clear signs of structural inhomogeneities were found. Instead, the data suggests supercritical water to consist of a heavily distorted but not completely broken H_2O network. The influence of ion dissolution was studied by comparing spectra of pure water with spectra of aqueous HCl solutions at similar temperature and pressure conditions and was found to be similar to a pressure increase in accordance with earlier neutron scattering data. MD simulation data also for all experimental water densities and aqueous solutions of HCl might prove valuable for a deeper understanding and sound interpretation of the experimental findings, especially when comparing the influence of HCl solution with the effect of a density increase.

In a second study, first XRS experiments were conducted to investigate the influence of water intake on the local structure of silicate melts. Si $L_{2,3}$-edge spectra measured *ex situ* for different water bearing and water free silicate glasses and minerals show only subtle spectral changes between the samples. A first *in situ* measurement of an aqueous NS3 melt is presented but definite conclusions cannot be drawn due to the limited experimental energy resolution and statistical accuracy which complicate a proper background subtraction. The subtle changes in the Si $L_{2,3}$-edge shape were related to the rigid Si-O bond which leaves the local surrounding of the Si atom unchanged up to the temperature and pressure studied. Simulations of the Si $L_{2,3}$-edge of crystalline NS3 and Albite using the FEFFq program package were carried out successfully and show that more drastic changes may be expected when investigating the Na K-edge of these materials in line with earlier experimental data from quenched glasses. This gives rise to perform future *in situ* studies of Na bearing silicate melts focusing on the Na K-edge. An approach of comparing spectra modeled from MD simulation snapshots to the measured data, similar to the *in situ* study of water, will lead to a thorough understanding of the structural changes upon intake of water at high pressure and temperatures.

7 Summary and outlook

In this thesis, temperature and pressure induced changes in the local atomic and electronic structure of complex materials were investigated to address scientific questions arising from such diverse fields as materials science, materials design, fundamental solid state physics, and the geosciences. The study of x-ray absorption edges proved tremendously valuable to solve these questions.

In a series of three studies, the phase separation and formation of Ge NCs in Ge-oxide and silica matrices was investigated employing XAS at the Ge K-edge and XRD. Firstly, bulk amorphous GeO_x ($x \approx 1$) was found to exhibit significant amounts of Ge sub-oxides in the native (as prepared) sample. With increasing annealing temperature these sub-oxides disproportionate into Ge and GeO_2 and Ge NCs are formed once a sufficient Ge domain size is reached. The NC formation takes place after the phase separation process is almost completed. GeO_2 domains crystallize at higher temperatures than necessary for crystallization of Ge such that a temperature window for the production of Ge NCs embedded in a Ge-oxide matrix is attainable. These findings are in line with the ICM model derived for bulk a-SiO and thus important from a materials science point of view.

Secondly, the phase separation and formation of size controlled Ge NCs in GeO_x/SiO_2 multilayers was studied. In an inert gas atmosphere the temperature behavior was found to be similar to bulk amorphous GeO. The size control of the Ge NCs is achieved by confining the NCs by the SiO_2 separation layers in the direction perpendicular to the substrate surface and by the GeO_2 product of the GeO phase separation parallel to the plane of the substrate's surface. Annealing in a reducing hydrogen containing atmosphere shifts the temperature regime, where the phase separation takes place, to lower values leading to the formation of Ge NCs between 400 and 450 °C. A lower crystallization temperature is important in order to decrease the necessary thermal budget for the production of oxide matrix embedded NCs. At temperatures above this initial crystallization temperature the reducing properties of the hydrogen in the annealing ambient can be utilized to reduce the Ge-oxide matrix enhancing the Ge NC density.

Thirdly, the formation of size controlled Ge-oxide free Ge NCs in a silica matrix was investigated. Similar to the size controlled growth of Ge NCs in a Ge-oxide matrix, a superlattice approach employing alternating thin SiO_2 and $GeSiO_x$ layers was used to ensure size control. It was found that in the temperature regime, where the disproportionation reaction of GeO_x takes place in the binary system, a redistribution of oxygen from Ge-oxides to the Si matrix material takes place. Depending on the stoichiometry of the SiO_x matrix pure Ge NCs embedded in a silica matrix can be produced. Here, a slightly under-stoichiometric SiO_x matrix with $x < 2$ is capable of compensating oxygen contaminants in the annealing atmosphere and the possible loss of volatile GeO. In addition to the study of the Ge K-edge, a Si absorption edge such as the Si K or $L_{2,3}$-edge should be investigated for a complete understanding of the processes in these ternary systems.

The atomic and electronic structure of complex Ba intercalated Si clathrates was investigated by employing the momentum transfer dependence of XRS, aiming at a full understanding of the interaction between the guest and host, and ultimately, at the mechanisms behind the intriguing pressure-induced phase transitions found in Ba_8Si_{46}.

In a first study, the Ba GR in the vicinity of the Ba $N_{4,5}$-edge was measured for the clathrates Ba_8Si_{46} and $Ba_{24}Si_{100}$ over a large range of momentum transfers in order to investigate the debated modulations of the GR due to the different local environments of the encaged Ba atoms and to assess the practicality of using this structure induced modulation of the GR as a fingerprinting tool to study the pressure-induced phase transitions. Using this new data and data from a previous study different modulations of the Ba GR were confirmed and clearly separated from spectral changes caused by the finite momentum transfer in the measurements. Thus, deviations of the measured and simulated spectra are in large part due to a small but finite momentum transfer in the XRS measurements. The shape of the GR in $BaSi_6$ and Ba_8Si_{46} is similar and differs from that of $Ba_{24}Si_{100}$, which suggests the smaller degree of symmetry of the Ba environment in $Ba_{24}Si_{100}$ as the origin of the modulation. This is confirmed by calculations using the FEFF program package employing TDLDA. For a fingerprinting of Ba in the different cages spectra of even higher quality, in combination with more advanced theoretical approaches, will be necessary.

Moreover, electronic phase transitions in the clathrate Ba_8Si_{46} were investigated by measuring the multiplet-like features of the Ba $N_{4,5}$-edge accessible using XRS at high momentum transfers. This approach, in contrast to measuring the Ba GR at low momentum transfer, circumvents the overlap of the GR with the K-edge of the often used Be gasket material in high pressure DACs. Employing new and different gasket materials, like boron nitride, may allow to also study pressure dependence of the Ba GR in these clathrates. In the presented experiment the Ba $N_{4,5}$-edge and the adjacent Si $L_{2,3}$-edge of Ba_8Si_{46} were measured for pressures between $1.5 - 19.4$ GPa. For the first time direct evidence of three electronic phase transitions at 4, 7 , and 16 GPa was found in accordance with indirect probes such as XRD and optical Raman spectroscopy. The electronic nature of these phase transitions qualifies them as electron topological transitions.

The feasibility of studying shallow absorption edges of geologically relevant samples under high pressure and high temperature conditions was shown by investigating the O K-edge of water and the Si $L_{2,3}$-edge of a hydrous NS3 melt under such conditions. High pressure and high temperature conditions were achieved using a HDAC with resistive heating.

The influence of high temperature and high pressure on the local atomic structure of water was investigated using XRS. Measurements were conducted at pressure and temperature points along the vapor pressure line and in the supercritical regime. Prominent spectral changes could be observed in the oxygen K-edges of water at elevated temperatures and pressures in comparison to spectra of the sample at ambient conditions and could be interpreted as due to a variation of oxygen-oxygen distance and degree of H-bonding in the sample. Spectra calculated from *ab initio* MD simulation snapshots show remarkable resemblance with the experimental findings and corroborate the experimental results. Structural information derived from partial RDFs are in line with the qualitative interpretation of the experimental XRS spectra. In particular, the data are found to be inconsistent with an earlier inhomogeneous model of supercritical water. Instead, the data

suggest supercritical water to consist of a heavily distorted but not completely broken H_2O network. *Ab initio* calculations from MD simulations for all experimental densities will complete the understanding of the local structure of water in the supercritical regime. Furthermore, the influence of ion dissolution was studied by comparing spectra of pure water with spectra of aqueous HCl solution at similar temperature and pressure conditions and was found to be similar to a pressure increase in accordance with earlier neutron scattering data. Future *ab initio* MD simulations for these aqueous solutions will be useful to interpret the results.

A first attempt to measure the Si $L_{2,3}$-edge of a hydrous NS3 melt *in situ* showed that it is possible to extract this edge from hydrous samples. However, a comparison of different reference materials like silicate glasses and minerals exhibits only small changes in the Si $L_{2,3}$-edge to be expected. Calculations of the Si $L_{2,3}$- and Na K-edge of crystalline NS3 and Albite using the FEFFq program package reproduce the Si $L_{2,3}$-edge reasonably but exhibit an increased sensitivity to the local structure at the Na K-edge compared to the Si $L_{2,3}$-edge, in line with earlier soft x-ray absorption spectra of quenched glassy samples. The presented preliminary study also encourages an approach to investigate the local structure of geologically relevant hydrous melts similar to the case of supercritical water by comparing calculated spectra from MD snapshots with the experimental data.

The presented thesis demonstrates how XAS and XRS can be utilized to study local electronic and atomic structures in a variety of fields. The incorporation of advanced computational methods available today with structural models from MD simulations allows for a deeper insight into the local structure even in amorphous solids, liquids, and melts.

Supplement to chapter 6

Estimating pressures by solving the equation of state

In experiments involving both high temperature and high pressure the pressure calibration by means of a small ruby chip in the sample volume of a DAC is not feasible since the ruby Raman mode is smeared out at elevated temperatures. To circumvent this difficulty, the pressure in the presented measurements was estimated using an equation of state after Wagner and Pruß (Wagner, W. and Pruß, A. (1999). *J. Phys. Chem. Ref. Data* **31**, 387). For aqueous solutions, this allows one to evaluate the pressure of a liquid sample by measuring the so called homogenization temperature. For the presented cases, this implies that the liquid sample (L) is loaded into the HDAC with a small vapor (V) bubble. The homogenization temperature ($L + V \rightarrow L$) corresponds to the temperature at which the vapor bubble dissolves. This can be monitored by a camera and lens setup and the temperature can be measured using a type-K thermocouple. From this homogenization temperature, the pressure can be estimated via the equation of state. Fig. 7.1 shows solutions to the equation of state after Wagner and Pruß parametrically for different homogenization temperatures and densities, respectively. Also shown are the melting curves of the ice phases from Wagner, W. et al. (1994). *J. Phys. Chem. Ref. Data* **23**, 515–528, which can also be used as pressure gauge.

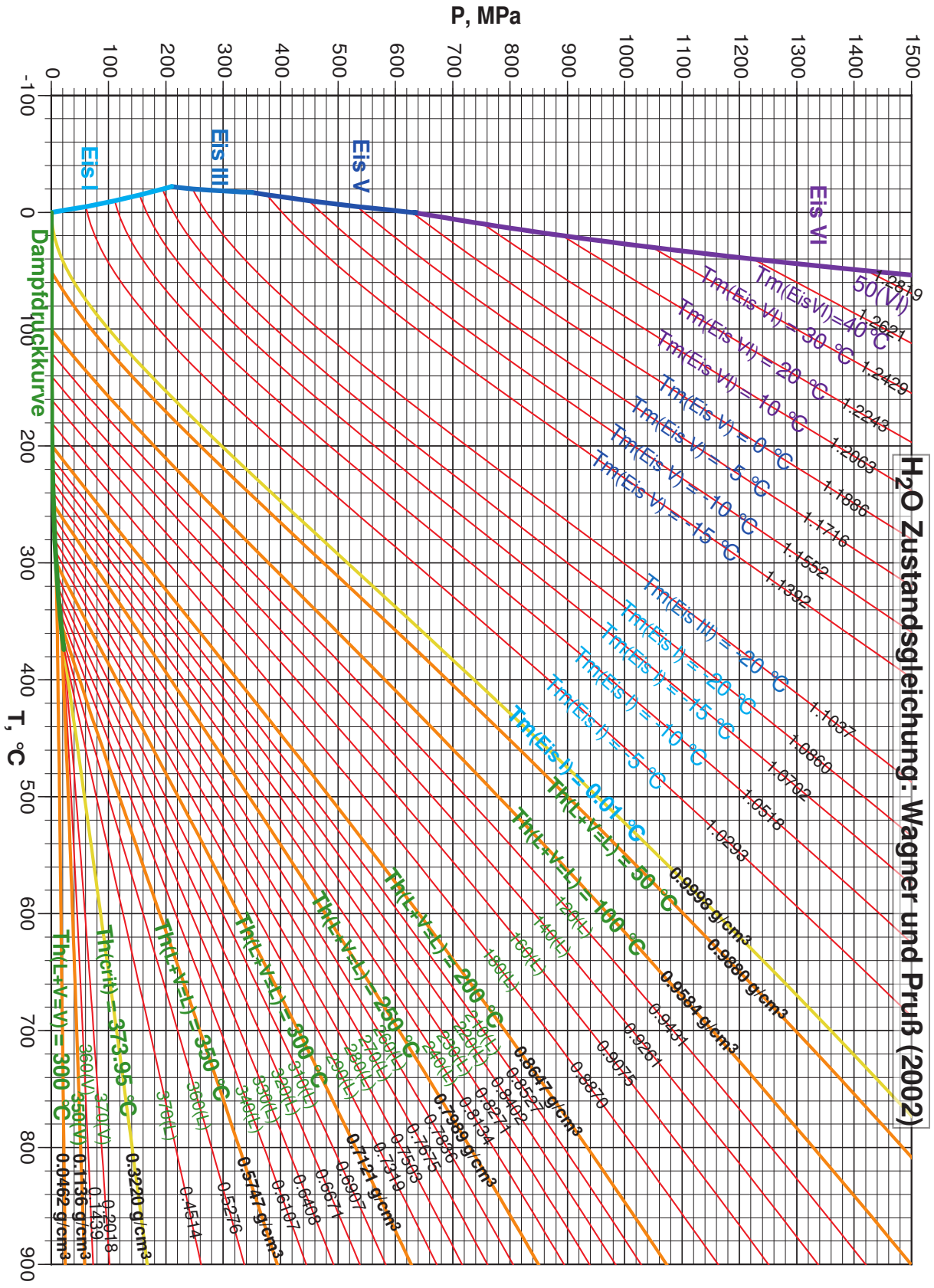

Figure 7.1: Solutions to the equations of state of water after Wagner *et al.* parametrically for different densities and homogenization temperatures. Melting curves of the ice phases are also shown. This figure was provided courtesy of C. Schmidt, GFZ Potsdam, Potsdam, Germany.

Bibliography

Akiya, N. and Savage, P.E. (2002). *Chem. Rev.* **102**, 2725–2750.

Alivisatos, A.P. (1996). *J. Phys. Chem.* **100**, 13226–13239.

Als-Nielsen, J. and McMorrow, D. (2011). *Elements of modern X-ray physics*. Wiley.

Amusia, M.Y. and Baltenkov, A.S. (2006). *Phys. Rev. A* **73**, 062723.

Ankudinov, A.L. ; Ravel, B. ; Rehr, J.J., and Conradson, S.D. (1998). *Phys. Rev. B* **58**, 7565.

Baba, H. (1956). *Bull. Chem. Soc. Jpn.* **29**, 789–793.

Ball, P. (2000). *A Biography of Water: Life's Matrix*. New York: Farrar, Straus and Giroux.

– (2008). *Nature* **452**, 291–292.

Ball, P. and Stillinger, F.H. (1999). *Nature* **401**, 850–850.

Bassett, W.A. (2003). *Eur. J. Mineral.* **15**, 773.

Batra, Y. ; Kabiraj, D., and Kanjilal, D. (2007). *Solid State Commun.* **143**, 213–216.

Bergmann, U. ; Wernet, P. ; Glatzel, P. ; Cavalleri, M. ; Pettersson, L.G.M. ; Nilsson, A., and Cramer, S.P. (2002). *Phys. Rev. B* **66**, 092107.

Bergmann, U. ; Nordlund, D. ; Wernet, P. ; Odelius, M. ; Pettersson, L.G.M., and Nilsson, A. (2007*a*). *Phys. Rev. B* **76**, 024202.

Bergmann, U. ; Di Cicco, A. ; Wernet, P. ; Principi, E. ; Glatzel, P., and Nilsson, A. (2007*b*). *J. Chem. Phys.* **127**, 174504.

Blume, M. (1985). *J. Appl. Phys.* **57**, 3615–3618.

Bobev, S. and Sevov, S.C. (2000). *J. Solid State Chem.* **153**, 92–105.

Brechignac, C. and Connerade, J.P. (1994). *J. Phys. B: At. Mol. Phys.* **27**, 3795.

Bruchez, M. ; Moronne, M. ; Gin, P. ; Weiss, S., and Alivisatos, A.P. (1998). *Science* **281**, 2013.

Cai, Y.Q. ; Mao, H.K. ; Chow, P.C. ; Tse, J.S. ; Ma, Y. ; Patchkovskii, S. ; Shu, J.F. ; Struzhkin, V. ; Hemley, R.J. ; Ishii, H., et al. (2005). *Phys. Rev. Lett.* **94**, 25502.

Car, R. and Parrinello, M. (1985). *Phys. Rev. Lett.* **55**, 2471–2474.

Chervin, J.C. ; Canny, B., and Mancinelli, M. (2001). *High Pressure Res.* **21**, 305–314.

Christensen, M. ; Abrahamsen, A.B. ; Christensen, N.B. ; Juranyi, F. ; Andersen, N.H. ; Lefmann, K. ; Andreasson, J. ; Bahl, C.R.H., and Iversen, B.B. (2008). *Nat. Mater.* **7**, 811–815.

Conibeer, G. (2007). *Mater. Today* **10**, 42–50.

Connerade, J.P. ; Esteva, J.M., and Karnatak, R.C. (1987). "Giant resonances in atoms, molecules, and solids."*NATO ASIB Proc. 151: Giant Resonances in Atoms, Molecules, and Solids*. Vol. 1.

Connerade, J.P. ; Dolmatov, V.K., and Manson, S.T. (2000). *J. Phys. B: At. Mol. Phys.* **33**, 2279.

Crljen, Z. ; Luberek, J. ; Wendin, G., and Levine, Z.H. (1994). *Phys. Rev. A* **50**, 3529.

De Wispelaere, S. ; Cabaret, D. ; Levelut, C. ; Rossano, S. ; Flank, A.M. ; Parent, P., and Farges, F. (2004). *Chem. Geol.* **213**, 63–70.

Debenedetti, P.G. (1996). *Metastable liquids: concepts and principles.* Princeton Univ Press.

– (2003). *J. Phys.: Condens. Matter* **15**, R1669.

Farges, F. ; de Wispelaere, S. ; Rossano, S. ; Muños, M. ; Wilke, M. ; Flank, A.M., and Lagarde, P. (2007). *AIP Conf. Proc.* **882**, 214–216.

Feroughi, O.M. ; Sternemann, C. ; Sahle, Ch.J. ; Schroer, M.A. ; Sternemann, H. ; Conrad, H. ; Hohl, A. ; Seidler, G.T. ; Bradley, J. ; Fister, T.T. ; Balasubramanian, M. ; Sakko, A. ; Pirkkalainen, K. ; Hämäläinen, K., and Tolan, M. (2010). *Appl. Phys. Lett.* **96**, 081912.

Fiolhais, C. ; Nogueira, F., and Marques, M. (2003). *A primer in density functional theory.* Vol. 620. Springer Verlag.

Fister, T.T. ; Seidler, G.T. ; Wharton, L. ; Battle, A.R. ; Ellis, T.B. ; Cross, J.O. ; Macrander, A.T. ; Elam, W.T. ; Tyson, T.A., and Qian, Q. (2006). *Rev. Sci. Instrum.* **77**, 063901.

Fukui, H. ; Huotari, S. ; Andrault, D., and Kawamoto, T. (2007). *J. Chem. Phys.* **127**, 134502.

Fukuoka, H. ; Ueno, K., and Yamanaka, S. (2000). *J. Organomet. Chem.* **611**, 543–546.

Glatzel, P. and Bergmann, U. (2005). *Coord. Chem. Rev.* **249**, 65–95.

Godefroo, S. ; Hayne, M. ; Jivanescu, M. ; Stesmans, A. ; Zacharias, M. ; Lededev, O. ; Van Tendeloo, G., and Moshchalkov, V.V. (2008). *Nature Nanotech.* **3**, 174–178.

Gordon, R.A. ; Seidler, G.T. ; Fister, T.T. ; Haverkort, M.W. ; Sawatzky, G.A. ; Tanaka, A., and Sham, T.K. (2008). *Europhys. Lett.* **81**, 26004.

Hämäläinen, K. ; Siddons, D.P. ; Hastings, J.B., and Berman, L.E. (1991). *Phys. Rev. Lett.* **67**, 2850–2853.

Hammersley, A.P. ; Svensson, S.O. ; Hanfland, M. ; Fitch, A.N., and Hausermann, D. (1996). *High Pressure Res.* **14**, 235–248.

Hedin, L. and Lundqvist, B.I. (1971). *J. Phys. C: Solid State Phys.* **4**, 2064.

Heitmann, J. ; Müller, F. ; Zacharias, M., and Gösele, U. (2005). *Adv. Mater.* **17**, 795–803.

Hermann, K. et al. *http://w3.rz-berlin.mpg.de/hermann/StoBe/index.html.*

Hetenyi, B. ; De Angelis, F. ; Giannozzi, P., and Car, R. (2004). *J. Chem. Phys.* **2004**, 120.

Hirschman, K.D. ; Tsybeskov, L. ; Duttagupta, S.P., and Fauchet, P.M. (1996). *Nature* **384**, 338–341.

Hohenberg, P. and Kohn, W. (1964). *Phys. Rev.* **136**, B864.

Hohl, A. ; Wieder, T. ; Aken, P.A. Van ; Weirich, T.E. ; Denninger, G. ; Vidal, M. ; Oswald, S. ; Deneke, C. ; Mayer, J., and Fuess, H. (2003). *J. Non-Cryst. Solids* **320**, 255–280.

Hove, L. Van (1954). *Phys. Rev.* **95**,1, 249–262.

Huang, C. ; Wikfeldt, K.T. ; Tokushima, T. ; Nordlund, D. ; Harada, Y. ; Bergmann, U. ; Niebuhr, M. ; Weiss, T.M. ; Horikawa, Y. ; Leetmaa, M., et al. (2009). *Proc. Natl. Acad. Sci.* **106**, 15214.

Huber, C. and Wächtershäuser, G. (1997). *Science* **276**, 245.

Huotari, S. ; Pylkkänen, T. ; Verbeni, R. ; Monaco, G., and Hämäläinen, K. (2011). *Nat. Mater.* **10**, 489–493.

Hurd, A.J. and Sinha, S. (2010). *Neutrons & nanoscience (Neutron scattering applications & techniques).* Springer.

Israelachvili, J. and Wennerström, H. (1996). *Nature* **379**, 219–225.

Iyer, S.S. and Xie, Y.H. (1993). *Science* **260**, 40.

Johann, H.H. (1931). *Zeitschrift für Physik* **69**, 185.

John, S. ; Ratcliffe, C.I. ; Powell, B.M. ; Sears, V.F., and Handa, Y.P. (1997). *J. Phys. Chem. A* **101**, 4491–4495.

Joly, Y. (2001). *Phys. Rev. B* **63**, 125120.

Kapaklis, V. ; Politis, C. ; Poulopoulos, P., and Schweiss, P. (2005). *Appl. Phys. Lett.* **87**, 123114.

Katayanagi, H. ; Kafle, B.P. ; Kou, J. ; Mori, T. ; Mitsuke, K. ; Takabayashi, Y. ; Kuwahara, E., and Kubozono, Y. (2008). *J. Quant. Spectrosc. Ra.* **109**, 1590–1598.

Kawaji, H. ; Horie, H. ; Yamanaka, S., and Ishikawa, M. (1995). *Phys. Rev. Lett.* **74**, 1427–1429.

Kawaji, H. ; Iwai, K. ; Yamanaka, S., and Ishikawa, M. (1996). *Solid state commun.* **100**, 393–395.

Keppler, H. (1996). *Nature* **380**, 237–240.

Kilcoyne, A.L.D. ; Aguilar, A. ; Müller, A. ; Schippers, S. ; Cisneros, C. ; Alna'Washi, G. ; Aryal, N.B. ; Baral, K.K. ; Esteves, D.A. ; Thomas, C.M., and Phaneuf, R. A. (2010). *Phys. Rev. Lett.* **105**, 213001.

Kimball, G.E. and Shortley, G.H. (1934). *Phys. Rev.* **45**, 815.

Kohn, S.C. ; Dupree, R., and Smith, M.E. (1989). *Geochim. et Cosmochim. Acta* **53**, 2925–2935.

Kohn, W. and Sham, L.J. (1965). *Phys. Rev.* **140**, 1133–1138.

Koningsberger, D.C. and Prins, R. (1987). *X-ray absorption: principles, applications, techniques of EXAFS, SEXAFS and XANES*. John Wiley and Sons Inc., New York, NY.

Korol, A.V. and Solov'yov, A.V. (2010). *J. Phys. B: At. Mol. Phys.* **43**, 201004.

Kovalev, D. ; Heckler, H. ; Polisski, G., and Koch, F. (1999). *Phys. Status Solidi B* **215**, 871–932.

Kramers, H.A. and Heisenberg, W. (1925). *Z. Phys. A: Hadrons Nucl.* **31**, 681–708.

Krywka, C. ; Paulus, M. ; Sternemann, C. ; Volmer, M. ; Remhof, A. ; Nowak, G. ; Nefedov, A. ; Poter, B. ; Spiegel, M., and Tolan, M. (2005). *J. Synchrotron Rad.* **13**, 8–13.

Krywka, C. ; Sternemann, C. ; Paulus, M. ; Javid, N. ; Winter, R. ; Al-Sawalmih, A. ; Yi, S. ; Raabe, D., and Tolan, M. (2007). *J. Synchrotron Rad.* **14**, 244–251.

Kume, T. ; Fukuoka, H. ; Koda, T. ; Sasaki, S. ; Shimizu, H., and Yamanaka, S. (2003). *Phys. Rev. Lett.* **90**, 155503.

Kümmerlen, J. ; Merwin, L.H. ; Sebald, A., and Keppler, H. (1992). *J. Phys. Chem.* **96**, 6405–6410.

Lambert, T.N. ; Andrews, N.L. ; Gerung, H. ; Boyle, T.J. ; Oliver, J.M. ; Wilson, B.S., and Han, S.M. (2007). *Small* **3**, 691–699.

Langford, J.I. and Wilson, A.J.C. (1978). *J. Appl. Crystall.* **11**, 102–113.

Leberman, R. and Soper, A.K. (1995). *Nature* **378**, 364–366.

Leetmaa, M. ; Ljungberg, M.P. ; Lyubartsev, A. ; Nilsson, A., and Pettersson, L.G.M. (2010). *J. Electron. Spectrosc. Relat. Phenom.* **177**, 135–157.

Lortz, R. ; Viennois, R. ; Petrovic, A. ; Wang, Y. ; Toulemonde, P. ; Meingast, C. ; Koza, M.M. ; Mutka, H. ; Bossak, A., and San Miguel, A. (2008). *Phys. Rev. B* **77**, 224507.

Lu, Z.H. ; Lockwood, D.J., and Baribeau, J.M. (1995). **378**, 258–260.

Luberek, J. and Wendin, G. (1996). *Chem. Phys. Lett.* **248**, 147–152.

Lützenkirchen-Hecht, D. ; Wagner, R. ; Haake, U. ; Watenphul, A., and Frahm, R. (2009). *J. Synchrotron Rad.* **16**, 264–272.

Madjet, M.E. ; Renger, T. ; Hopper, D.E. ; McCune, M.A. ; Chakraborty, H.S. ; Rost, J.M., and Manson, S.T. (2010). *Phys. Rev. A* **81**, 013202.

Maeda, Y. ; Tsukamoto, N. ; Yazawa, Y. ; Kanemitsu, Y., and Masumoto, Y. (1991). *Appl. Phys. Lett.* **59**, 3168–3170.

Mamiya, M. ; Takei, H. ; Kikuchi, M., and Uyeda, C. (2001). *J. Cryst. Growth* **229**, 457–461.

Mamiya, M. ; Kikuchi, M., and Takei, H. (2002). *J. Cryst. Growth* **237**, 1909–1914.

Manning, C.E. (2004). *Earth. Planet. Sci. Lett.* **223**, 1–16.

Marshak, S. (2004). *Essentials of geology*. WW Norton.

Miguel, A.S. ; Merlen, A. ; Toulemonde, P. ; Kume, T. ; Floch, S.L. ; Aouizerat, A. ; Pascarelli, S. ; Aquilanti, G. ; Mathon, O., and Bihan, T.L. (2005). *Europhys. Lett.* **69**, 556.

Mitsuke, K. ; Mori, T. ; Kou, J. ; Haruyama, Y., and Kubozono, Y. (2005*a*). *J. Chem. Phys.* **122**, 064304.

Mitsuke, K. ; Mori, T. ; Kou, J. ; Haruyama, Y. ; Takabayashi, Y., and Kubozono, Y. (2005*b*). *Int. J. Mass Spectrom.* **243**, 121–125.

Mizuno, Y. and Ohmura, Y. (1967). *J. Phys. Soc. Jpn.* **22**,2, 445–449.

Morita, T. ; Kusano, K. ; Ochiai, H. ; Saitow, K., and Nishikawa, K. (2000). *J. Chem. Phys.* **112**, 4203.

Mott, S.N. (1978). *Rev. Mod. Phys.* **50**, 203.

Müller, A. ; Schippers, S. ; Phaneuf, R.A. ; Habibi, M. ; Esteves, D. ; Wang, J.C. ; Kilcoyne, A.L.D. ; Aguilar, A. ; Yang, S., and Dunsch, L. (2007). "Photoionization of the endohedral fullerene ions $Sc_3N@C_{80}^+$ and $Ce@C_{82}^+$ by synchrotron radiation."Vol. 88, 012038.

Müller, A. ; Schippers, S. ; Habibi, M. ; Esteves, D. ; Wang, J.C. ; Phaneuf, R.A. ; Kilcoyne, A.L.D. ; Aguilar, A., and Dunsch, L. (2008*a*). *Phys. Rev. Lett.* **101**, 133001.

– (2008*b*). *Phys. Rev. Lett.* **101**, 133001.

Myneni, S. ; Luo, Y. ; Näslund, L.Å. ; Cavalleri, M. ; Ojamäe, L. ; Ogasawara, H. ; Pelmenschikov, A. ; Wernet, P. ; Väterlein, P. ; Heske, C., et al. (2002). *J. Phys.: Cond. Matter* **14**, L213.

Mysen, B.O. and Richet, P. (2005). *Silicate glasses and melts: Properties and structure*. Vol. 10.

Nakanishi, K. and Ohta, T. (2009). *J. Phys.: Condens. Matter* **21**, 104214.

Nibbering, E.T.J. and Elsaesser, T. (2004). *Chem. Rev.* **104**, 1887–1914.

Nilsson, A. ; Nordlund, D. ; Waluyo, I. ; Huang, N. ; Ogasawara, H. ; Kaya, S. ; Bergmann, U. ; Näslund, L.Å. ; Öström, H. ; Wernet, P., et al. (2010). *J. Electron. Spectrosc. Relat. Phenom.* **177**, 99–129.

Nowak, M. and Behrens, H. (1995). *Geochim. et Cosmochim. Acta* **59**, 3445–3450.

Odelius, M. ; Cavalleri, M. ; Nilsson, A., and Pettersson, L.G.M. (2006). *Phys. Rev. B* **73**, 024205.

Patterson, A.L. (1939). *Phys. Rev.* **56**, 978.

Pavesi, L. ; Negro, L.D. ; Mazzoleni, C. ; Franzo, G., and Priolo, F. (2000). *Nature* **408**, 440–444.

Petrenko, V.F. and Whitworth, R.W. (1999). *Physics of ice*. Oxford University Press.

Pouchard, M. ; Cros, C. ; Hagenm
uller, P. ; Reny, E. ; Ammar, A. ; Ménétrier, M., and Bassat, J.M. (2002). *Solid State Sci.* **4**, 723–729.

Pylkkänen, T. (2011). "Disordered matter studied by x-ray Raman scattering." PhD thesis. University of Helsinki.

Pylkkänen, T. ; Giordano, V.M. ; Chervin, J.-C. ; Sakko, A. ; Hakala, M. ; Soininen, J.A. ; Hämäläinen, K. ; Monaco, G., and Huotari, S. (2010). *J. Phys. Chem. B* **114**, 3804–3808.

Rasaiah, J.C. ; Garde, S., and Hummer, G. (2008). *Annu. Rev. Phys. Chem.* **59**, 713–740.

Rehr, J.J. and Albers, R.C. (1990). *Phys. Rev. B* **41**, 8139.

– (2000). *Rev. Mod. Phys.* **72**, 621–654.

Rehr, J.J. ; Kas, J.J. ; Vila, F.D. ; Prange, M.P., and Jorissen, K. (2010). *Phys. Chem. Chem. Phys.* **12**, 5503–5513.

Richter, M. ; Meyer, M. ; Pahler, M. ; Prescher, T. ; Raven, E. ; Sonntag, B., and Wetzel, H.E. (1989). *Phys. Rev. A* **40**, 7007.

Röelver, R. ; Berghoff, B. ; Bätzner, D.L. ; Spangenberg, B., and Kurz, H. (2008). *Appl. Phys. Lett.* **92**, 212108.

Sahle, Ch.J. (2008). "Disproportionierung und Kristallisation von massivem amorphen Germaniummonoxid." MA thesis. TU Dortmund, unpublished.

Sahle, Ch.J. ; Sternemann, C. ; Conrad, H. ; Herdt, A. ; Feroughi, O.M. ; Tolan, M. ; Hohl, A. ; Wagner, R. ; Lützenkirchen-Hecht, D. ; Frahm, R. ; Hämäläinen, K., and Tolan, M. (2009). *Appl. Phys. Lett.* **95**, 021910–021910.

Sakko, A. ; Hakala, M. ; Soininen, J.A., and Hämäläinen, K. (2007). *Phys. Rev. B* **76**, 205115.

Sakko, A. ; Sternemann, C. ; Sahle, Ch.J. ; Sternemann, H. ; Feroughi, O.M. ; Conrad, H. ; Djurabekova, F. ; Hohl, A. ; Seidler, G. ; Tolan, M., and Hämäläinen, K. (2010). *Phys. Rev. B* **81**, 205317.

Sakko, A. ; Galambosi, S. ; Inkinen, J. ; Pylkkänen, T. ; Hakala, M. ; Huotari, S., and Hämäläinen, K. (2011). *Phys. Chem. Chem. Phys.* **13**, 11678–11685.

San-Miguel, A. and Toulemonde, P. (2005). *High Pressure Res.* **25**, 159–185.

San-Miguel, A. ; Kéghélian, P. ; Blase, X. ; Mélinon, P. ; Perez, A. ; Itié, J.P. ; Polian, A. ; Reny, E. ; Cros, C., and Pouchard, M. (1999). *Phys. Rev. Lett.* **83**, 5290–5293.

San-Miguel, A. ; Mélinon, P. ; Connétable, D. ; Blase, X. ; Tournus, F. ; Reny, E. ; Yamanaka, S., and Itié, J.P. (2002). *Phys. Rev. B* **65**, 054109.

Schacht, A. ; Sternemann, C. ; Hohl, A. ; Sternemann, H. ; Sahle, Ch.J. ; Paulus, M., and Tolan, M. (2009). *J. Non-Cryst. Solids* **355**, 1285–1287.

Schmidt, B.C. ; Riemer, T. ; Kohn, S.C. ; Behrens, H., and Dupree, R. (2000). *Geochim. et Cosmochim. Acta* **64**, 513–526.

Schmidt, C. and Rickers, K. (2003). *Am. Mineral.* **88**, 288.

Schmidt, C. and Watenphul, A. (2010). *Geochim. Cosmochim. Acta* **74**, 6852–6866.

Schülke, W. (1991). *Handbook on Synchrotron Radiation*. Ed. by Brown, G. and Moncton, D.E. Elsevier Science Publishers.

– (2007). *Electron dynamics by inelastic X-ray scattering*. Vol. 7. Oxford University Press, USA.

Sedlmeier, F. ; Horinek, D., and Netz, R.R. (2011). *J. Am. Chem. Soc.* **133**, 1391–1398.

Sette, F. ; Stöhr, J., and Hitchcock, A.P. (1984). *J. Chem. Phys.* **81**, 4906.
Shaw, R.W. ; Brill, T.B. ; Clifford, A.A. ; Eckert, C.A., and Franck, E.U. (1991). *Chem. Eng. News* **69**, 26–39.
Siskin, M. and Katritzky, A.R. (1991). *Science* **254**, 231.
Slack, G.A. (1995). *CRC Press, 1995* **407**,
Slater, J.C. and Johnson, K.H. (1972). *Phys. Rev. B* **5**, 844.
Soininen, J.A. ; Ankudinov, A.L., and Rehr, J.J. (2005). *Phys. Rev. B* **72**, 045136.
Soper, A.K. (2000). *Chem. Phys.* **258**, 121–137.
Soper, A.K. ; Teixeira, J., and Head-Gordon, T. (2010). *Proc. Nat. Acad. Sci.* **107**, E44.
Sternemann, C. ; Sternemann, H. ; Huotari, S. ; Lehmkühler, F. ; Tolan, M., and Tse, J.S. (2008). *J. Anal. At. Spectrom.* **23**, 807–813.
Sternemann, H. (2008). *A non-resonant inelastic x-ray scattering study on silicon oxides and clathrates*. PhD Thesis, TU Dortmund.
Sternemann, H. ; Sternemann, C. ; Tse, J.S. ; Desgreniers, S. ; Cai, Y. ; Vankó, G. ; Hiraoka, N. ; Schacht, A. ; Soininen, J.A., and Tolan, M. (2007*a*). *Phys. Rev. B* **75**, 245102.
Sternemann, H. ; Soininen, J.A. ; Sternemann, C. ; Hämäläinen, K., and Tolan, M. (2007*b*). *Phys. Rev. B* **75**, 075118.
Stöhr, J. (1992). *NEXAFS Spectroscopy*. Vol. 222238. Springer Berlin.
Suzuki, S. ; Ishii, T., and Sagawa, T. (1975). *J. Phys. Soc. Jpn.* **38**, 156.
Tanigaki, K. ; Shimizu, T. ; Itoh, K.M. ; Teraoka, J. ; Moritomo, Y., and Yamanaka, S. (2003). *Nat. Mater.* **2**, 653–655.
Tiwari, S. ; Rana, F. ; Hanafi, H. ; Hartstein, A. ; Crabbé, E.F., and Chan, K. (1996). *Appl. Phys. Lett.* **68**, 1377.
Toulemonde, P. ; Machon, D. ; Miguel, A. San, and Amboage, M. (2011). *Phys. Rev. B* **83**, 134110.
Triguero, L. ; Pettersson, L.G.M., and Ågren, H. (1998). *Phys. Rev. B* **58**, 8097.
Tse, J.S. (2005). *Z. Kristallogr.* **220**, 521–530.
Tse, J.S. ; Uehara, K. ; Rousseau, R. ; Ker, A. ; Ratcliffe, C.I. ; White, M.A., and MacKay, G. (2000). *Phys. Rev. Lett.* **85**, 114–117.
Tse, J.S. ; Flacau, R. ; Desgreniers, S. ; Iitaka, T., and Jiang, J.Z. (2007). *Phys. Rev. B* **76**, 174109.
Tse, J.S. ; Shaw, D.M. ; Klug, D.D. ; Patchkovskii, S. ; Vankó, G. ; Monaco, G., and Krisch, M. (2008). *Phys. Rev. Lett.* **100**, 95502.
Tse, J.S. ; Yang, L. ; Zhang, S.J. ; Jin, C.Q. ; Sahle, Ch.J. ; Sternemann, C. ; Nyrow, A. ; Giordano, V. ; Jiang, J.Z. ; Yamanaka, S. ; Desgreniers, S., and Tulk, C.A. (2011). *Phys. Rev. B* **84**, 184105.
Verbeni, R. ; Pylkkänen, T. ; Huotari, S. ; Simonelli, L. ; Vankó, G. ; Martel, K. ; Henriquet, C., and Monaco, G. (2009). *J. Synchrotron Rad.* **16**, 469–476.
Vining, C.B. (2008). *Nat. Mater* **7**,
Wagner, W. and Pruß, A. (1999). *J. Phys. Chem. Ref. Data* **31**, 387.
Wagner, W. ; Saul, A., and Pruss, A. (1994). *J. Phys. Chem. Ref. Data* **23**, 515–528.
Wendin, G. and Wästberg, B. (1993). *Phys. Rev. B* **48**, 14764.
Wernet, P. ; Nordlund, D. ; Bergmann, U. ; Cavalleri, M. ; Odelius, M. ; Ogasawara, H. ; Näslund, L.Å. ; Hirsch, T.K. ; Ojamäe, L. ; Glatzel, P., et al. (2004). *Science* **304**, 995.

Wernet, P. ; Testemale, D. ; Hazemann, J.L. ; Argoud, R. ; Glatzel, P. ; Pettersson, L.G.M. ; Nilsson, A., and Bergmann, U. (2005). *J. Chem. Phys.* **123**, 154503.

Yamaguchi, O. ; Kotera, K. ; Asano, M., and Shimizu, K. (1982). *J. Chem. Soc., Dalton Trans.* (10 1982), 1907–1910.

Yamanaka, S. (2010). *Dalton Trans.* **39**, 1901–1915.

Yamanaka, S. and Maekawa, S. (2006). *Z. Naturforsch.* **61b**, 1493–1499.

Yamanaka, S. ; Horie, H.O. ; Kawaji, H., and Ishikawa, M. (1995). *Eur. J. Sol. State. Inor.* **32**, 799–807.

Yamanaka, S. ; Enishi, E. ; Fukuoka, H., and Yasukawa, M. (2000). *Inorg. Chem.* **39**, 56–58.

Yang, L. ; Ma, Y.M. ; Iitaka, T. ; Tse, J.S. ; Stahl, K. ; Ohishi, Y. ; Wang, Y. ; Zhang, R.W. ; Liu, J.F., and Mao, H.K. (2006). *Phys. Rev. B* **74**, 245209.

Zacharias, M. and Streitenberger, P. (2000). *Phys. Rev. B* **62**, 8391–8396.

Zacharias, M. ; Bläsing, J. ; Löhmann, M., and Christen, J. (1996). *Thin Solid Films* **278**, 32–36.

Zacharias, M. ; Weigand, R. ; Dietrich, B. ; Stolze, F. ; Blasing, J. ; Veit, P. ; Drusedau, T., and Christen, J. (1997). *J. Appl. Phys.* **81**, 2384–2390.

Zacharias, M. ; Heitmann, J. ; Scholz, R. ; Schmidt, M., and Bläsing, J. (2002). *Appl. Phys. Lett.* **80**, 661.

Zangwill, A. (1987). "A Condensed Matter View of Giant Resonance Phenomena." *NATO ASIB Proc. 151: Giant Resonances in Atoms, Molecules, and Solids.* Vol. 1, 321.

Zhang, B. ; Shrestha, S. ; Green, M.A., and Conibeer, G. (2010). *Appl. Phys. Lett.* **96**, 261901.

Zschintzsch, M. ; Jeutter, N.M. ; Borany, J. von ; Krause, M., and Mücklich, A. (2010). *J. Appl. Phys.* **107**, 034306.

Publications

Publications directly related to this thesis

- A. Schacht, C. Sternemann, A. Hohl, H. Sternemann, **Ch.J. Sahle**, M. Paulus, and M. Tolan (2009). *J. Non-Cryst. Solids* 355, 1285-1287: "Temperature-induced obliteration of sub-oxide interfaces in amorphous GeO".

- **Ch.J. Sahle**, C. Sternemann, H. Conrad, A. Herdt, O.M. Feroughi, M. Tolan, A. Hohl, R. Wagner, D. Lützenkirchen-Hecht, R. Frahm, A. Sakko, and K. Hämäläinen (2009). *Appl. Phys. Lett.* 95, 021910: "Phase separation and nanocrystal formation in GeO".

- O.M. Feroughi, C. Sternemann, **Ch.J. Sahle**, M.A. Schroer, H. Sternemann, H. Conrad, A. Hohl, G.T. Seidler, J. Bradley, T.T. Fister, M. Balasubramanian, A. Sakko, K. Pirkkalainen, K. Hämäläinen, and M.Tolan (2010). *Appl. Phys. Lett.* **96**, 081912: "Phase separation and Si nanocrystal formation in bulk SiO studied by x-ray scattering".

- A. Sakko, C. Sternemann, **Ch.J. Sahle**, H. Sternemann, O.M. Feroughi, H. Conrad, F. Djurabekova, A. Hohl, G.T. Seidler, M. Tolan, and K. Hämäläinen (2010). *Phys. Rev. B* **81**, 205317: "Suboxide interface in disproportionating a -SiO studied by x-ray Raman scattering".

- **Ch.J. Sahle**, M. Zschintzsch, C. Sternemann, J. von Borany, A. Mücklich, A. Nyrow, N.M. Jeutter, R. Wagner, R. Frahm, and M. Tolan (2011). *Nanotechnology* 22, 125709: "Influence of hydrogen on thermally induced phase separation in GeO/SiO 2 multilayers".

- M. Zschintzsch, **Ch.J. Sahle**, C. Sternemann, J. von Borany, A. Mücklich, A. Nyrow, and M. Tolan (2011). *Nanotechnology* **22**, 485303: "Ge-Si-O phase separation and Ge nanocrystals growth in Ge:SiO_x/SiO_2 multilayers – A new dc magnetron approach".

- J.S. Tse, Yang, S.J. Zhang, C.Q. Jin, **Ch.J. Sahle**, C. Sternemann, A. Nyrow, V. Giordano, J.Z. Jiang, S. Yamanaka, and C.A. Tulk (2011). *Phys. Rev. B* **84**, 184105: "Pressure-induced Electron Topological Transitions in Ba-doped Si Clathrate".

Other publications

- P. Link, D. Wandner, I. Schellenberg, R. Pöttgen, M. Paulus, **Ch.J. Sahle**, C. Sternemann, and U. Ruschewitz (2010). *Z. Anorg. Allg. Chem.* **636**, 2276:

"$Eu_xSr_{1-x}C_2$ ($0 < x < 1$): A dicarbide solid solution with perfect vegard behavior".

- M.A. Schroer, M. Paulus, Ch. Jeworrek, C. Krywka, S. Schmacke, Y. Zhai, D.C.F. Wieland, **Ch.J. Sahle**, M. Chimenti, C.A. Royer, B. Garcia-Moreno, M. Tolan, and R. Winter (2010). *Biophys. Journal* **99**, 3430-3437: "High-pressure SAXS study of folded and unfolded ensembles of proteins".

- F. Lehmkühler, A. Sakko, C. Sternemann, M. Hakala, K. Nygard, **Ch.J. Sahle**, S. Galambosi, I. Steinke, S. Tiemeyer, A. Nyrow, T Buslaps, D. Pontoni, M. Tolan, and K. Hämäläinen (2010). *J. Phys. Chem. Lett.* **1**, 2832: "Anomalous energetics in tetrahydrofuran clathrate hydrate revealed by x-ray Compton scattering".

- A. Steffen, C. Kronholz, M. Paulus, F. Wieland, S. Bieder, P. Degen, **Ch.J. Sahle**, M. Ferreira, R. Wagner, W. Tillmann, and M. Tolan (2010). *1st International Conference on Product Property Prediction*, ISBN 978-3-9808718-6-0: "Predicting properties of materials with x-rays: The application of synchrotron radiation in materials science".

- M.A. Schroer, J. Markgraf, D.C.F. Wieland, **Ch.J. Sahle**, J. Möller, M. Paulus, M. Tolan, and R. Winter (2011). *Phys. Rev. Lett.* **106**, 178102: "Nonlinear pressure dependence of the interaction potential of dense protein solutions".

- F. Lehmkühler, A. Sakko, I. Steinke, C. Sternemann, M. Hakala, **Ch.J. Sahle**, T. Buslaps, L. Simonelli, S. Galambosi, M. Paulus, T. Pylkkänen, M. Tolan, and K. Hämäläinen (2011). *J. Phys. Chem. C* **115**, 21009: "Temperature Induced Structural Changes of Tetrahydrofuran Clathrate and of the Liquid Water/Tetrahydrofuran Mixture".

- M.A. Schroer, Y, Zhai., D.C.F. Wieland, **Ch.J. Sahle**, J. Nase, M. Paulus, M. Tolan, and R. Winter (2011). *Ang. Chem. Int. Ed.* **50**, 11413: "Exploring the Piezophilic Behavior of Natural Cosolvent Mixtures".

- J. Möller, M. Cebi, M.A. Schroer, M. Paulus, P. Degen, **Ch.J. Sahle**, D.C.F. Wieland, S. Leick, A. Nyrow, H. Rehage, and M. Tolan (2011). *Phys. Chem. Chem. Phys.* **13**, 20354: "Dissolution of iron oxide nanoparticles inside polymer nanocapsules monitored by means of X-ray scattering techniques".

- A. Steffen, M. Paulus, C. Kronholz, M. Ferreira, **Ch.J. Sahle**, W. Tillmann, and M. Tolan (2011). Proccedings of the 1st International Conference on Stone and Concrete Machining, ISBN 978-3-943104-22-6, 145: "An *in situ* diffraction study on cobalt feedstock materials".

Acknowledgments

I am indebted to M. Tolan and C. Sternemann for everything they have done for me.

A work of this extent cannot be accomplished without the help and support of others. Throughout the past years, I have received and welcomed advice, help, and guidance from tremendously many people in my scientific and private life alike. These very lines are dedicated to all of you, each one of the caring, patient, and understanding persons, to thankfully express my deepest gratitude.

This work was supported by the Deutsche Forschungsgemeinschaft grant (TO-169/14) which is gratefully acknowledged.

Eidesstattliche Erklärung

Hiermit erkläre ich an Eides statt, dass die vorliegende Dissertationsschrift — abgesehen von der Beratung durch meine wissenschaftlichen Betreuer — nach Inhalt und Form meine eigene Arbeit ist. Sie wurde weder ganz noch in Teilen an anderer Stelle im Rahmen eines Prüfungsverfahrens vorgelegt.

Dortmund, November 2011

_____

(Christoph J. Sahle)